BOSTON UNIVERSITY
GRADUATE SCHOOL OF ARTS AND SCIENCES

Dissertation

THERMODYNAMICS AND DYNAMICS OF SUPERCOOLED WATER

by

MARCO G. MAZZA

M.S., University of Catania, Italy 2001

Submitted in partial fulfillment of the
requirements for the degree of
Doctor of Philosophy
2009

Approved by

First Reader

H. Eugene Stanley, Ph.D.
University Professor and Professor of Physics

Second Reader

Richard Averitt, Ph.D.
Associate Professor of Physics

To my mother who always supported me;

in memory of my father.

Acknowledgments

Firstly, I want to thank my advisor H. Eugene Stanley, for his support and encouragement during all these years; Gene will never cease to be a source of inspiration and admiration to me, both as a man and as a scientist. I am deeply grateful to Nicolas Giovambattista who has been an example to me since the first day. I thank Francis Starr, who has taught me a lot and literally opened his home to me. I thankfully acknowledge Giancarlo Franzese who can find the right question to ask at any time, and for that he has my complete admiration. I also thank Sergey Buldyrev, his kindness and infinite patience have no match.

So many friends have shared their path with mine and they have been wonderful companions, both inside and outside the walls of BU. I thank Sameet Sreenivasan, because I know that I can always count on him. We have shared many laughs, and many conversations that were never meant to end. My sincere thanks to my first roommates: Steve and Rob Nelson. They welcomed me in their family and they taught me to love baseball, a beautiful expression of the American spirit. I thank Mike Litos and Monica Pangilinan, also wonderful roommates. I am grateful to Daan aan de Kerk, with whom I enjoyed many dinners in our home at "Uniroad" and who incited me to cook, and now it is my passion. I greatly acknowledge Daniel Schmitt for his inspiring friendship that links us no matter how far apart we are. I thank Silvia Viola for always being present in my life in Boston; our feisty conversations will never mask our love. My infinite thanks to Claudia De Grandi, because through her eyes the world is beautiful. I also thank Diego Guerra who can say more things with his eyes than with a hundred words. I wish to thank Jan Beucke for his rare and immovable friendship; I know we'll share a bond for a long time. Limei Xu has been

the elder sister I never had, my gratitude goes to her for the laughters and preoccupations we shared in 202.

I would also like to thank Plamen Ivanov, Jiayuan Luo, Elena Strekalova, Kevin Stokely, Sungho Han, Jerry Paul, Bob Tomposki and Jerry Morrow for being a unique family; Mirtha Cabello deserves my gratitude for helping and sharing a smile with me every day, since the first day.

And finally I want to thank my family: my mother Antonia, whose love is boundless, my sister Valeria, whom I deeply love, and my father Vito, who didn't see me take these steps.

THERMODYNAMICS AND DYNAMICS OF SUPERCOOLED WATER

(Order No.)

MARCO G. MAZZA

Boston University Graduate School of Arts and Sciences, 2009

Major Professor: H. Eugene Stanley, University Professor and Professor of Physics

ABSTRACT

This thesis employs methods of statistical mechanics and numerical simulations to study some aspects of the thermodynamic and dynamic behavior of liquid water.

As liquid water is cooled down into the supercooled state, some regions of the sample show correlated molecular motion. Previously, only the translational motion has been the object of investigation. Given the importance of orientational dynamics for water, a question that naturally arises is whether the rotational molecular motion also shows heterogeneous dynamics. We show that the most rotationally mobile molecules tend to form clusters, "rotational heterogeneities", and we study their dependence upon observation time and temperature. Further, we show evidence that molecules belonging to dynamic heterogeneities are involved in bifurcated bonds.

Since the presence of dynamic heterogeneities is increasingly important as the temperature is lowered, one would expect a signature of this phenomenon in dynamical quantities. We study the effect of dynamic heterogeneities on the origin of the breakdown of the Stokes–Einstein and Stokes–Einstein–Debye relations for water. These relations link the diffusivity to temperature and viscosity. We study the separation of time scales of dynamic heterogeneities and the diffusive regime. We also consider different sets of mobility, slowest and fastest, for both translational and rotational heterogeneities.

A long–standing problem in biology is the seemingly universal loss of biological activity of all biomolecules, a phenomenon termed the "protein glass transition". We explore the connection between the hypothesized liquid–liquid phase transition of water, and the protein glass transition. We find that the protein glass transition coincides with the crossing of the Widom line of hydration water.

Many different scenarios have been proposed to rationalize water's thermodynamic anomalies. We study a cell model for water using the Wolff cluster algorithm, which permits rapid equilibration. We find that three different scenarios for the phase diagram of water can be coherently described through the concept of H bond cooperativity. Finally, we study an intriguing prediction of the cell model: the presence of two maxima in the specific heat of water. We draw connections with recent experimental data.

Contents

List of Figures

List of Abbreviations

DH	Dynamic Heterogeneities
CPF	Critical–Point Free
HDL	High Density Liquid
LDL	Low Density Liquid
LLCP	Liquid–Liquid Critical Point
MC	Monte Carlo
MD	Molecular Dynamics
RH	Rotational Heterogeneities
SF	Singularity–Free
SL	Stability Limit
TH	Translational Heterogeneities
TMD	Temperature of Maximum Density

Chapter 1

Introduction

1.1 An important and peculiar liquid

The importance of water to human life is difficult to exaggerate. Early settlements of people grew around sources of fresh water. The Nile River and the Tigris and Euphrates had fundamental role in the history of civilization because they provided potable water, irrigated the fields and were means of transportation. No surprise that water became an archetypical symbol of life in every culture. Aristotle in his *Physics* considered water as a fundamental element of the universe.

The study of the physics of water, in a modern sense, starts three centuries ago [1] when the first anomaly of liquid water was recognized: if the temperature T is lowered below $4\,^\circ\mathrm{C}$ at atmospheric pressure the density decreases. Today we know a lot more about water, but there are still some fundamental questions left without answer.

The thermodynamic phase diagram of water is rich and complex: more than sixteen crystalline phases [2], two or more glasses [3], and possibly two critical points. Water is a peculiar liquid, under many aspects. To start illustrating how the behavior of water deviates from other liquids we plot in Fig. 1.1 the melting and boiling temperatures for water and other hydride compounds of atoms of Group 6A. As the molecular weight decreases (from right to left in Fig. 1.1) both melting and boiling temperatures monotonically decrease except for the lightest atom: the oxygen in the water molecule. The dashed lines represent

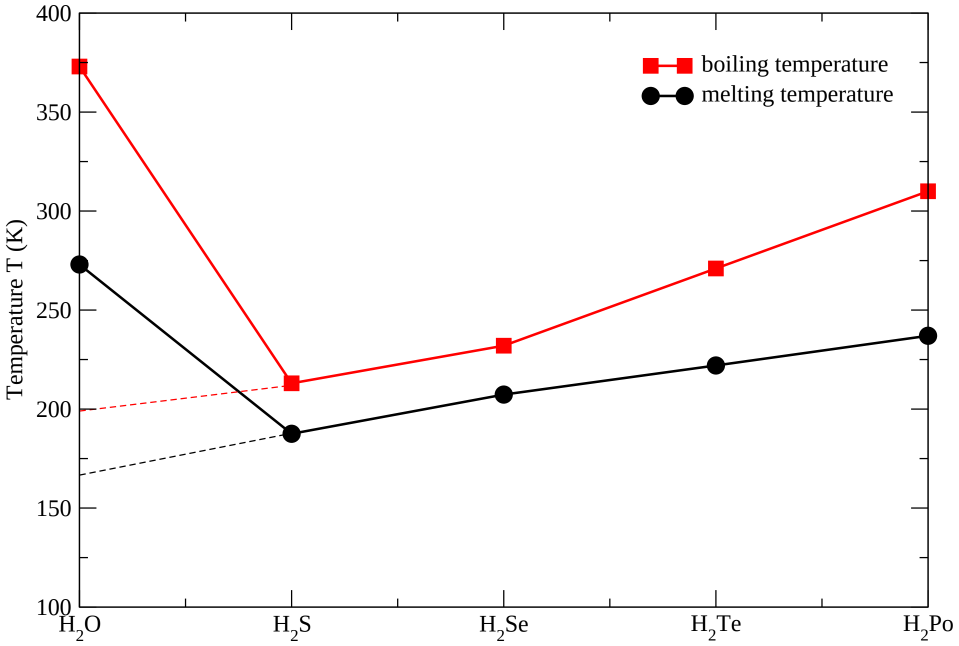

Figure 1.1: The melting and boiling temperatures for isoelectronic hydride molecules. Data from Ref. [4].

simple extrapolations if water were to follow the behavior of the other isoelectronic hydrides. We can notice that the difference between the real data and the extrapolated values is about 100 K for the melting point, and about 170 K for the boiling point. A very important consequence of the shift of these two temperatures is that the stable liquid phase of water is located well in the range of temperatures accessible on our planet. With a boiling point at $\approx$ 200 K all the water on Earth would be in the gaseous phase. Since life started in the oceans, this hypothetical "extrapolated" behavior of water would have hindered, if not made impossible, the evolution of life as we know it.

In Fig. 1.2 we show the stable phase of the vapor, the liquid and some crystalline forms that have a phase boundary with liquid water. It is also shown the solid–liquid–vapor triple point, $T_{\rm TP} = 273.16$ K, $P_{\rm TP} = 611.657$ Pa, and the liquid–gas critical point, $T_{\rm C} = 647.096$ K $P_{\rm C} = 22.064$ MPa. Another interesting feature of water that we can notice from Fig. 1.2 is the negative slope of the liquid–solid first–order transition line. We can easily derive an important thermodynamic relation. When two phases of a substance are in equilibrium,

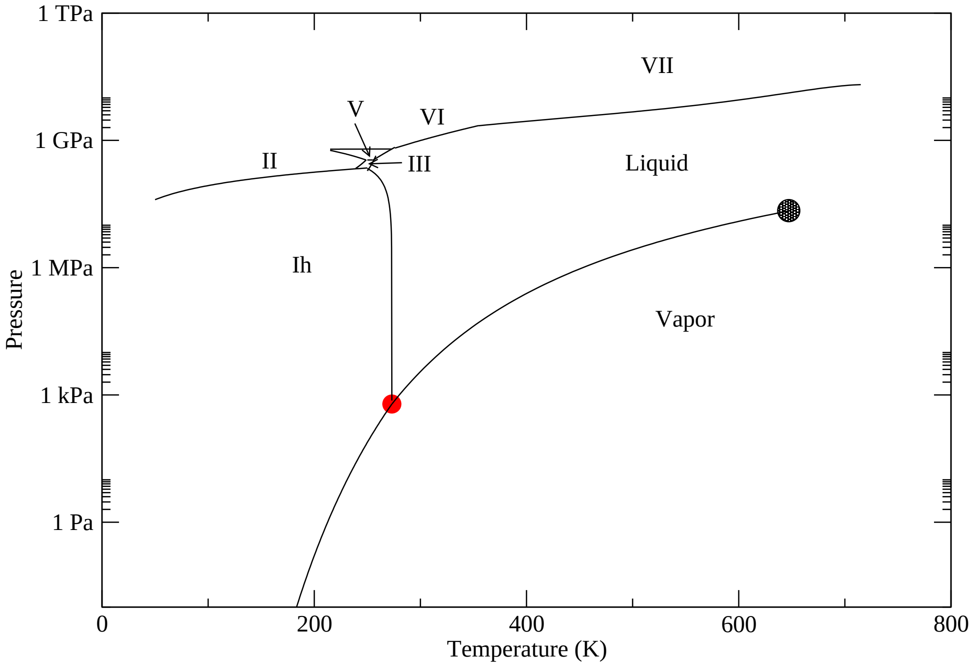

Figure 1.2: Phase diagram of water showing the stable phase of vapor, liquid and some crystalline ices.

the temperatures T, pressures P and chemical potentials μ must be equal [5]

$$T_1 = T_2 \tag{1.1}$$

$$P_1 = P_2 \tag{1.2}$$

$$\mu_1 = \mu_2. \tag{1.3}$$

If we express the potential in terms of T and P we have

$$\mu_1(P,T) = \mu_2(P,T) \tag{1.4}$$

from which we can immediately conclude that pressure and temperature of two phases in equilibrium cannot be assigned independently, but one is a function of the other, for example, $P = P(T)$. If we take the derivative of Eq. 1.4, we obtain

$$\frac{\partial \mu_1}{\partial T} + \frac{\partial \mu_1}{\partial P}\frac{dP}{dT} = \frac{\partial \mu_2}{\partial T} + \frac{\partial \mu_2}{\partial P}\frac{dP}{dT}, \tag{1.5}$$

since $(\partial \mu/\partial T)_P = -s$, where s is the specific entropy, and $(\partial \mu/\partial P)_T = v$, where v is the

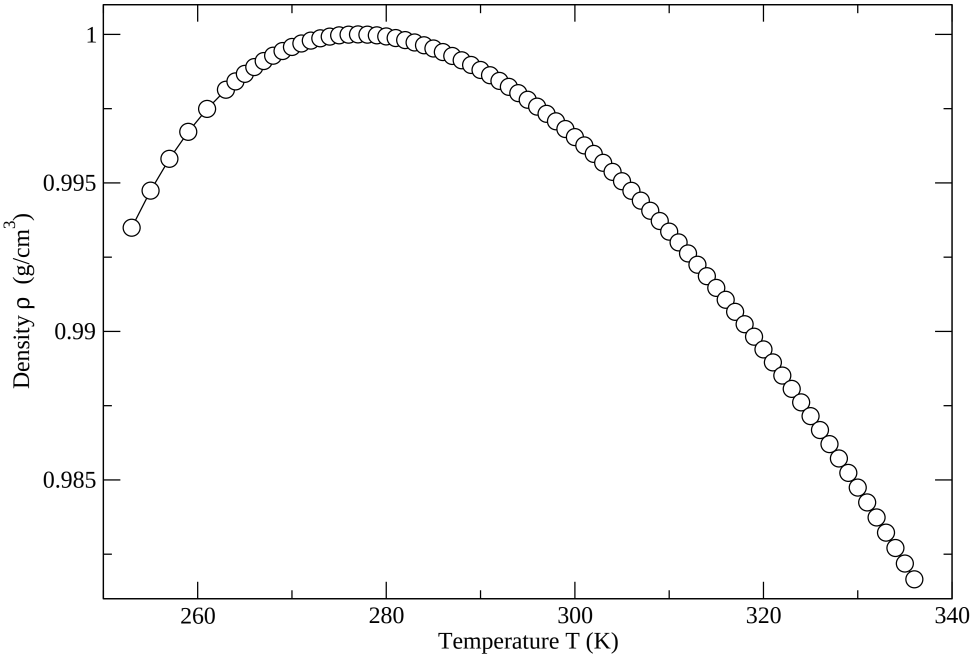

Figure 1.3: Density as a function of temperature at one atmosphere for liquid water. The density decreases for $T < 277$ K. Data taken from Ref. [6].

specific volume, we finally obtain

$$\frac{dP}{dT} = \frac{\Delta s}{\Delta v} \tag{1.6}$$

which is called the *Clausius–Clapeyron equation*. In the case of the liquid–solid transition of water, we already recognized the negative slope of the first–order line in the $P - T$ plane, i.e. $dP/dT < 0$. Upon cooling the entropy must decrease, because $C_P \equiv T \left(\frac{\partial S}{\partial T}\right)_P > 0$, hence the entropy S is a monotonically increasing function of T. This implies that the specific volume must increase in the phase transition from liquid to solid. The physical origin of this volume increase upon cooling is the hydrogen (H) bond. The formation of a H bond between two water molecules leads to a local volume expansion. This simple fact is the origin of another thermodynamic anomaly of water with far–reaching consequences: the density anomaly. In Fig. 1.3 we show the density of liquid water at one atmosphere as a function of T. The presence of a maximum at 277 K is referred to as the “density anomaly”, since for the vast majority of liquids the density decreases monotonically as T is lowered.

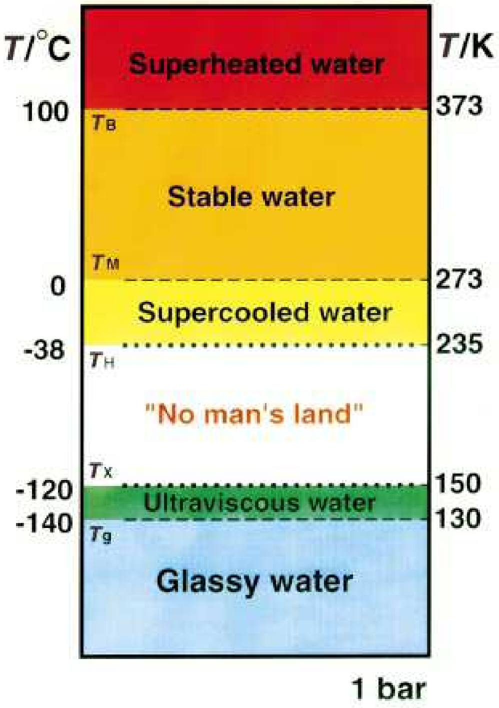

Figure 1.4: Schematic representation of the stable and metastable phases of water at atmospheric pressure. Figure courtesy of Dr O. Mishima.

Incidentally, this anomaly guarantees that the animals and the vegetation inhabiting rivers and lakes survive winter, because the ice is limited to the surface.

For some time a substance can remain in the liquid phase even below the temperature at which the stable thermodynamic phase is the solid. Such metastable state is called *supercooled*. Water can be cooled at $P = 1$ atm to $-38\,^{\circ}$C. Upon pressurization, the lowest temperature reached with supercooled water is $-92\,^{\circ}$C at $P = 210$ MPa [3]. Such metastable state is possible because the liquid–gas transition is of first order, thus, in order to form the two phases an energy barrier has to be overcome, corresponding to the surface tension of the interface between the two phases. Furthermore, the initial formation of the crystal, i.e. the nucleation process, is a kinetic process whose rate of occurrence can be reduced by using samples free of impurities, or by using vessels with very smooth surfaces, since any irregularity can initiate the nucleation process. However, the energy barrier to nucleation diminishes as the temperature is lowered, until reaching a temperature where the energy barrier is of the order of $k_B T$, where k_B is Boltzmann constant, i.e. thermal fluctuation. This temperature is named *homogeneous nucleation temperature* $T_{\rm H}$.

Below $T_{\rm H}$ water crystallizes. But it is possible to avoid the crystalline phase altogether by cooling very rapidly the sample (a typical cooling rate is $\sim$ 100 K/min [7]). What is obtained is *glassy* water, i.e., an amorphous solid. The temperature at which the molecular relaxation time reaches 100 s is conventionally called the "glass transition temperature" T_g. For water $T_g \approx 165$ K [8]. It is important to note that this is not a thermodynamic transition in the standard sense (such as the liquid–gas transition), but rather a kinetic event.

If glassy water is heated, it crystallizes to ice Ic (cubic ice). Therefore, there is an interval 165 K $\lesssim T \lesssim$ 235 K where it is impossible to probe the supercooled state; because of these experimental limits this region of the phase diagram of water has been termed "no man's land". In Fig. 1.4 we show a schematic of the phase diagram at 1 atm representing the stable, metastable and glassy phases of water.

1.2 Thermodynamic anomalies

Water is a very anomalous liquid. To date sixty six anomalies have been recognized [9]. We have briefly described the density anomaly, but the set of anomalies can be broadly divided in thermodynamic anomalies (such as the density maximum), dynamic anomalies (such as the maximum in diffusivity as a function of T), and material anomalies (such as the dielectric constant). In this section we will discuss the thermodynamic anomalies.

When studying a thermodynamic system, pressure or temperature perturbations are induced into the sample and its response to these is observed. It is therefore natural to consider the following important thermodynamic response functions

i) the isobaric and isochoric specific heat

$$C_P \equiv T \left(\frac{\partial S}{\partial T}\right)_P = \left(\frac{\partial H}{\partial T}\right)_P , \tag{1.7}$$

$$C_V \equiv T\left(\frac{\partial S}{\partial T}\right)_V = \left(\frac{\partial U}{\partial T}\right)_V, \tag{1.8}$$

where S is the entropy, $H \equiv U + PV$ the enthalpy, V the volume, and U the total internal energy of the system

ii) the isothermal compressibility

$$K_T \equiv -\frac{1}{V}\left(\frac{\partial V}{\partial P}\right)_T, \tag{1.9}$$

iii) the adiabatic compressibility

$$K_S \equiv -\frac{1}{V}\left(\frac{\partial V}{\partial P}\right)_S, \tag{1.10}$$

iv) the coefficient of thermal expansion

$$\alpha_P \equiv \frac{1}{V}\left(\frac{\partial V}{\partial T}\right)_P. \tag{1.11}$$

Some useful relations among these quantities are

$$K_T(C_P - C_V) = TV\alpha_P^2, \tag{1.12}$$

and

$$\frac{C_P}{C_V} = \frac{K_T}{K_S}. \tag{1.13}$$

In Fig. 1.5 we show the isobaric specific heat at atmospheric pressure for liquid water, both stable and supercooled, down to 236 K. This type of anomalous increase is not found in other molecular liquids, even those with water–like properties, such as H_2O_2 and N_2H_4 [10]. Similarly to C_P , also the isothermal compressibility K_T shows an anomalous increase upon cooling, that becomes more pronounced in the supercooled state [Fig. 1.6]. From these data there seems to be a singular temperature just below the lowest point reachable in experiments. Indeed, it is possible to fit the data with power–laws

$$C_P \sim (\frac{T}{T_s} - 1)^{-0.36} \tag{1.14}$$

$$K_T \sim (\frac{T}{T_s} - 1)^{-0.349}, \tag{1.15}$$

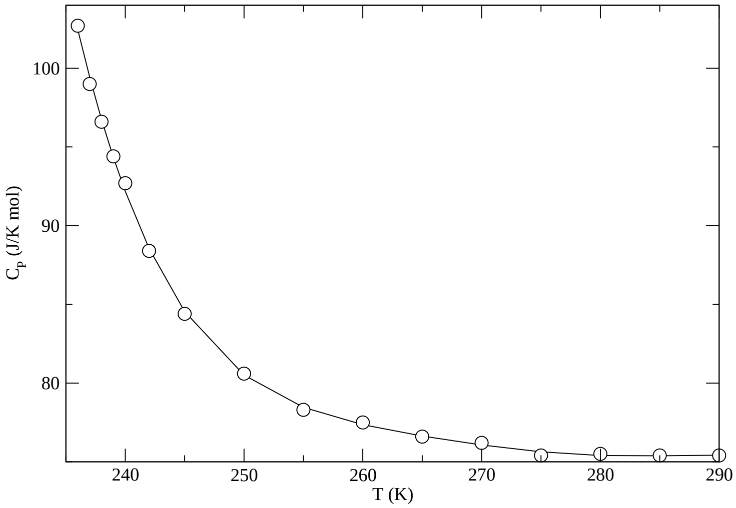

Figure 1.5: Isobaric specific heat C_P of water as a function of temperature at atmospheric pressure. Data from Ref. [10]; the line is a guide for the eye.

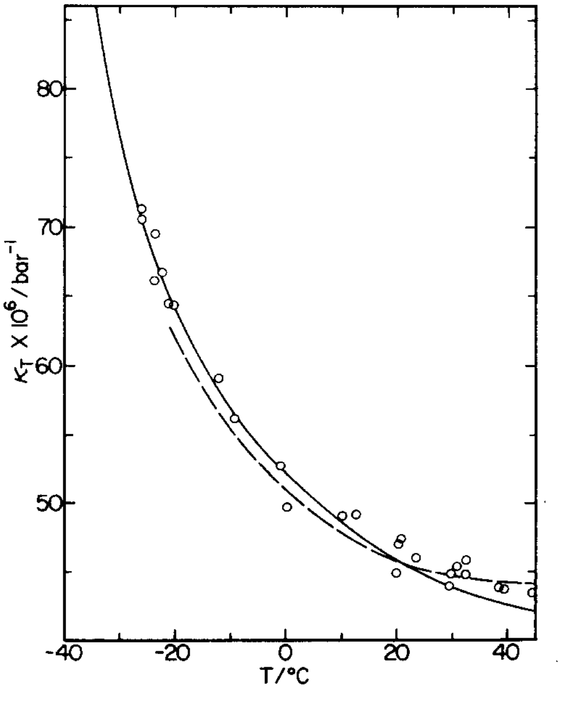

Figure 1.6: Isothermal compressibility of water as a function of temperature at atmospheric pressure. The dashed line is a polynomial extrapolation by Kell [6], the solid line is the plot of Eq.(1.15). Adapted from Ref. [11].

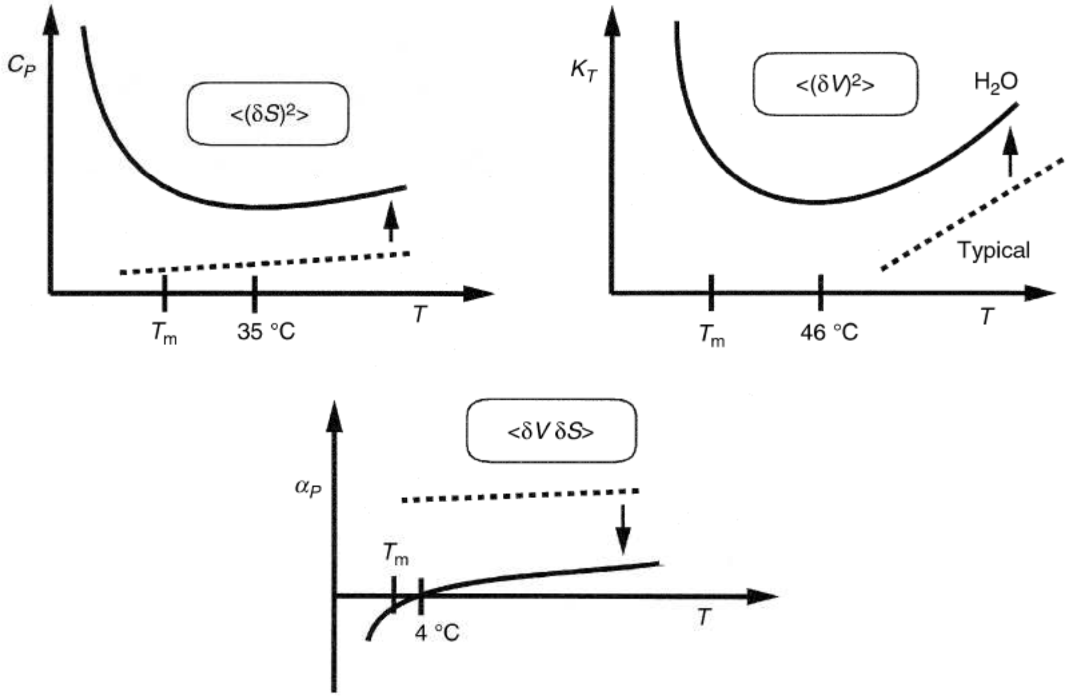

Figure 1.7: Schematic temperature dependence of (top left panel) the isobaric specific heat C_P, (top right panel) isothermal compressibility K_T, and (bottom panel) isobaric thermal expansion coefficient α_P for water. The behavior of a typical liquid is also shown with a dashed line. Figure courtesy of Dr. F. W. Starr [12].

and a predicted singular temperature $T_s = 228$ K [11].

To illustrate why we call anomalous this behavior of supercooled water, we consider the following relations that associate every response function to the corresponding fluctuation

$$\left\langle (\delta V)^2 \right\rangle = V k_B T K_T \tag{1.16}$$

$$\left\langle (\delta S)^2 \right\rangle = N k_B C_P \tag{1.17}$$

$$\langle (\delta S \delta V) \rangle = V k_B T \alpha_P \tag{1.18}$$

It is intuitive to think that as T is lowered thermodynamic fluctuations will decrease in amplitude, and in virtue of Eq. 1.16, 1.17, 1.18 also the thermodynamic response functions will decrease. Indeed, as shown with dashed lines in Fig. 1.7, for simple liquids the response functions decrease upon cooling, but water behaves differently. C_P and K_T show minima at 35 °C and 46 °C respectively, and then increase anomalously upon cooling into the supercooled regime.

This anomalous behavior is suddenly interrupted by crystallization. Since experiments in the liquid phase are not possible below T_H different theoretical models have been proposed to explain the behavior of supercooled water. Computer simulations have played an important role in establishing the plausibility of the different theories for liquid water. In the following Section we review some theories actively debated in the literature.

1.3 Stability limit hypothesis

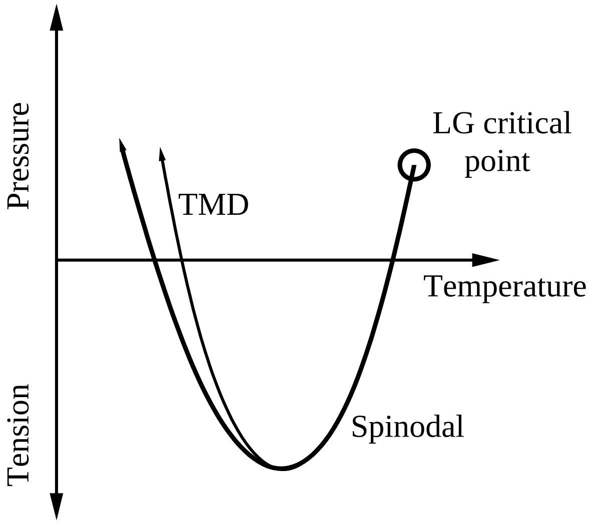

Figure 1.8: Schematic diagram of phase diagram on the (P, T) plane predicted by the stability limit hypothesis.

The stability limit hypothesis was proposed by Speedy in 1982[13]. It postulates the existence of a continuous limit of stability of the liquid for the superheated, stretched and supercooled states. In this scenario, the liquid spinodal, originating from the liquid–gas critical point, changes its slope in the negative pressure region of the (P, T) plane and re-enters the positive pressure region at lower T in the supercooled state, see Fig. 1.8. This limit of stability $P_s(T)$ is defined without reference to the phase on the other side of the spinodal. Since upon approaching a spinodal $(\partial P/\partial V)_T \to 0$, K_T will diverge at $P_s(T)$.

It is possible to demonstrate from thermodynamic first principles that a spinodal must change slope when it intersects a locus where $\alpha_P = 0$. The locus on the $(P,\, T)$ plane where the density shows a maximum, called temperature of maximum density (TMD), provides such an example.

A thermodynamic consequence of this scenario is that the intersection of the retracing spinodal with the liquid–vapor coexistence line must be a critical point [3]. The presence of a lower critical point in the liquid–vapor transition, altough possible, is not confirmed by any experiment. This fact poses a serious challenge to the stability limit scenario.

1.4 Liquid–liquid critical point hypothesis

A more recent scenario proposed by Poole *et. al.* [14] hypothesizes the existence of a second critical point in the phase diagram of water located in the supercooled state. This second critical point is the terminus of a line of first–order phase transition between two liquids, which, similarly to the liquid–gas critical point, are distinguished by the density: a low density liquid (LDL) at low P and a high density liquid (HDL) at higher P. The critical pressure and temperature of the liquid–liquid critical point (LLCP) predicted by computer simulations [14] are respectively $P_{C'} \approx 100$ MPa and $T_{C'} \approx 220$ K. The LLCP scenario is consistent with all the experimental evidence available to date. However, a direct verification of the presence of the LLCP is still missing because freezing prevents to access that region of the phase diagram (no man's land). Figure 1.9 shows a schematic representation of the phase diagram of water as predicted by the LLCP scenario.

An important consequence of the existence of a critical point for a substance is the concept of "Widom line". The correlation length ξ of a system grows upon approaching the critical point and diverges at it [15]. If, for instance, we consider an isobaric path in the $(P,\, T)$ plane in the neighborhood of the critical point, the thermodynamics response functions will show a local maximum reflecting the presence of critical fluctuations. The locus of maxima of correlation length is termed Widom line. Since asymptotically close to

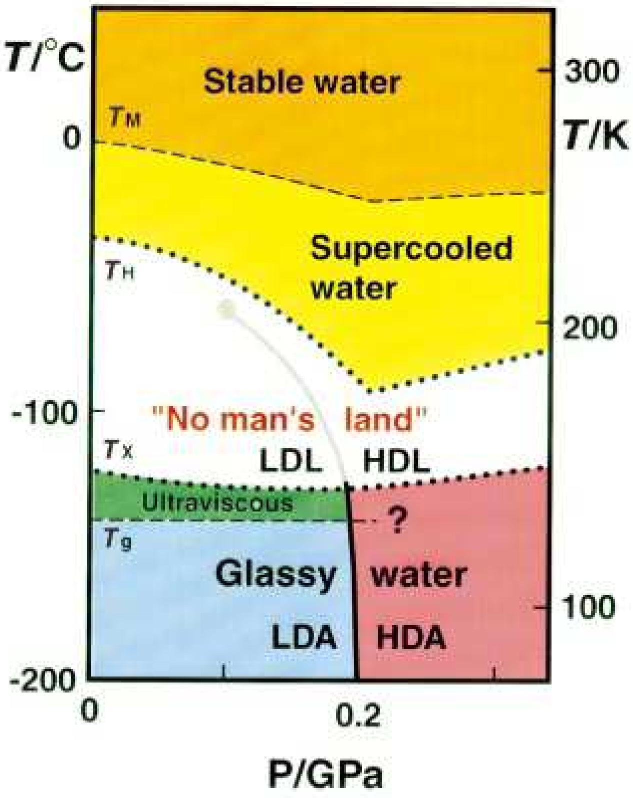

Figure 1.9: Schematic diagram of phase diagram on the $(P,\ T)$ plane predicted by the liquid–liquid critical point hypothesis. Figure courtesy of Dr. O. Mishima.

the critical point every response function can be expressed as a power law in ξ, the loci of maxima of response functions converge at the critical point, but they are otherwise distinct.

The Widom line that emanates from the LLCP projects into the experimentally accessible supercooled region of water. Thus, the anomalous increases of C_P and K_T are, in this scenario, an indirect manifestation of the LLCP.

1.5 The singularity–free scenario

In 1996 Sastry *et al.* proposed a thermodynamic picture that does not invoke critical behavior (a spinodal or the LLCP) in the phase diagram [16, 17]. Instead, the anomalous behavior of response functions in water are related to the negative slope of the TMD line in the (P, T) plane.

Let us derive a general thermodynamic theorem that will prove useful in the following. Along a path of constant $\alpha_P \equiv V^{-1}\left(\partial V/\partial T\right)_P$ we can write

$$d\alpha_P = \left(\frac{\partial \alpha_P}{\partial T}\right)_P dT + \left(\frac{\partial \alpha_P}{\partial P}\right)_T dP = 0 \tag{1.19}$$

and performing the derivatives gives

$$\frac{\partial}{\partial T}\left(\frac{1}{V}\frac{\partial V}{\partial T}\right)_P = -\frac{1}{V^2}\left(\frac{\partial V}{\partial T}\right)^2 + \frac{1}{V}\frac{\partial^2 V}{\partial T^2} = -\alpha_P^2 + \frac{1}{V}\frac{\partial^2 V}{\partial T^2} \tag{1.20}$$

$$\frac{\partial}{\partial P}\left(\frac{1}{V}\frac{\partial V}{\partial T}\right)_P = -\frac{1}{V^2}\frac{\partial V}{\partial P}\frac{\partial V}{\partial T} + \frac{1}{V}\frac{\partial^2 V}{\partial P \partial T} = K_T\alpha_P + \frac{1}{V}\frac{\partial^2 V}{\partial P \partial T}. \tag{1.21}$$

We can write

$$\left(\frac{dP}{dT}\right)_{d\alpha_P=0} = -\frac{\left(\frac{\partial \alpha_P}{\partial T}\right)_P}{\left(\frac{\partial \alpha_P}{\partial P}\right)_T}. \tag{1.22}$$

Along the TMD, $\alpha_P = 0$, we obtain

$$\left(\frac{dP}{dT}\right)_{\mathrm{TMD}} = -\frac{\frac{\partial^2 V}{\partial T^2}}{\frac{\partial^2 V}{\partial P \partial T}}. \tag{1.23}$$

Next we consider the following thermodynamic derivative

$$\left(\frac{\partial K_T}{\partial T}\right)_P = -\left[\frac{1}{V}\frac{\partial^2 V}{\partial P \partial T} + K_T\alpha_P\right] \tag{1.24}$$

By restricting to the TMD we obtain

$$\left(\frac{\partial K_T}{\partial T}\right)_{P,\mathrm{TMD}} = -\frac{1}{V}\frac{\partial^2 V}{\partial P \partial T}. \tag{1.25}$$

Using Eq. 1.25 into Eq. 1.23 yields the final result

$$\left(\frac{\partial K_T}{\partial T}\right)_{P,\mathrm{TMD}} = \frac{1}{V}\frac{\partial^2 V/\partial T^2}{(dP/dT)_{\mathrm{TMD}}}. \tag{1.26}$$

The TMD is the locus of density maxima, and in the (P, T) has a negative slope for positive pressure, hence $(dP/dT)_{\mathrm{TMD}} < 0$; since $\partial^2 V/\partial T^2$ is positive at the TMD, we can conclude from Eq. 1.26 that K_T must increase upon isobaric cooling. Therefore, in the singularity–free scenario the increase of the response functions is a consequence of the density anomaly, and it is predicted not to show any singular behavior [18]. Ultimately, it is the anticorrelation between entropy and volume in water that causes the thermodynamic anomalies. Upon cooling the entropy must decrease, and since, in water, ordering is achieved through H bond formation, the volume will increase. Another interesting consequence of Eq. 1.26 is the fact that if the TMD has an infinite slope, the locus of maxima of K_T will meet the TMD with a zero slope.

1.6 Overview of the Dissertation

In this first chapter of this Dissertation, we have introduced the physical problems of liquid water, the experimental evidence and the currently discussed theoretical approaches. In chapter 2 we study the importance of clusters of correlated molecular motion in water. These regions of the fluid, known as dynamic heterogeneities, become increasingly important upon cooling a liquid towards the glass transition temperature. Here we show the relation between regions of correlated translational motion and regions of correlated rotational motion, and how this is relevant to the diffusion mechanism for a cold dense liquid.

In chapter 3 we analyze how dynamic heterogeneities modify the diffusion in water leading to the breakdown of hydrodynamic laws relating diffusion coefficient to temperature and viscosity, the Stokes–Einstein and Stokes–Einstein–Debye relations. We find a general collapse onto a master curve for the diffusivity as a function of temperature measured for different families of clusters, that differ by the amount of molecular mobility. Further, we find that the largest contribution to the breakdown of the Stokes–Einstein and Stokes–Einstein–Debye relations originates at the time scale when dynamic heterogeneities are more prominent. This finding offers a link connecting the characteristic time scale of dynamic heterogeneities, the end of the cage regime, with the diffusive regime.

In chapter 4 we consider the problem of the “protein glass transition”. There is experimental evidence that nearly every biomolecules ceases any biological activity near 200 K. We propose a connection between this phenomenon and the possible liquid–liquid phase transition occuring in water. Upon cooling, water undergoes a transition from a disordered liquid to a less dense liquid with short–range order. We find that this transition correlates very closely with the protein glass transition.

In chapter 5 we introduce a microscopic cell model that is able to reproduce the thermodynamic features of liquid water. We employ both Monte Carlo simulations and mean–field analytical calculations to determine the phase diagram. Finally, in chapter 6 by tuning a model parameter that physically corresponds to a three–body correlation among water molecules, i.e., O-O-O correlation, we find that four seemingly different scenarios for water’s phase diagram correspond to different degrees of cooperativity among hydrogen bonds.

Chapter 2

Dynamics of supercooled water

In this chapter we will first describe the Adam–Gibbs theory by following the original description given in their seminal paper [19]. Then we will describe the concept of dynamic heterogeneities in supercooled water. The presence of heterogeneous dynamics in the translational and rotational molecular motion will be studied by using computer simulations.

2.1 Adam–Gibbs theory

The theory of Adam and Gibbs [19] describes T-dependent relaxation processes for the liquid state starting from the concept of *cooperatively rearranging regions* (CRR). A CRR is defined as a "*subsystem of the sample which, upon a sufficient fluctuation in energy (or, more correctly, enthalpy), can rearrange into another configuration independently of its environment*" [19]. When a liquid is supercooled the CRR grow and the local molecular relaxation requires an increasing number of molecules with correlated motion. The growth of these regions is reflected in a decrease of configurational entropy, because fewer and fewer states are accessible to the system, hence the increase of the relaxation times. The probability that a CRR changes state is calculated in terms of the dimension, or number of molecules, z of the CRR, that we assume compact in shape. Further, we assume that the subsystem interacts weakly with its surrounding. These CRR are in thermal and mechanical equilibrium with each other, thus we can consider an isothermal–isobaric ensemble of N

independent distinguishable subsystems comprising z molecules. The partition function is

$$\Delta(z, P, T) = \sum_{E,V} \omega(z, E, V) \exp[-(E + PV)/k_B T] \tag{2.1}$$

where ω is the number of configurations of z molecules with energy E and volume V. Thus, the Gibbs free energy is given by

$$G = z\mu = -k_B T \ln \Delta. \tag{2.2}$$

By summing over only the values of E and V involved in a transition, we obtain the partition function for the CRR

$$\Delta'(z, P, T) = \sum_{E,V} \omega'(z, E, V) \exp[-(E + PV)/k_B T] \tag{2.3}$$

where now ω' is the number of configurations of z molecules with energy E and volume V that can rearrange cooperatively. The corresponding Gibbs free energy is $G' = z\mu' = -k_B T \ln \Delta'$. The transition probability for a region of size z, W_z is then proportional to the fraction of subsystems that can rearrange, i.e.Δ'/Δ. With the notation $z\Delta\mu = z(\mu' - \mu) = G' - G$, we obtain

$$W_z = A \exp(-z\Delta\mu/k_B T). \tag{2.4}$$

We can assume the T-dependence of the pre–factor A negligible with respect to the exponential. Also the dependence of $\Delta\mu$ on z and T is small.

The average transition probability W is the sum of W_z over all possible values of z. Furthermore, there is a lower limit z^* to the size of a CRR.

$$W = \sum_{z=z^*}^{\infty} A \left[\exp(-\Delta\mu/k_B T)\right]^z \quad , \tag{2.5}$$

We can easily derive an expression for z^* with the following argument. The configurational entropy of the macroscopic system composed of N_{CRR} number of CRR is

$$S_c = N_{CRR} s_c \tag{2.6}$$

where s_c is the configurational entropy of a subsystem of size z. However S_c can be expressed directly in terms of W_c, the number of configurations accessible to the system

$$S_c = k_B \ln W_c. \tag{2.7}$$

If we consider the system to be one mole, then we can write

$$s_c = \frac{k_B}{N_{CRR}} \ln W_c = k_B \frac{z}{N_A} \ln W_c \tag{2.8}$$

where N_A is Avogadro number. Now, there must be a lower bound z^* to z because in a rearrangement there must be at least two configurations available; this corresponds to a value of the configurational entropy per CRR given by

$$s_c^* = k_B \frac{z^*}{N_A} \ln W_c = \frac{z^*}{N_A} S_c. \tag{2.9}$$

Thus we find

$$z^* = N_A s_c^* / S_c. \tag{2.10}$$

We can now perform the truncated sum

$$W = \frac{A}{1 - \exp(-\Delta\mu / k_B T)} \exp(-z^* \Delta\mu / k_B T) \quad . \tag{2.11}$$

At low T the denominator $1 - \exp(-\Delta\mu/k_B T)$ is nearly T-independent, so we can absorb it in the constant A, obtaining

$$W = \mathcal{A} \exp(-z^* \Delta\mu / k_B T) \quad . \tag{2.12}$$

This result implies that the majority of the transitions occur in regions predominantly of size z^*, the size of the smallest CRR. We now remember that from Eq. 2.10 $z^* \propto 1/s_{conf}$, and that $\Delta\mu$ is approximately T–independent; we can rewrite Eq. 2.12 as

$$W = \mathcal{A} \exp(-C/T S_{conf}) \tag{2.13}$$

where C has the dimension of energy. It was derived within the assumption of weak interacton among cooperative regions.

Equation 2.13 is commonly used in fitting experimental data; in these cases the S_{conf} is approximated for supercooled liquids as the difference between the entropy of the liquid and that of the crystal, $S_{conf} \simeq S_{liq} - S_{cris}$; the right–hand side of this relation is calculated from the specific heat and latent heat of fusion.

Since the inverse of W is a relaxation time τ, Eq. 2.13 predicts a divergence of τ when S_{conf} goes to zero. Extrapolations of experimental data seem to indicate that S_{conf} goes to zero for glass–forming liquids at a finite T called *Kauzmann temperature*, T_K. Below T_K the supercooled liquid (a disordered state) would have an entropy lower than the crystal (an ordered state). This hypothetical situation is termed the *Kauzmann paradox.* Experimentally the glass transition occurs before this extrapolated T, thus this paradox seems to remain only a theoretical pathology. Possibly, the origin of this paradox may lie in the assumption of thermodynamic continuity between the liquid and glassy state [3].

If we assume that S_{conf} goes to zero linearly in T, $S_{conf} \propto (T - T_K)$, we obtain

$$\tau \propto \exp\left[B/(T - T_K)\right] \tag{2.14}$$

which is called "Vogel–Fulcher–Tamman" relation (VFT), used to fit experimental data.

2.2 Dynamic heterogeneities in water

Supercooled liquids are characterized by the non–exponential decay of ensemble–averaged time correlation functions [20–24]. According to the mode coupling theory (MCT) [25, 26], this decay can be expressed in terms of a stretched exponential function, $\exp\left[-(t/t_r)^{\beta}\right]$ with $t_r \sim (T - T_{MCT})^{-\gamma}$, where T_{MCT} is the mode coupling temperature which is slightly above the glass transition temperature, T_g. Two microscopic scenarios have been proposed to explain this behavior, schematically shown in Fig. 2.1. In the spatially homogeneous dynamics scenario, correlation functions for different molecules decay in the same way, i.e., by a unique stretched exponential function with a characteristic relaxation time t_r and exponent β. As shown in Fig. 2.1, in the "homogeneous" scenario, all molecules are equivalent. As temperature is lowered, the locally averaged molecular displacement is the same at every

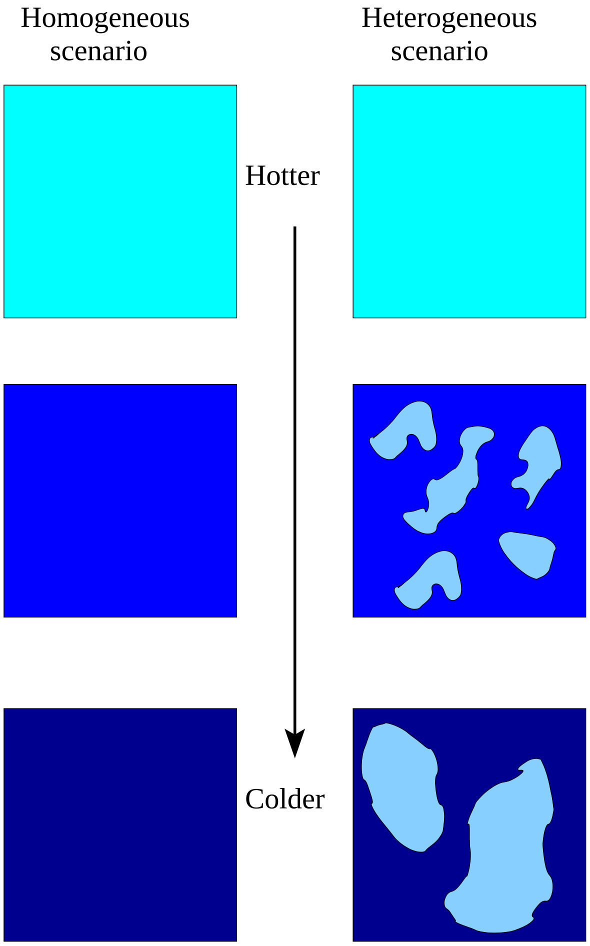

Figure 2.1: Two possible scenarios proposed to describe diffusion in cold liquids. In the spatially *homogeneous* dynamics scenario molecules relax in the same way, while in the spatially *heterogeneous* dynamics (SHD) scenario, sets of more mobile molecules (in comparison to the average motion of the molecules in the system) form patches or clusters. The size of these clusters increases upon cooling.

point in the system. The homogeneous scenario is inconsistent with experiments [27–32] and simulations [33–36], which identify dynamical heterogeneities in supercooled liquids and spin glasses [37].

In the spatially heterogeneous dynamics (SHD) scenario, correlation functions for different molecules decay exponentially, but with a broad distribution of relaxation times[38]. The superposition of these individual exponential contributions produces a non-exponential decay of the ensemble-averaged time correlation function, and the exponent β is a measure of the width of the distribution of relaxation times. In the heterogeneous scenario, the locally averaged molecular displacements are different depending on the part of the system box we are looking at. One finds groups of molecules that are more mobile and groups that are less mobile than the average molecule in the system. As the temperature is lowered, patches formed by mobile molecules increase in size. These patches of mobile molecules have a short lifetime; they appear and disappear constantly in different parts of the system.

Clusters composed of particles with high mobility have been found in numerical simulations of simple systems, e.g., Lennard-Jones (LJ) mixtures, indicating the presence of spatially heterogeneous dynamics (SHD) [27, 33, 36, 39–47]. Hence, the SHD scenario for the dynamics of liquids at low temperatures was confirmed. In this section we show that SHD are also present in computer simulations of the SPC/E [48] water model. We study a system with $N = 1728$ molecules at fixed density $\rho = 1.0$ g/cm^3 varying the temperature T from 200 K to 260 K in steps of 10 K. In order to increase statistics, we performed two independent simulations for every temperature. We find that the T–dependence of the diffusion constant can be expressed by:

$$D \sim (T - T_{MCT})^{\gamma}, \tag{2.15}$$

where the mode coupling temperature $T_{\mathrm{MCT}} = 193$ K and the diffusivity exponent $\gamma = 2.80$.

We use the approach to define SHD clusters which was introduced in a study of a LJ mixture [40] and in experiments on colloids [47]. We calculate the self part of the time-

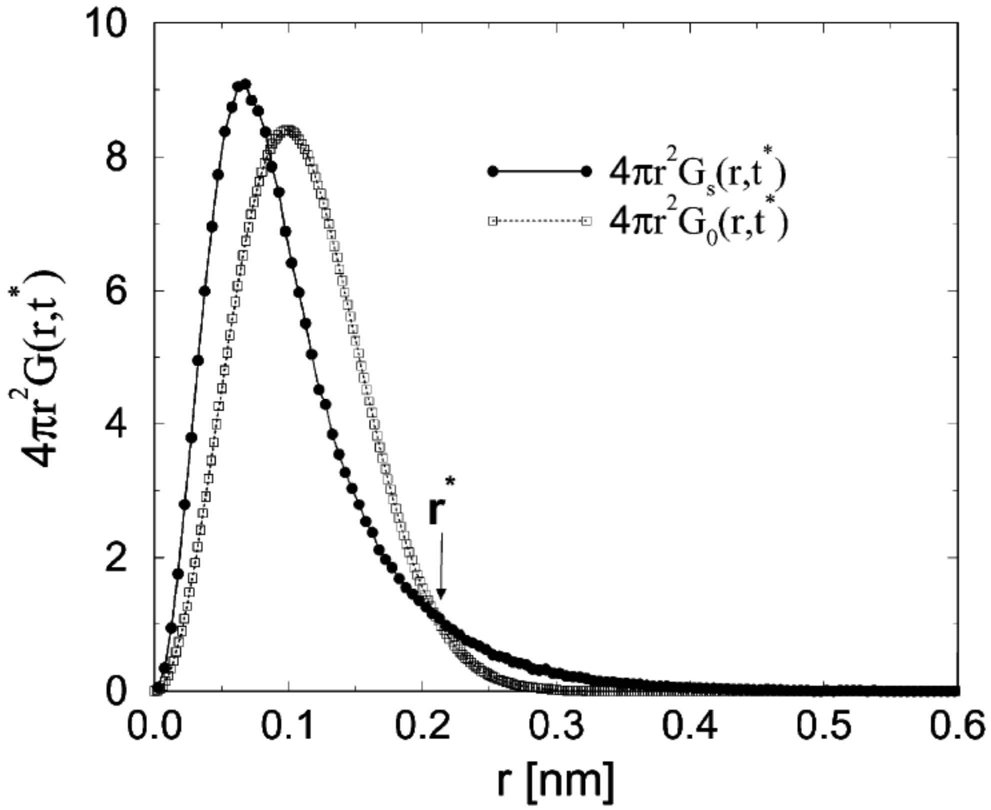

Figure 2.2: Van Hove correlation function $G_s(r, t^*)$ and its Gaussian approximation $G_0(r, t^*)$ obtained using $\langle r^2(t^*) \rangle$, for $T = 220$ K. The tails of the distributions cross at $r^* \approx 0.225$ for all temperature.

dependent van Hove correlation function [49] $G_s(r, t)$,

$$G_s(r,t) \equiv \frac{1}{N} \sum_{i=1}^{N} \langle \delta(|\vec{r}_i(t) - \vec{r}_i(0)| - r) \rangle \,, \tag{2.16}$$

where $\langle \cdots \rangle$ represents average over configurations and $\vec{r}_i(t)$ are the coordinates of the oxygen atom of the *i-th* molecule. The probability of finding an oxygen atom at a distance r at time t from its position at $t = 0$ is given by $4\pi r^2 G_s(r, t) dr$.

For both short times (when particles move ballistically) and long times (when particle motion can be described by the diffusion equation), $G_s(r, t)$ can be fitted by a Gaussian approximation

$$G_0(r,t) = \left[\frac{3}{2\pi\left\langle r^2(t)\right\rangle}\right]^{3/2} \exp\left[-3r^2/2\left\langle r^2(t)\right\rangle\right], \tag{2.17}$$

where $\left\langle r^2(t)\right\rangle$ is the mean square displacements of the oxygen atoms. However, deviations of $G_s(r,t)$ from $G_0(r,t)$ are well pronounced at intermediate times, corresponding to the vibrations of the particle within the cage formed by neighboring molecules. We define t^* as the value of time at which the deviation of $G_s(r,t)$ from $G_0(r,t)$ is maximum, which is achieved when the non-Gaussian parameter [20, 21]

$$\alpha_2(t) \equiv \frac{3}{5}\langle r^4(t)\rangle/\langle r^2(t)\rangle^2 - 1 \tag{2.18}$$

reaches its maximum.

In Fig. 2.2, we see that $G_s(r,t^*)$ and $G_0(r,t^*)$ intersect for large r at r^*, and that $G_s(r,t^*)$ develops a tail for large r falling outside the Gaussian distribution. Molecules with displacements $r > r^*$ can be considered as molecules that move more than expected (in comparison to $G_0(r,t^*)$). We find r^* is in the range 0.20–0.25 nm for all T (the oxygen-hydrogen distance in a molecule for SPC/E is 0.1 nm). The fraction of molecules with $r > r^*$ at $t = t^*$ is given by $\phi \equiv \int_{r^*}^{\infty} 4\pi r^2 G_s(r,t^*)dr$. Depending on T, we find $6\% < \phi < 8\%$. For simplicity we fix $\phi = 7\%$ for all T. Similar values of ϕ were found in atomic systems [39, 40, 47] and in polymer melts [50].

Following Refs. [40] and [47], we define the mobility of molecule i at a given time t_0 as the maximum displacement of the oxygen atom in the interval $[t_0, t_0 + \Delta t]$,

$$\mu_i(t_0,\Delta t) = \max\{|\vec{r}_i(t_0) - \vec{r}_i(t+t_0)|, t_0 \leq t \leq t_0 + \Delta t\}. \tag{2.19}$$

We will be interested in the "mobile" molecules defined as the fraction ϕ of molecules with largest μ_i. We define a connected SHD cluster, also called a dynamic heterogeneity (DH), for an observation time Δt formed by mobile molecules. A pair of molecules is assumed to be connected if their oxygen-oxygen distance at time t_0 is less than 0.315 nm, which corresponds to the first minimum of the oxygen-oxygen radial distribution function.[1] We find in water that SHD-clusters are similar to those in models of simpler liquids.

In LJ systems [39], monatomic liquids [51], and polymers [52], complex clusters are composed of more elementary "strings" in which particles are arranged in a roughly linear fashion. This is not so clear in simulations of water because the hydrogen bond network constrains the geometry of the clusters.

2.3 Rotational and translational dynamic heterogeneities

Experiments and computer simulations have shown that dynamics in supercooled liquids is spatially heterogeneous, i.e., one can identify transient regions with relaxation times different by orders of magnitude [45, 46, 53, 54]. Simulations have shown that the most mobile particles tend to form clusters [39, 55]. Different theoretical approaches have been developed to understand spatially heterogeneous dynamics [19, 56]. In particular, Adam and Gibbs (AG) [19] postulate the existence of cooperatively rearranging regions (CRR) whose molecules change configuration independently of the rest of the system. Molecular dynamics (MD) simulations [57, 58] have verified many of the predictions of the AG theory.

While there have been numerous studies of the heterogeneous nature of the translational degrees of freedom (TDOF) in water, there are few studies of the heterogeneous nature of the rotational degrees of freedom (RDOF). Here we systematically study the rotational dynamics of water and compare with the translational dynamics. Previous work for other systems suggests that translationally mobile molecules may have enhanced rotational mobility [59, 60], and the characteristic times for the RDOF are smaller than for the TDOF [61]. To this end we perform MD simulations of a system of $N = 1728$ water molecules interacting with the extended simple point charge potential (SPC/E) for a range of temperatures from 350 K down to 200 K at the fixed density of 1 g/cm^3; for each temperature we run

---

[1] Alternatively, we also consider using a separation of 0.35 nm, the distance criterion commonly used by hydrogen bond definitions [F. Sciortino and S. L. Fornili, J. Chem. Phys. **90**, 2786 (1989)]. Preliminary calculations indicated this alternative choice does not qualitatively affect our results.

two independent trajectories to improve[2] the statistics [23].

We first quantify the rotation of a molecule using the normalized polarization vector $\hat{p}_i(t)$, defined as the normalized vector from the center of mass of the water molecule to the midpoint of the line joining the two hydrogens. In a time interval $[t, t{+}\delta t]$, $\hat{p}_i(t)$ spans an angle $\delta\theta \equiv \cos^{-1}(\hat{p}_i(t) \cdot \hat{p}_i(t+\delta t))$. We define a vector $\delta\vec{\varphi}_i(t)$ such that $|\delta\vec{\varphi}_i(t)| = \delta\theta$ and its direction is given by $\hat{p}_i(t) \times \hat{p}_i(t+\delta t)$. Thus the vector $\vec{\varphi}_i(t) \equiv \int_0^t \delta\vec{\varphi}_i(t')dt'$ allows us to define a trajectory in a φ-space representing the rotational motion of molecule i. One can then associate a rotational mean square displacement (RMSD) given by

$$< \varphi^2(t) > \equiv \frac{1}{N} \sum_i |\vec{\varphi}_i(t) - \vec{\varphi}_i(0)|^2 \tag{2.20}$$

and a rotational diffusion coefficient

$$D_R \equiv \lim_{t\to\infty} \frac{1}{4tN} \sum_{i=1}^{N} \langle\, |\vec{\varphi}_i(t) - \vec{\varphi}_i(0)|^2 \rangle \,. \tag{2.21}$$

The vector $\vec{\varphi}_i(t)$ is not bounded to the unit sphere, since otherwise Eq. (2.21) would give $D_R = 0$. Equations (2.20) and (2.21) were applied in [63] to study a linear molecular system. If water molecules were linear, this one angle would suffice to fully describe the motion. To account for the fact that water molecules are not linear, we consider rotations also of the other two normalized principal vectors, which we label $\hat{q}_i(t)$ and $\hat{r}_i(t)$; we replace $\hat{p}_i(t)$ in the definition of $\vec{\varphi}_i$ with $\hat{q}_i(t)$ and $\hat{r}_i(t)$.

Figures 2.3(a) and 2.3(b) show the RMSD considering only the vector $\hat{p}$ (similar results hold for $\hat{q}$ and $\hat{r}$) and the temperature dependence of D_R for all the three vectors, which we label $D_{R,\,p}$, $D_{R,\,q}$ and $D_{R,\,r}$. Similar to Ref. [63] we observe: (i) the RMSD shows three different regimes: a *ballistic* regime, where $<\varphi^2> \propto t^2$, a plateau or *cage* regime, where molecules find themselves trapped in the cage formed by their neighboring molecules, and finally a *diffusive* regime where $<\varphi^2> \propto t$, these three regimes are analogous to those observed in studies of translational dynamics of supercooled liquids. (ii) D_R increases with T with a non-Arrhenius behavior. While the values of $D_{R,p}$, $D_{R,q}$ and $D_{R,r}$ differ (as

---

[2] Note that classical simulations can not capture any perturbation in the dynamics due to quantum effects, as discussed in [62]

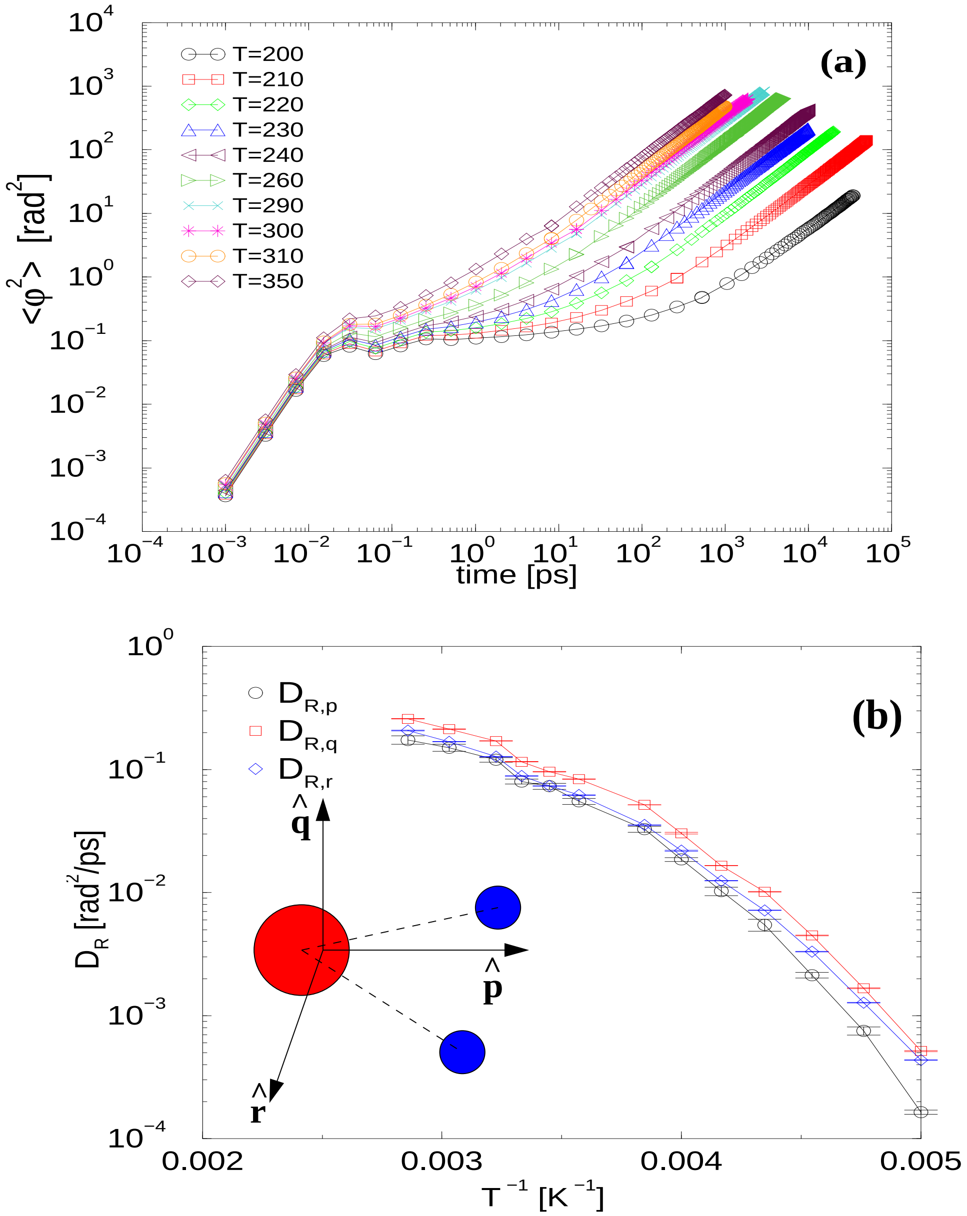

Figure 2.3: (a) RMSD for rotations of the polarization vector, $\hat{p}$, in a range of temperatures from 200 to 350 K. (b) Rotational diffusivity, D_R, as a function of T^{-1} for all three principal vectors, $\hat{p}$, $\hat{q}$ and $\hat{r}$. The inset shows a schematic defining these vectors.

found in [62]), they all show the same non-Arrhenius dependence on temperature. Note the oscillations in Fig. 2.3(a) present for times of the order of 10^{-2} ps. These oscillations, not present for linear molecules [63], correspond to the *libration* (hindered rotation) regime and occur at the same time as the oscillations observed in the rotational correlation function of water in [64].

We introduce the rotational counterpart of the self part of the time-dependent van Hove distribution function, $G_s(\varphi,t)$ [49],

$$G_s(\varphi,t) \equiv \frac{1}{N}\sum_{i=1}^{N}\langle\delta(|\vec{\varphi}_i(t)-\vec{\varphi}_i(0)|-\varphi)\rangle\,, \tag{2.22}$$

where $\langle\cdots\rangle$ represents average over configurations. With this formalism we recover the usual interpretation for $4\pi\varphi^2 G_s(\varphi,t)$ as the probability of having a molecule at time t with angular displacement φ. In other words, that in the abstract φ-space, a molecule has moved to a distance φ from its position at $t=0$. For long times the diffusion equation for $\vec{\varphi}_i(t)$ holds, and $G_s(\varphi,t)$ is a Gaussian distribution

$$G_0(\varphi,t) = \left[\frac{3}{2\pi\langle\varphi^2(t)\rangle}\right]^{3/2} \exp\left[-3\varphi^2/2\langle\varphi^2(t)\rangle\right]\;. \tag{2.23}$$

The deviations of $G_s(\varphi,t)$ from $G_0(\varphi,t)$ can be quantified by the non-Gaussian parameter [65] $\alpha_2(t) \equiv 3\langle\varphi^4(t)\rangle/5\langle\varphi^2(t)\rangle^2 - 1$. Figure 2.4(a) shows $\alpha_2(t)$ for different temperatures. $\alpha_2(t)$ shows a clear maximum at $t = t^*(T)$ which corresponds to the beginning of the diffusive regime for the RDOF [Fig. 2.3(a)]. We note that there is a small maximum at $t \approx 10^{-2}$ ps: this is a consequence of the librational motion as shown in Fig. 2.3(a) [3]. By considering $t^*(T)$ we find that at all T the diffusive regime occurs for the RDOF at a slightly earlier time than for the TDOF. Figure 2.4(b) shows $G_s(\varphi,t)$ and $G_0(\varphi,t)$ for $T = 200$ K and $t = t^*(200K) \approx 1.05$ ns. As in [58] we find that $G_s(\varphi,t^*)$ and $G_0(\varphi,t^*)$ intersect for large φ at φ^*, and $G_s(\varphi,t^*)$ shows a large tail where the fitted Gaussian underestimate the angular motion of the molecules. Molecules with $\varphi > \varphi^*$ can be considered with an

---

[3] Note that for $t \to 0$, contrary to [58] for TDOF, $\alpha_2(t\to 0) \approx 0.37$. This value of α_2 can be obtained analytically from a Boltzmann distribution of a free rotator and noting that for short times $\vec{\varphi}_i(t) \simeq \vec{\omega}_i(t)\,\delta t$, where $\vec{\omega}_i$ is the angular velocity for the $i-$th molecule.

angular displacement higher than expected; this fraction $f \equiv \int_{\varphi^*}^{\infty} 4\pi\varphi^2 G_s(\varphi,t)$ is found to be $\approx 13\%$, showing a weak T-dependence.

In analogy to [40, 47, 58], we define the rotational mobility of a molecule at a given time t_0 as the maximum angular displacement in the interval $[t_0, t_0+\Delta t]$ of the oxygen atom

$$\Psi_i(t,\Delta t) \equiv \max\{|\vec{\varphi}_i(t+t_0) - \vec{\varphi}_i(t_0)|\,,\, t_0 \le t \le t_0+\Delta t\}\,. \qquad (2.24)$$

We focus our attention on the most rotationally mobile molecules and explore the possibility that there exist clusters also among this category of molecules. To facilitate comparison with the study [58] of translational heterogeneities (TH), we select the 7% of the most rotationally mobile molecules [4] and define a cluster at time t_0 over an observation time Δt as those molecules whose nearest neighbor oxygen-oxygen (O-O) distance at time t_0 is less than 0.315 nm (first minimum of O-O radial distribution function). We find that the rotational dynamics is spatially heterogeneous, since these molecules form clusters, which we will call rotational heterogeneities (RH). Furthermore, we obtain different clusters depending on which vector ($\hat{p}$, $\hat{q}$, or $\hat{r}$) we consider. We refer to these as $\hat{p}$- $\hat{q}$- $\hat{r}$-clusters.

Next we address the question of how these RH depend on the observation time. The weight average cluster size is $\langle n(\Delta t)\rangle_w \equiv \langle n^2(\Delta t)\rangle / \langle n(\Delta t)\rangle$ where $\langle n(\Delta t)\rangle$ is the average number of molecules in a cluster in a time Δt. To eliminate the contribution of random clusters, we normalize $\langle n(\Delta t)\rangle_w$ by $\langle n_r\rangle_w$, i.e., the weight average cluster size obtained by chosing randomly 7% of the molecules. Figure 2.5 shows $\langle n(\Delta t)\rangle_w / \langle n_r\rangle_w$ for $\hat{p}$-clusters as a function of Δt for different T (similar results hold for $\hat{q}$ and $\hat{r}$). In the same manner as the translational case, the maximum in $\langle n(\Delta t)\rangle_w / \langle n_r\rangle_w$ occurs at the end of the cage regime of the RMSD, indicating that the cage breaking of the RDOF is highly correlated with the cage breaking of TDOF. The RH become larger as T decreases. Figure 2.6(a) shows $\langle n(\Delta t)\rangle_w / \langle n_r\rangle_w$ for RH (obtained from $\hat{p}$, $\hat{q}$ or $\hat{r}$) and TH at the corresponding t_{max}, the time at which the corresponding weight average cluster size is largest. We find that on average TH are larger than RH, and that RH reach their maximum size before the TH, Fig. 2.6(b), i.e. t_{max} for RH is smaller than t_{max} for TH.

---

[4] Our results are not qualitatively effected by the choice of f, provided $f \lesssim 15\%$.

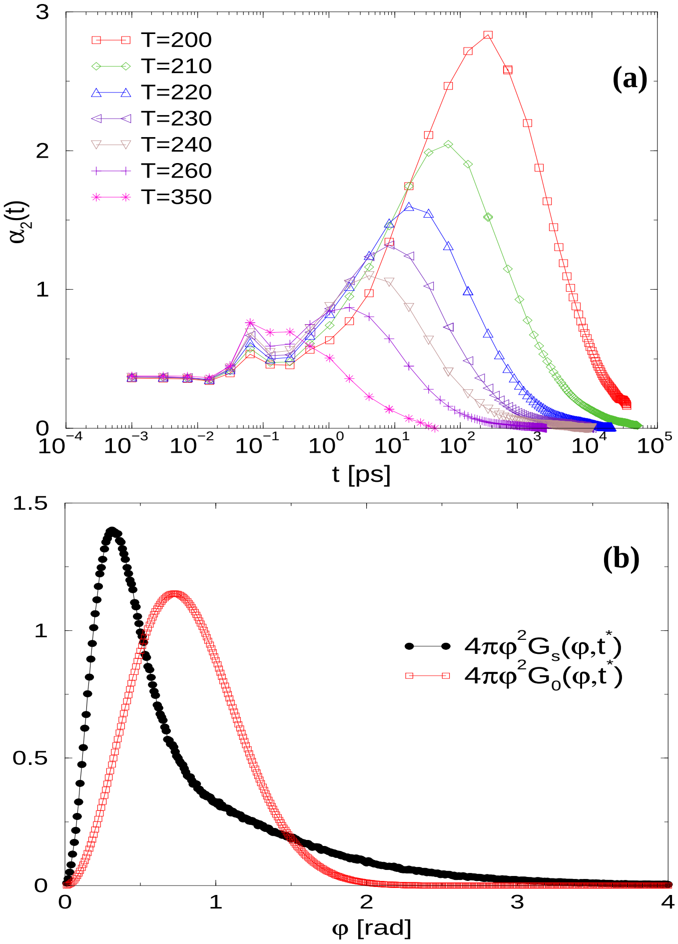

Figure 2.4: (a) Non-Gaussian parameter $\alpha_2(t)$ for the range of temperatures indicated. (b) Self part of the van Hove distribution function, $G_s(\varphi, t)$, for T = 200 K and $t^*(200\text{ K}) \approx 1.05$ ps, compared with the Gaussian approximation, $G_0(\varphi, t)$, obtained using $\langle\varphi^2(t^*)\rangle$ also at T = 200 K.

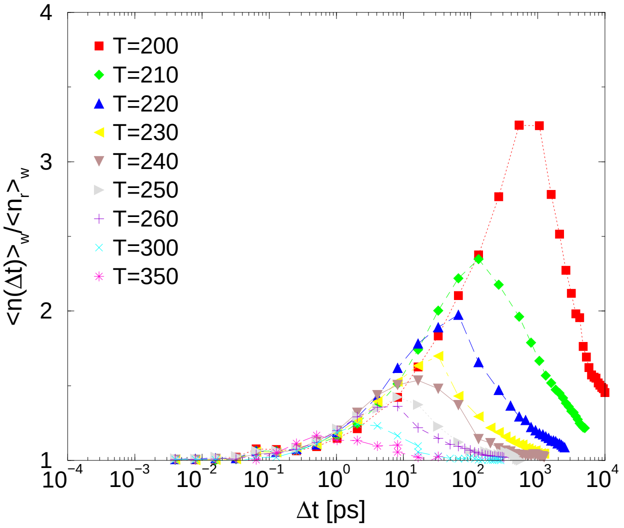

Figure 2.5: Weight average cluster size for T = 200 K − 350 K for molecules belonging to the 7% most rotationally mobile molecules. The values are normalized to the random cluster contribution.

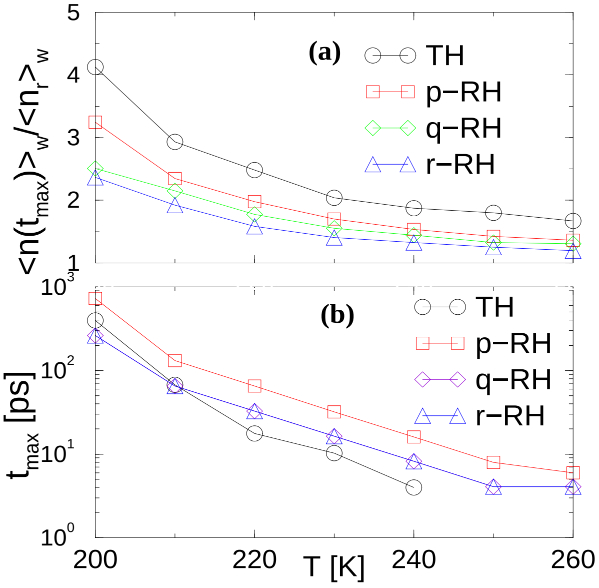

Figure 2.6: (a) Weight average cluster size as a function of temperature for TH and RH. Both quantities are calculated at the corresponding t_{max}. Note that the TH are larger than the RH. (b) The time t_{max} at which the maximum of the weight average cluster size occurs.

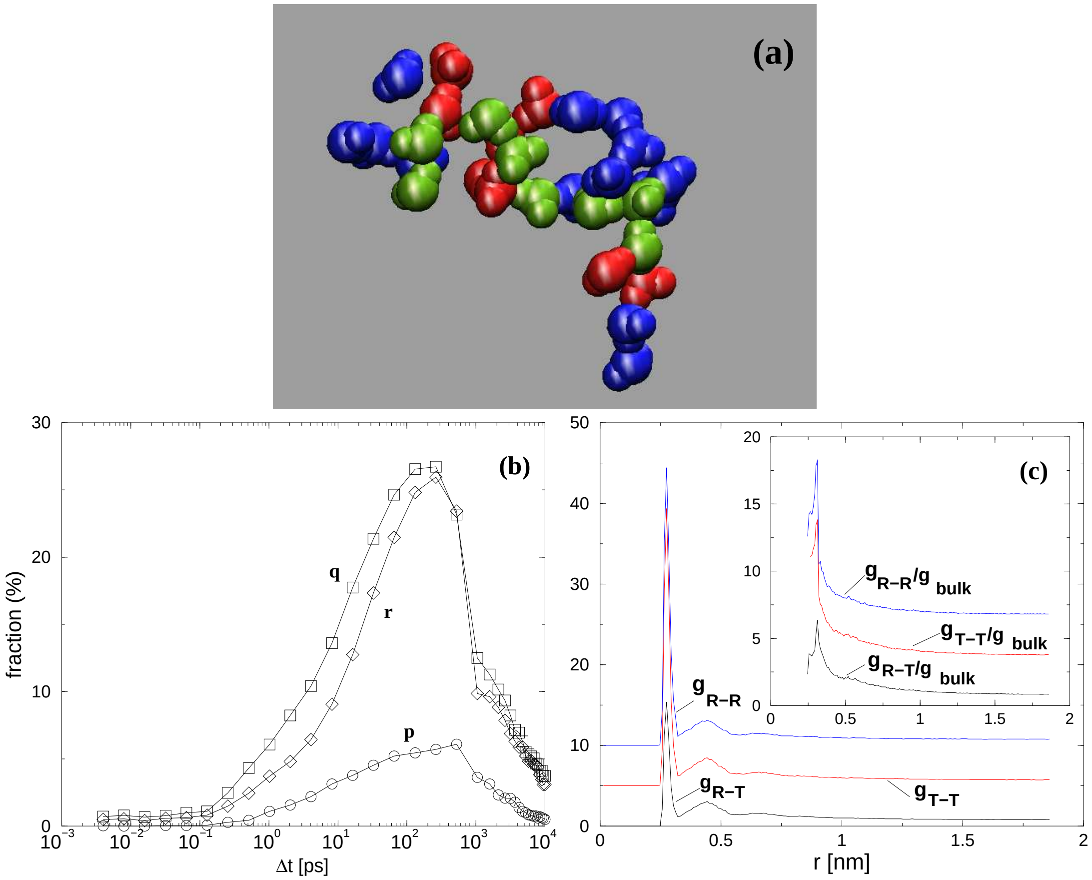

Figure 2.7: (a) A snapshot of a typical cluster at T = 200 K. The red molecules belong to TH, blue to RH and the green molecules belong to both clusters.(b) Fraction of molecules in both a TH and RH for the three principal vectors; the strongest correlations are for vectors $\hat{q}$ and $\hat{r}$. (c) RDF between the sets of translationally mobile and rotationally mobile molecules for T = 200 K. The inset shows the corresponding ratios of these functions to $g_{\mathrm{bulk}}(r)$. For clarity $g_{\mathrm{T-T}}$ is shifted by 5 and $g_{\mathrm{R-R}}$ by 10 on the vertical axis; the ratio involving $g_{\mathrm{T-T}}$ is shifted by 3 and the ratio involving $g_{\mathrm{R-R}}$ by 6 in the inset.

It is natural to ask to what extent the RH and TH are formed by the same molecules. We address this question by simultaneously analyzing the properties of RH and TH. We considered the RH defined from $\hat{p}$, but the same physical picture holds when using $\hat{q}$ or $\hat{r}$. Figure 2.7(a) is a typical snapshot of the system, showing both TH and RH. The clusters together form a larger entity characterizing the dynamical heterogeneities; the molecules belonging to both kinds of clusters act as the "backbone" of such an entity. We find that the fraction f_{RT} of molecules simultaneously belonging to both clusters increases with decreasing temperature. Figure 2.7(b) shows f_{RT} at the lowest temperature simulated, for the three kinds of RH. We observe that the maximum value of f_{RT} is 6% for the case of $\hat{p}$, while this value becomes 27% for $\hat{q}$ or $\hat{r}$. Thus the $\hat{q}$- and $\hat{r}$-clusters couple more strongly with the TH clusters.

To compare the structure of the TH and RH, we evaluate the radial distribution function (RDF) of oxygen atoms within each kind of cluster, and between the two kinds of clusters. Figure 2.7(c) shows the RDF for TH, for RH (defined from $\hat{p}$, but the same results are obtained by using $\hat{q}$ or $\hat{r}$), and for molecules which belong to *both* TH and RH. We see that there is a strong tendency for mobile molecules (of either type) to be neighbors. The RDF's are qualitatively similar to the bulk RDF, $g_{\text{bulk}}(r)$, with maxima at $r \approx 0.28$ nm and $r \approx 0.45$ nm (i.e., molecules are nearest or next-nearest neighbors); however, the amplitudes of the first peak are strongly enhanced compared to bulk water. In order to examine deviations from the bulk we normalize the RDF's by $g_{\text{bulk}}(r)$ [inset of Fig. 2.7(c)]. All of the RDF's display maxima at 0.32 nm, indicating that oxygens in TH and RH have an enhanced tendency (with respect to the bulk) to be in the first interstitial shells of each other and, therefore, have more than four nearest neighbors. Molecules with five or more neighbors have bifurcated bonds and represent "defects" in the tetrahedral network characterizing water [66, 67]. Therefore, our results suggest that the combined TH and RH in water (i) are a consequence of the defects of the HB network, and (ii) are primarily composed by molecules located at the defects of the HB network: evidence of the relation between the structure and dynamics in water. Thus the physical picture needed to describe rotational heterogeneities resembles that needed for describing translational heterogeneities.

Chapter 3

Role of dynamical heterogeneities on diffusivity

At temperatures where liquids have a diffusion constant similar to that of ambient temperature water, the translational and rotational diffusion, D_t and D_r respectively, are well described by the Stokes-Einstein (SE) relation [68]

$$D_t = \frac{k_B T}{6\pi\eta R} \tag{3.1}$$

and the Stokes-Einstein-Debye (SED) relation [69]

$$D_r = \frac{k_B T}{8\pi\eta R^3}. \tag{3.2}$$

Here T is the temperature, η the viscosity, k_B the Boltzmann constant and R is the "molecular" radius. These equations are derived by a combination of classical hydrodynamics (Stokes Law) and simple kinetic theory (e.g, the Einstein relation) [70]. Recently, the limits of the SE and SED relations have been an active field of experimental [32, 71–75], theoretical [76–83] and computational [61, 84–94] research. The general consensus is that the SE and SED relations hold for low-molecular-weight liquids for $T \gtrsim 1.5T_g$, where T_g is the glass transition temperature. For $T \lesssim 1.5T_g$, deviations from either one or both of the SE and SED relations are observed. Experimentally, it is found that the SE relation holds for many liquids in their stable and weakly supercooled regimes, but when the liquid is deeply supercooled it overestimates D_t relative to η by as much as two or three orders of magnitude, a phenomenon usually referred to as the "breakdown" of the SE relation. The situation for the SED relation is more complex. Some experimental studies found agreement with the predicted values of the SED relation even for deeply supercooled liquids [32, 45, 46], while others claim also a breakdown of the SED relation to the same extent as for the SE relation [72, 95–98]. The failure of these relations provides a clear indication of a fundamental change in the dynamics and relaxation of the system. Indeed, the changing dynamics of the liquid as it approaches the glass transition is well documented, but not yet fully understood [7, 99–101].

There is a growing body of evidence [47, 102–106] that, upon cooling, a liquid does not become a glass in a spatially homogeneous fashion. Instead the system is characterized by the appearance of dynamical heterogeneities [45–47, 50, 51, 54, 102–114]. This phenomenon is often called "spatially heterogeneous dynamics", since there are spatial regions in which the structural relaxation time can differ by orders of magnitude from the average over the entire system [1]. In the "dynamical heterogeneities" (DH) view, the motion of atoms or molecules is highly spatially correlated. The presence of these DH has been argued to give rise to the breakdown of the SE relation [76, 81]. Since the derivation of the Einstein relation assumes uncorrelated motion of particles, it is reasonable that the emergence of correlations could result in a failure of the SE relation. The aim of the present work is to assess the validity of the SE and SED relations in the SPC/E model of water, and consider to what extent the DH contribute to the SE and SED breakdown.

Computer simulations have been particularly useful for studying DH (e.g., see Refs. [33, 34, 36, 39, 58, 115–118]) since simulations have direct access to the details of the molecular motion. For water, the existence of regions of enhanced or reduced mobility has also been identified [58, 119]. In particular, Ref. [58] identifies the clusters of molecules with greater *translational* (or center of mass) mobility with the hypothesized "cooperatively rearranging regions" of the Adam-Gibbs approach [19, 120]. For water, those DH are also accompanied by spatial heterogeneities [121, 122]

---

[1] First suggested by G. Tammann, *Der Glasszustand* (Leopold Voss, Leipzig, 1933).

Most computer simulation studies on DH describe these heterogeneities based on the particle or molecule translational degrees of freedom. We will refer to these DH as translational heterogeneities (TH). For water, it is also necessary to consider the rotational degrees of freedom of the molecule. Recently, some computer simulation studies on molecular systems described the DH based on the molecular *rotational* degrees of freedom [59, 61, 71, 84, 123–125]. We will refer to these DH as rotational heterogeneities (RH). For the case of a molecular model of water, RH were studied [125] and it was found that RH and TH are spatially correlated. This work extends those results. We find support for the idea that TH are connected to the failure of the SE relation, and further that RH have a similar effect on SED relation. Additionally, we find that the breakdown of these relations is accompanied by the decoupling of the translational and rotational motion.

This work is organized as follows. In the next section we describe the water model and simulation details. In Sec. 3.2 and Sec. 3.3 we test the validity of the SE and SED relations and their connection with the presence of DH, respectively. The decoupling between rotational and translation motion is studied in Sec. 3.6. In Sec. 3.7 we explore the role of time scale in the breakdown of the SE and SED relations and decoupling of rotational and translational motion. We summarize our results in Sec. 3.10. We have placed some technical aspects of the work in appendices to facilitate the flow of our results.

3.1 Model and Simulation Method

We perform molecular dynamics (MD) simulations of the SPC/E model of water [48]. This model assumes a rigid geometry for the water molecule, with three interaction sites corresponding to the centers of the hydrogen (H) and oxygen (O) atoms. Each hydrogen has a charge $q_H = 0.4238\ e$, and the oxygen charge is $q_O = -2.0\ q_H$, where e is the magnitude of the electron charge. The OH distance is 1.0 Å and the HOH angle is 109.47°, corresponding to the tetrahedral angle. In addition to the Coulombic interactions, a Lennard-Jones interaction is present between oxygen atoms of two different molecules; the Lennard-Jones parameters are $\sigma = 3.166$ Å and $\epsilon = 0.6502$ kJ/mol. We use a cutoff distance of $2.5\sigma = 7.915$ Å for the pair interactions and the reaction field technique [126] is used to treat the long range Coulombic interactions.

We perform simulations in the constant particle number, N, volume, V, and temperature NVT ensemble with $N = 1728$ water molecules and fixed density $\rho = 1.0$ g/cm^3. The values of the simulated temperature are $T = 210$, 220, 230, 240, 250, 260, 270, 280, 290, 300, 310, 330 and 350 K. We use the Berendsen method [127] to keep the temperature constant [2]. We use periodic boundary conditions and a simulation time step of 1 fs. To ensure that simulations attain a steady-state equilibrium, we perform equilibration simulations for at least the duration specified by Ref. [23]. After these equilibration runs we continue with production runs of equal duration during which we store the coordinates of all atoms for data analysis. To improve the statistics of our results, we have performed 5 independent simulations for each T. Ref. [23] provides further details of the simulation protocol.

3.2 Breakdown of the Stokes-Einstein and Stokes-Einstein-Debye relations

To assess the validity of the SE and SED relations we consider a simple rearrangement of Eqs. (3.1) and (3.2), *i.e.* we define the SE ratio

$$R_{\mathrm{SE}} \equiv \frac{D_t \eta}{T} \tag{3.3}$$

and the SED ratio

$$R_{\mathrm{SED}} \equiv \frac{D_r \eta}{T}. \tag{3.4}$$

Both R_{SE} and R_{SED} will be temperature-independent if the SE and SED relations are valid.

To evaluate R_{SE} and R_{SED}, we must first calculate the appropriate diffusion constants. Following normal procedure, we define

$$D_t \equiv \lim_{\Delta t \to \infty} \frac{1}{6\Delta t} \langle r^2(\Delta t) \rangle. \tag{3.5}$$

---

[2] Although it is desirable to simulate in the microcanonical ensemble (NVE), for long simulations a small energy drift is unavoidable. To correct this situation, the Berendsen thermostat was employed with a very long time constant $\tau = 200$ ps. For an interesting discussion on the relation between the Berendsen thermostat and canonical and microcanonical ensembles, see T. Morishita, J. Chem. Phys. **113**, 2976 (2000).

where $\langle r^2(\Delta t)\rangle$ is the translational mean square displacement (MSD) of the oxygen atoms

$$\langle r^2(\Delta t)\rangle \equiv \frac{1}{N}\sum_{i=0}^{N} |\vec{r}_i(t') - \vec{r}_i(t)|^2. \tag{3.6}$$

Here, $\vec{r}_i(t)$ and $\vec{r}_i(t')$ are the positions of the oxygen atom of molecule i at time t and t' respectively, and $\Delta t = t' - t$. Analogously, we define the rotational diffusion coefficient

$$D_r \equiv \lim_{\Delta t\to\infty} \frac{1}{4\Delta t}\langle \varphi^2(\Delta t)\rangle, \tag{3.7}$$

where $\langle \varphi^2(\Delta t)\rangle$ is the rotational mean square displacement (RMSD) for the vector rotational displacement $\vec{\varphi}_i(\Delta t)$. Special care must be taken to calculate $\langle \varphi^2(\Delta t)\rangle$ so that it is unbounded. A detailed discussion of this procedure is provided in Appendix 3.11.1.

We also need the viscosity η to evaluate R_{SE} and R_{SED}. Unfortunately, accurate calculation of η is computationally challenging. A frequently employed approximation exploits the fact that η is proportional to the shear stress relaxation time, τ_s, via the infinite frequency shear modulus, G_∞, which is nearly T-independent [49]. Additionally, we expect that τ_s (a "collective property") should be nearly proportional to other collective relaxation times, such as the relaxation time τ defined from the coherent intermediate scattering function, $F(q, \Delta t)$, where q is the wave vector. Therefore, we substitute η by τ, which should only affect the value and units of the constants in the R_{SE} and R_{SED}. For the purposes of our calculations, we define τ by fitting $F(q, \Delta t)$ at long times with a "stretched" exponential

$$F(q, \Delta t) \sim \exp\left[-(\Delta t/\tau)^{\beta}\right], \tag{3.8}$$

where $0 < \beta < 1$, and we focus on the q value corresponding to the first peak in the static structure factor $S(q)$.

Now that we have the necessary quantities, we show R_{SE} and R_{SED} in Fig. 3.1(a) and Fig. 3.1(b) with the curves labelled with "all". Both quantities deviate at low T from the corresponding constant values reached at high temperature indicating a breakdown of both the SE and SED relations.

Whether there is a breakdown of the SED relation in experiments is not clear. While some experiments measuring dipole relaxation times show that the SED relation holds down

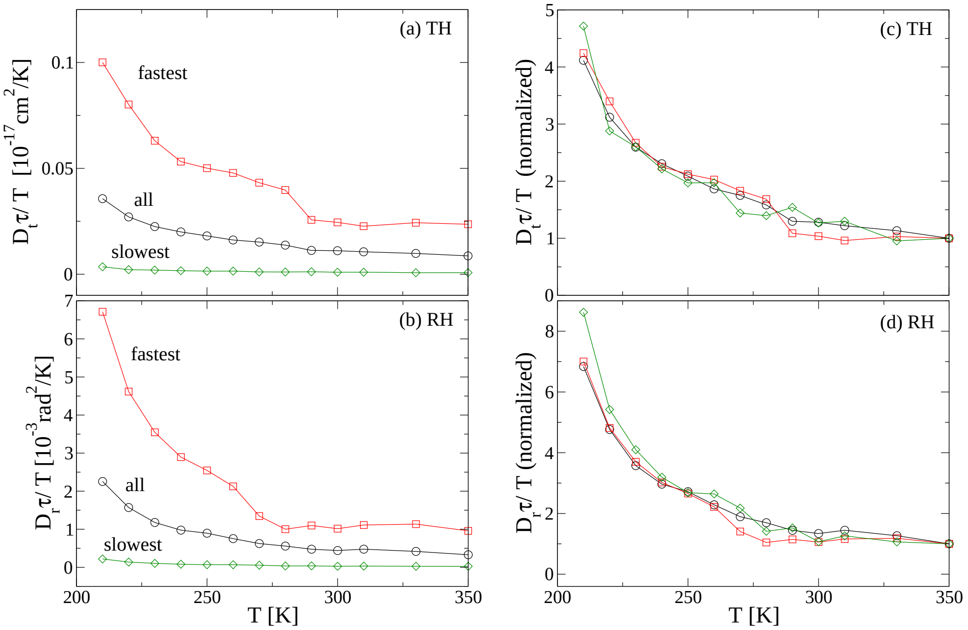

Figure 3.1: (a) Stokes–Einstein ratio, $D_t\tau/T$, for the 7% most translationally mobile molecules ("fastest"), for the 7% least translationally mobile molecules ("slowest"), and for the entire system (all). There is a breakdown of the Stokes-Einstein relation (constant Stokes-Einstein ratio) at low temperatures in both the fastest and slowest subsets, as well as for the entire system. (b) Stokes-Einstein-Debye ratio, $D_r\tau/T$, for the 7% most rotationally mobile molecules, for the 7% least rotationally mobile molecules, and for the entire system (all). Similar to (a), there is a breakdown of the Stokes-Einstein-Debye relation (constant Stokes-Einstein-Debye ratio). (c) and (d) Normalization of the curves in (a) and (b), respectively, by the corresponding quantities at $T = 350$ K. The collapse of these curves demonstrates that the relative deviations from the Stokes-Einstein and Stokes-Einstein-Debye relations are approximately the same for the corresponding mobility subsets.

to the glass transition [45, 46], other experiments [128] show that the SED relation fails for low T. Our simulations are in agreement with the breakdown of the SED ratio observed in, e.g., Ref. [87]. Figures 3.1(a) and 3.1(b) also show R_{SE} and R_{SED} for different subsets of molecules to examine the role played by DH. This is discussed in the following Section.

3.3 Identifying mobility subsets

Many theoretical approaches (e.g. [76, 81, 129]) attempt to explain the breakdown of SE and/or SED in terms of DH. To this end, we must first describe the procedure used to select molecules whose motion (or lack thereof) is spatially correlated. A variety of approaches have been used to probe the phenomenon of DH. Here we use one of the most common techniques: partitioning a system into mobility groups based on their rotational or translational maximum displacement.

For the TH, we define the translational mobility, μ_i, of a molecule i at a given time t_0 and for an observation time Δt, as the maximum displacement over the time interval $[t_0, t_0 + \Delta t]$ of its oxygen atom [40]

$$\mu_i(t_0, \Delta t) \equiv \max\{|\vec{r}_i(t + t_0) - \vec{r}_i(t_0)| \, , \, t_0 \leq t \leq t_0 + \Delta t\}. \tag{3.9}$$

For the RH, following [125], we define a rotational mobility that is analogous to the translational case. In analogy with Eq. (3.9), we define the rotational mobility at time t_0 with an observation time Δt as

$$\psi_i(t_0, \Delta t) \equiv \max\{|\vec{\varphi}_i(t + t_0) - \vec{\varphi}_i(t_0)| \, , \, t_0 \leq t \leq t_0 + \Delta t\} \, . \tag{3.10}$$

We identify the subsets of rotationally and translationally "fastest" molecules as the 7% of the molecules with largest ψ_i and μ_i, respectively. Analogously, we identify the subsets of rotationally and translationally "slowest" molecules as the 7% of the molecules with smallest ψ_i and μ_i, respectively. The choice of 7% is made to have a direct comparison with the analysis of Ref. [58, 125], but the qualitative details of our work are unaffected by modest changes in this percentage. In the following, we will refer to these subsets of molecules as

TH and RH, fastest and slowest, depending on whether we consider the top or the bottom of the distribution of mobilities. We will see that comparing the fastest and the slowest molecules will reveal new features of DH.

3.4 Stokes-Einstein and Stokes-Einstein-Debye relations for fastest and slowest molecules

Having identified subsets of highly mobile or immobile molecules, we can calculate the ratios R_{SE} and R_{SED} by limiting the evaluation of D_t, D_r and τ to these subsets. This is relatively straightforward for the diffusion constants, since they depend only on single molecule averages. For τ, the situation is more complex since $F(q, \Delta t)$ includes cross-correlations between molecules. Hence we specialize the definition of $F(q, \Delta t)$ for the TH and RH subsets by introducing a definition that captures the cross-correlation within subsets and between a subset and rest of the system. We call this function $F_{\mathrm{subset}}(q, \Delta t)$, which we discuss in detail in Appendix 3.11.2.

We show the value of R_{SE} and R_{SED} in Fig. 3.1(a) and 3.1(b) for the cases when only the fastest and slowest subsets of molecules are considered. Like the total system average, both the SE and SED ratios for the subsets deviate at low T from the corresponding constant value reached at high temperature. Therefore, we observe that the breakdowns of both the SE and SED relations occur not only in the subset of the fastest molecules, but also in the slowest. We have also confirmed a breakdown in intermediate subsets.

The most mobile subset of molecules has a consistently greater value of $D_t\tau/T$ and $D_r\tau/T$ than the rest of the system, while the ratios for the least mobile subsets are always smaller. This is a result of the fact that the means by which we select the different subsets most strongly affects the diffusion constant (see Appendix 3.11.2), and hence the differences in the SE and SED ratios between the full system and the subsets are dominated by the diffusion constant, rather than by the relaxation time.

In order to compare the relative deviations of these curves from the SE and SED predictions, we normalize R_{SE} and R_{SED} by their respective high temperature values [Fig. 3.1(c) and 3.1(d)]. We observe that there is a collapse of all the curves; thus, we conclude that both the most and least mobile molecules contribute in the same fashion to the breakdown of SE and SED. Moreover, this result supports the scenario that the deviation from the SE and SED relations cannot be attributed to only one particular subset of fastest/slowest molecules, but to all scales of translational and rotational mobility. We have confirmed this by looking at subsets of intermediate mobility (not shown). Therefore, we interpret our results as a sign of a "generalized breakdown" in the system under study, in contrast to a picture where only the most mobile molecules are the origin of the breakdown of SE and SED, embedded in an inactive background where the SE and SED equations hold (see e.g. [32]). These results are consistent with the results of Ref. [87], who arrived at the same conclusion via a different analysis.

3.5 Fractional Stokes-Einstein and Stokes-Einstein-Debye relations

When the SE and SED relations fail, it is frequently observed that they can be replaced by *fractional* functional forms [71, 73, 95, 130–135]

$$D_t \sim \left(\frac{\tau}{T}\right)^{-\xi_t}, \quad D_r \sim \left(\frac{\tau}{T}\right)^{-\xi_r} \tag{3.11}$$

with $\xi_t < 1$ and $\xi_r < 1$. Hence we test to what degree Eqs. (3.11) hold for our system. In Fig. 3.2 we show a parametric plot of diffusivity versus τ/T for the entire system, and for the fastest and slowest molecules composing the TH and RH. The results at low temperature are well fit with the fractional form of SE and SED relations. From Fig. 3.2, ξ_t for TH is $0.83, 0.84, 0.84$ for fastest, slowest, and all, respectively, so all TH have approximately the same exponent. Similarly, for RH we find that ξ_r is $0.75, 0.76, 0.75$ for fastest, slowest, and all, respectively.

Reference [87] found a stronger form of this fractional relation. Specifically, Ref. [87] examined an "ensemble" of systems of the ST2 water model at the same T, which by

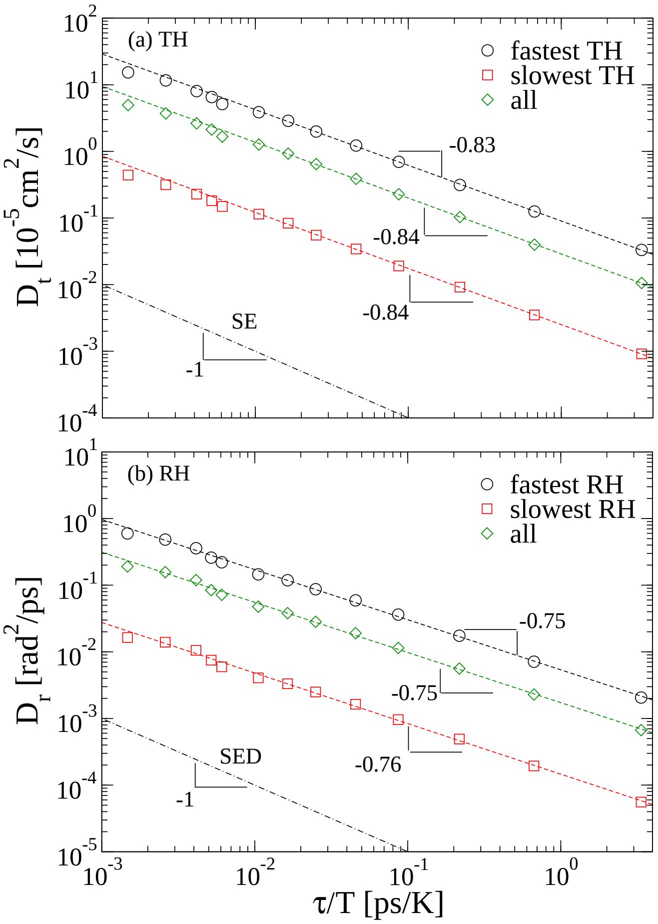

Figure 3.2: (a) Power law fits of translational diffusivity D_t as functions of τ/T, $D_t \sim (\tau/T)^{-\xi_t}$, for the eight values of temperature $T = 210 \ldots\ 280$ K (but not for the remaining values $T = 290 \ldots\ 350$ K), for fastest translational heterogeneities (TH), slowest TH, and all molecules. We estimate $\xi_t \approx 0.84$. The dot-dashed line represents the normal Stokes–Einstein behavior ($\xi_t = 1$). Consistently with the results of Fig. 3.1, the deviation of these three curves from the Stokes–Einstein behavior is almost identical as reflected in the values of these fractional exponents. (b) Power law fits of rotational diffusivity, D_r, as functions of τ/T, $D_r \sim (\tau/T)^{-\xi_r}$, of simulations in the same temperature range of (a) for fastest rotational heterogeneities (RH), slowest RH, and all molecules. We estimate $\xi_r \approx 0.75$. The dot-dashed line represents the normal Stokes–Einstein–Debye behavior ($\xi_r = 1$). Also for RH, a fractional law is found with the same exponents for the three families considered, and, noticeably, the deviation from the normal case ($\xi_r = 1$), is stronger for D_r than for D_t, since $\xi_r < \xi_t$.

statistical variation have fluctuations in the SE and SED ratios. Nonetheless, all systems collapsed to the same master curve when plotted in the parametric form shown in Fig. 3.2, meaning that the systems dominated by mobile or immobile molecules collapse to the same curve. While Ref. [87] employed a very different method (small systems followed for shorter times), the conclusion of our Fig. 3.2 is the same: a generalized deviation from SE and SED. However, Fig. 3.2 clearly shows that we do not find a general collapse in our present calculation. To understand why, we return to the fact that the method by which we define mobility affects much more strongly the diffusion constants than the coherent relaxation time, τ. As a result, it is impossible to have the results for the mobile and immobile subsets to collapse to a single master curve. To observe the same collapse, presumably one needs a more "neutral" method for selecting the mobile particles—that is one that does not explicitly bias toward a specific property. Unfortunately, such an approach is not obvious. However, we reproduced the ensemble approach of Ref. [87], by splitting each of our 5 simulations into 3 trajectories. We obtain reasonable fluctuations that allow us to test and confirm (not shown) the observation of collapse of Ref. [87]. Hence, the phenomenon of homogeneous breakdown of SE and SED appears to be robust for the different water models.

3.6 Decoupling of translational and rotational motions

The SE and SED relations also imply a coupling between rotational and translational motion. Specifically, Eqs. (3.1) and (3.2) imply that the ratio

$$\frac{D_r}{D_t} = \frac{3}{4R^2} \tag{3.12}$$

should remain constant as a function of temperature. Since we have already seen that the SE and SED ratios are not obeyed, it is likely that the ratio D_r/D_t is also violated [136]. However, it is also possible that D_r/D_t remains constant if both D_r and D_t deviate from their expected behavior in the same way.

Figure 3.3(a) shows D_r/D_t as a function of temperature. As T decreases, we observe that

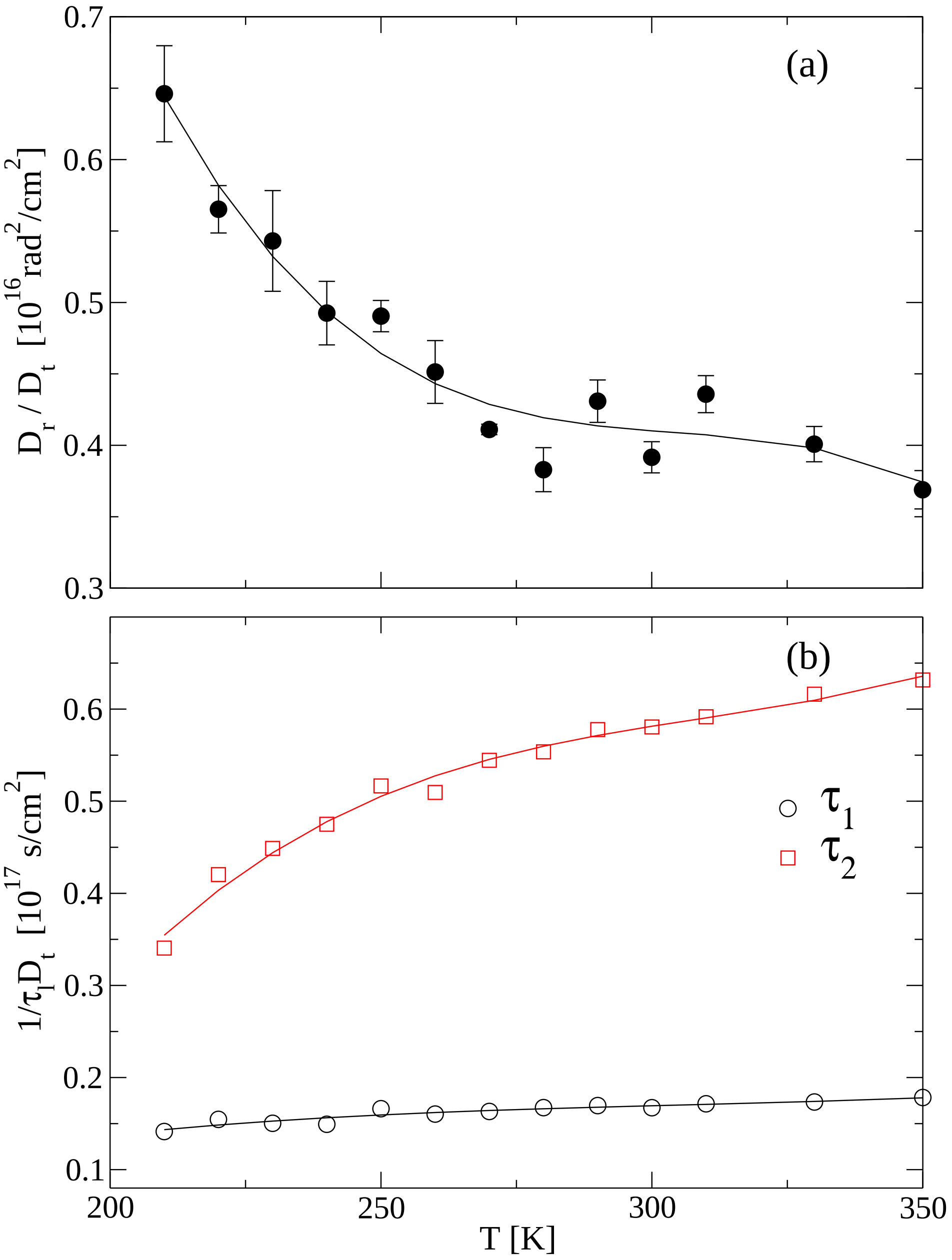

Figure 3.3: (a) The ratio of rotational and translational diffusivities D_r/D_t as a function of temperature. As temperature decreases, this ratio increases indicating a decoupling between rotation and translational motion. The deviation of D_r is stronger than that of D_t. The line is a guide for the eye. (b) Same as (a) where the rotational diffusivity, D_r, is replaced by the inverse of the rotational relaxation time, τ_ℓ with $\ell = 1, 2$, as usually done in experiments. An opposite decoupling is observed in (a) and (b). The lines are guides for the eye.

D_r/D_t increases, which implies that the breakdown of the SED relation is more pronounced than that of the SE relation.

Experiments generally do not examine the behavior of D_r/D_t since D_r is not accessible. Instead, D_r is usually replaced by $(\tau_\ell)^{-1}$ with $\ell = 2$ [85]. Here, τ_ℓ is the relaxation time of the rotational correlation function

$$C_\ell(\Delta t) \equiv \langle P_\ell(\cos[\hat{p}(t) \cdot \hat{p}(t + \Delta t)])\rangle, \tag{3.13}$$

where $P_\ell(x)$ is the Legendre polynomial of order ℓ, and $\hat{p}(t)$ is defined in Appendix 3.11.1. Figure 3.3(b) shows $(\tau_\ell)^{-1}/D_t$ for $\ell = 1, 2$. We observe that $(\tau_\ell)^{-1}/D_t$ also shows a decoupling between rotational and translational motion. However, while D_r/D_t *increases* upon cooling, $(\tau_\ell)^{-1}/D_t$ *decreases* upon cooling. MD simulations using an *ortho*-terphenyl (OTP) model [137] and the ST2 water model [87] also find a qualitatively similar temperature dependence of decoupling of the SE and SED relations depending on whether D_r or τ_2 is used. In the simulations of OTP, it was shown that the inverse relation between D_r and τ_2 fails due to the caging of the rotational motion; this caging results in intermittent large rotations that are not accounted for by the Debye approximation.

Similar to the analysis of the breakdown of the SE and SED ratios, we can test whether DH play a strong role in the decoupling by examining the ratio D_r/D_t for the different mobility subsets. This is slightly complicated by the fact that we can choose mixed mobility subsets when calculating the ratio. Figure 3.4 shows that the ratio D_r/D_t for all choices of mobility subsets approximately coincide when scaled by the high temperature behavior of D_r/D_t. This indicates that (like the breakdown of the SE and SED relations) the decoupling is uniform across the subsets of mobility.

3.7 Time scales: time dependent Stokes-Einstein and Stokes-Einstein-Debye relations

The SE and SED relations depend on D and η, which are defined only in the asymptotic limit of infinite time. In contrast, the time scale on which DH exist is finite, and generally

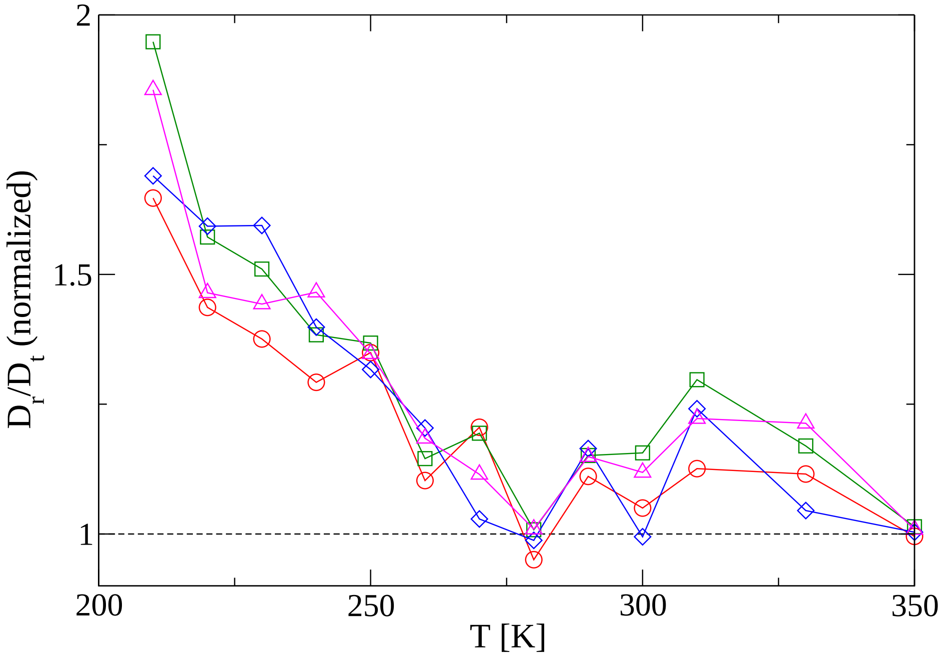

Figure 3.4: The ratio of rotational and translational diffusivities, D_r and D_t respectively, for the following choices of subsets: D_r for fastest translational heterogeneities (TH) divided by D_t for fastest TH ($\Diamond$), D_r for slowest TH divided by D_t for slowest TH ($\triangle$), D_r for fastest rotational heterogeneities (RH) divided by D_t for fastest RH ($\bigcirc$), D_r for slowest RH divided by D_t for slowest RH ($\Box$). The values were normalized by the $T = 350$ K values for every curve. The fact that for these four cases D_r/D_t deviates from unity (dashed line) to approximately the same degree indicates that the decoupling occurs across all four cases.

shorter that the time scale on which the system becomes diffusive. As a result, making the connection between DH and the breakdown of SE and SED expressions is difficult. To address this complication, we incorporate a time dependence in the SE and SED relations, so that we can evaluate these relations at the time scale of the DH. This point has been neglected so far in the literature. To define time-dependent versions of the SE and SED ratios, we first define time-dependent diffusivities

$$D_t(\Delta t) \equiv \frac{\langle r^2(\Delta t)\rangle}{6\Delta t}\,,\ D_r(\Delta t) \equiv \frac{\langle \varphi^2(\Delta t)\rangle}{4\Delta t}, \tag{3.14}$$

and we also define time-dependent relaxation times

$$\tau(\Delta t) \equiv \int_t^{t+\Delta t} F(q,t')dt'\,. \tag{3.15}$$

Note that $D_t(\Delta t) \to D_t$ and $D_r(\Delta t) \to D_r$ in the limit $\Delta t \to \infty$. The definition of $\tau(\Delta t)$ requires some explanation: $\tau(\Delta t)$ is the time integral of the intermediate scattering function, and $\tau(\Delta t)$ will be proportional to the standard relaxation time τ [Eq. (3.8)] in the limit $\Delta t \to \infty$. There is a constant of proportionality resulting from the stretched exponential form [3]. When, instead, a DH is considered, $F_{\mathrm{subset}}(q,\Delta t)$ [see Eq. (3.23)] is used in the computation of $\tau(\Delta t)$. We choose these definitions since, in the limit $\Delta t \to \infty$, they converge or are proportional to the corresponding time-independent definitions. We will use these time-dependent quantities to examine time-dependent generalizations of R_{SE} [Eq. (3.3)] and R_{SED} [Eq. (3.4)].

3.8 Breakdown time scale

Analyzing the time-dependent ratio $D(\Delta t)\tau(\Delta t)/T$ (for either rotational or translational motion) allows one to verify quantitatively the role of the time scale in the SE/SED ratios. To contrast the behavior of $D(\Delta t)\tau(\Delta t)/T$ with the average over the entire system, we define the time dependent "breakdown" ratios as follows:

$$b_{\mathrm{TH}}(\Delta t) \equiv \frac{(D(\Delta t)\tau(\Delta t)/T)_{\mathrm{TH}}}{(D(\Delta t)\tau(\Delta t)/T)_{\mathrm{all}}} \tag{3.16}$$

---

[3] Assuming a Kohlrausch form for the intermediate scattering function, $\exp(-t/\tau)^{\beta}$, the integral will yield $\tau(\infty) = \tau\Gamma(\beta^{-1})/\beta$, where $\Gamma(x)$ is the Euler Gamma function.

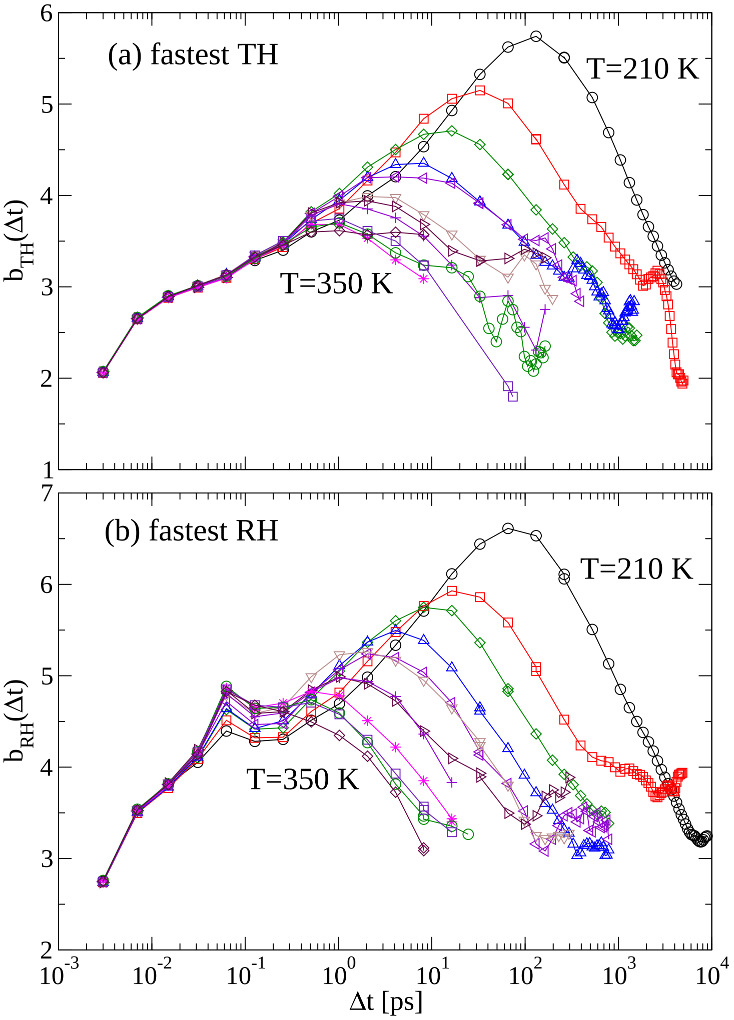

Figure 3.5: (a) Time-dependent extension, $b_{\mathrm{TH}}(\Delta t)$, of the Stokes–Einstein relation for the fastest translational heterogeneities (TH) at different T. For the sake of clarity the curve corresponding to $T = 290$ K was removed. (b) Time-dependent extension, $b_{\mathrm{RH}}(\Delta t)$, of the Stokes–Einstein–Debye relation for the fastest rotational heterogeneities (RH) at different T. For the sake of clarity the curve corresponding to $T = 290$ K was removed. In both (a) and (b), the maxima occur at the time scales corresponding to the end of the cage regime, when DH are more pronounced. These maxima increase upon cooling, as the DH become more pronounced.

and similarly

$$b_{\mathrm{RH}}(\Delta t) \equiv \frac{(D(\Delta t)\tau(\Delta t)/T)_{\mathrm{RH}}}{(D(\Delta t)\tau(\Delta t)/T)_{\mathrm{all}}} \tag{3.17}$$

If the DH are related to the breakdown of the SE and SED relations, then one would expect that: (i) the b_{TH} and b_{RH} ratios will show the largest deviations from the system average behavior at the time scale when DH are most pronounced, i.e. approximately at a time which we denote as t^*, at which the non-Gaussian parameter is a maximum (see Appendix 3.11.3). (ii) The lower the T, the larger the peak of b_{DH} is (in agreement with the fact that the DH are more pronounced as T decreases). Figure 3.5(a) for TH and Fig. 3.5(b) for RH, show the behavior of $b_{\mathrm{DH}}(\Delta t)$ for the fastest subset of molecules, for different temperatures. Both expectations (i) and (ii) agree with Fig. 3.5.

From Fig. 3.5 we can extract the time t_b when $b_{\mathrm{DH}}(\Delta t)$ is a maximum. Figure 3.6(a) shows t_b for each of the four subsets: TH fastest/slowest and RH fastest/slowest. If DH play a significant role in the breakdown of the SE and SED relations, we would expect that the maximum contribution to the deviation from the SE and SED relations, occurring at t_b, coincides roughly with the "classical" measure of the characteristic time of DH, t^*. Comparison of Fig. 3.6(a) and Fig. 3.6(b) for $T < 280$ K shows that t^* is slightly larger than t_b for the slowest DH, while is shorter than t_b for fastest DH. Nonetheless, t_b and t^* are approximately the same, and so the largest contribution to the SE/SED ratio is on the time scale when DH are most pronounced. This provides direct evidence for the idea that the appearance of DH is accompanied by the failure of the SE and SED ratios.

3.9 Decoupling time scales

We next directly probe the relation between DH and the decoupling of D_r and D_t. As discussed above, the time scale at which the DH are observable is much smaller than the time scale at which the system is considered diffusive. Therefore, in analogy to the previous section, we incorporate a time scale in the D_r/D_t ratio so that we can compare the decoupling between rotation and translation at the time scale of the DH. To this end we

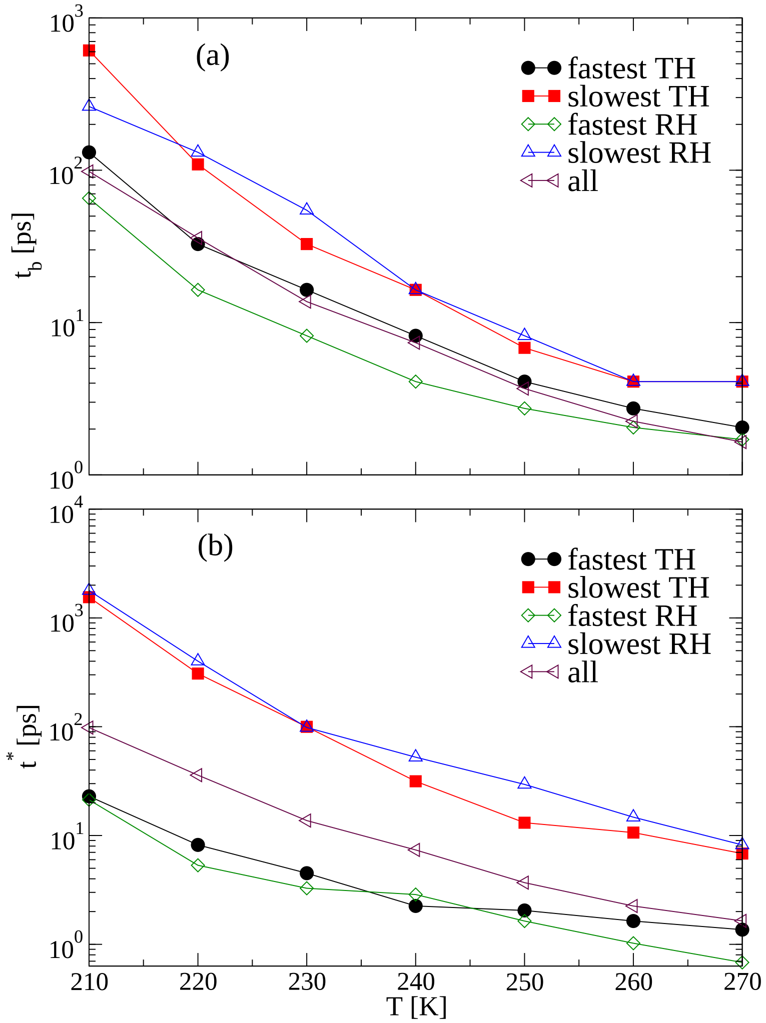

Figure 3.6: Temperature dependence of (a) t_b, the time at which the time-dependent extensions of the Stokes–Einstein and Stokes–Einstein–Debye relations, b_{TH} and b_{RH} respectively, have maxima, and (b) t^*, the time at which the non–Gaussian parameter, $\alpha_2(\Delta t)$, reaches a maximum. t^* indicates the time scale corresponding to the end of the cage regime. We show the results when considering molecules belonging to translational heterogeneities, rotational heterogeneities, and also for the entire system.

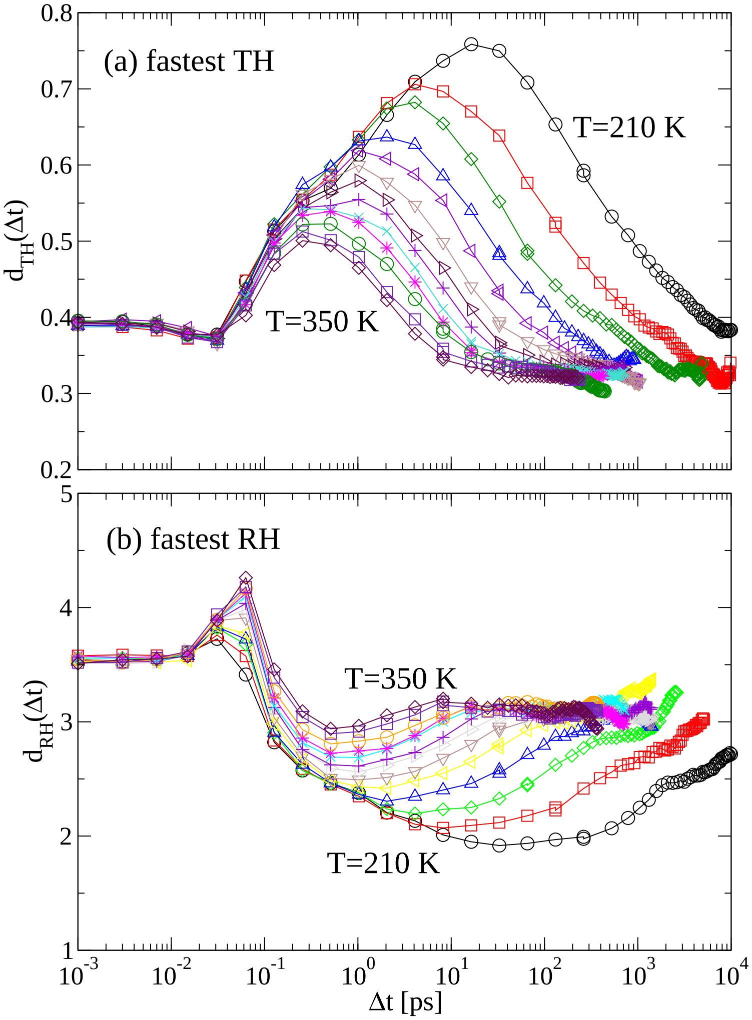

Figure 3.7: (a) Temporal behavior of the ratio of the time-dependent rotational diffusivity and translational diffusivity for fastest translational heterogeneities (TH), normalized by the average over the entire system. We show all the simulated temperatures. (b) Temporal behavior of the ratio of the time-dependent rotational diffusivity and translational diffusivity for fastest rotational heterogeneities (RH), normalized by the average over the entire system. We show all the simulated temperatures. The figure shows that the decoupling of rotation from translation is increasingly more pronounced as T decreases and is a maximum (a) or minimum (b) on the time scale of the DH.

introduce the ratios

$$d_{\mathrm{TH}}(\Delta t) \equiv \frac{(D_r(\Delta t)/D_t(\Delta t))_{\mathrm{TH}}}{(D_r(\Delta t)/D_t(\Delta t))_{\mathrm{all}}}, \tag{3.18}$$

and similarly

$$d_{\mathrm{RH}}(\Delta t) \equiv \frac{(D_r(\Delta t)/D_t(\Delta t))_{\mathrm{RH}}}{(D_r(\Delta t)/D_t(\Delta t))_{\mathrm{all}}}. \tag{3.19}$$

Figure 3.7(a) shows the results for $d_{TH}(\Delta t)$ for the fastest subsets of molecules. For short times, $d_{TH}(\Delta t)$ does not depend on time and temperature, since in this initial temporal regime the dynamics at all temperatures is ballistic, i.e., both $\langle \varphi^2(\Delta t)\rangle$ and $\langle r^2(\Delta t)\rangle$ are approximately linear with $(\Delta t)^2$. At intermediate times $d_{TH}(\Delta t)$ develops a distinct maximum which increases in magnitude and shifts to larger observation times as T is reduced. The maximum occurs at the time scale where the fastest molecules of the TH and RH "break their cages" and enter the corresponding diffusive regimes, see Fig. 3.6(b). Therefore, the results of Fig. 3.7(a) also suggest that the decoupling between rotational and translational motion is largest at approximately the same time scale at which the DH are most pronounced. We note from Fig. 3.7(a) that $d_{TH}(\Delta t) < 1$, indicating that the decoupling of rotational and translational motion observed in the fastest subsets of TH is smaller than that from the average over the entire system. As we focus in slower subsets of TH for the same T, we observe that the maximum in $d_{TH}(\Delta t)$ decreases at any given T.

Figure 3.7(b) shows $d_{RH}(\Delta t)$ for the fastest subsets of molecules. Similar to the behavior of $d_{TH}(\Delta t)$, at short times $d_{RH}(\Delta t)$ does not depend on time nor temperature; molecules move ballistically in this regime. The maxima in $d_{RH}(\Delta t)$ at $\Delta t \approx 0.1$ ps for all temperatures are a consequence of the librational molecular motion, enhanced in this case because we are selecting the fastest subset of RH. At intermediate times, we observe a broad minimum in $d_{RH}(\Delta t)$ centered at $\Delta t \approx t^*$; this minimum becomes deeper and shifts to later times upon cooling, suggesting that the decoupling in the fastest subset of RH is largest at approximately the same time scale at which the DH are more pronounced. The fact that $d_{TH}(\Delta t)$ shows a maximum at approximately t^*, while $d_{RH}(\Delta t)$ shows a minimum at t^* is because fastest subsets of RH tend to enhance the rotational motion with respect to the translational motion, while the opposite situation occurs for the fastest subsets of TH.

We note from Fig. 3.7(b) that $d_{RH}(\Delta t) > 1$, indicating that the decoupling of rotational and translational motion observed in the fastest subsets of RH is larger than that found in the average over the entire system.

In short, the behavior of $d_{TH}(\Delta t)$ and $d_{RH}(\Delta t)$ indicates that the emergence of DH is correlated to the rotation/translation decoupling, just as it does for the breakdown of the SE and SED relations.

3.10 Summary

In this work, we tested in the SPC/E model for water (i) the validity of the SE and SED equations, (ii) the decoupling of rotational and translational motion, and (iii) the relation of (i) and (ii) to DH. We found that at low temperatures there is a breakdown of both the SE and SED relations and that these relations can be replaced by fractional functional forms. The SE breakdown is observed in every scale of translational mobility. Similarly, the SED breakdown is observed in every scale of rotational mobility. The view commonly accepted is that the origin of the breakdown of the SE and SED relations is to be attributed to the most mobile molecules embedded in an inactive background where these relations hold. Instead our results support the view of a "generalized breakdown".

We also found that, upon cooling, there is a decoupling of translational and rotational motion. This decoupling is also observed in all scales of rotational and translational mobilities. In agreement with MD simulations of an OTP model [137], we find that an opposite decoupling is observed depending on whether one uses the rotational diffusivity, D_r, or the rotational relaxation time, τ_2. In the first case, rotational motion is enhanced upon cooling with respect to the translational motion, while the opposite situation holds when choosing τ_2. This is particularly relevant for experiments, where typically only τ_2 is accessible.

We also found that as the decoupling of D_r/D_t increases, the number of molecules belonging simultaneously to both RH and TH also increases. This is counter-intuitive since a stronger decoupling would suggest less overlapping of TH and RH. Therefore we conclude that the decoupling of D_r/D_t is significant even at the single molecule level.

We also explored the role of time scales in the breakdown of the SE and SED relations and decoupling. To do this we introduced time dependent versions of the SE and SED expressions. Our results suggest that both the decoupling and SE and SED breakdowns are originated at the time scale corresponding to the end of the cage regime, when diffusion starts. This is also the time scale at which the DH are more relevant.

Our work also demonstrates that selecting DH on the basis of translational or rotational displacement more strongly biases the calculation of diffusion constants than the other dynamical properties. If appropriate care is taken, this should not be problematic, but it does make apparent that an alternative approach to identify DH would be valuable. This is especially true when contrasting behavior of diffusion constants and relaxation times, as is the case for the SE and SED relations.

3.11 Methods

3.11.1 Evaluation of the rotational mean square displacement

To calculate D_r [Eq. (3.7)] we consider the behavior of the normalized polarization vector $\hat{p}_i(t)$ for molecule i (defined as the normalized vector from the center of mass of the water molecule to the midpoint of the line joining the two hydrogens). The molecular rotation will cause a rotation of $\hat{p}_i(t)$. A naive definition of angular displacement as $\hat{p}_i(t)-\hat{p}_i(0)$ would be insensitive to full molecular rotations, since it would result in a bounded quantity. Following Ref. [123], we avoid this complication by defining the vector rotational displacement in the time interval $[t, t+\Delta t]$ as

$$\vec{\varphi}_i(\Delta t) \equiv \int_t^{t+\Delta t} \Delta\vec{\varphi}_i(t')dt', \tag{3.20}$$

where $\Delta\vec{\varphi}_i(t')$ is a vector with direction given by $\hat{p}_i(t') \times \hat{p}_i(t'+dt')$ and with magnitude given by $|\Delta\vec{\varphi}_i(t')| \equiv \cos^{-1}\left(\hat{p}_i(t') \cdot \hat{p}_i(t'+dt')\right)$, i.e., the angle spanned by $\hat{p}_i$ in the time interval $[t', t'+dt']$. Thus, the vector $\vec{\varphi}_i(\Delta t)$ allows us to define a trajectory in a 3D space representing the rotational motion of molecule i, analogous to the trajectory defined by $\vec{r}_i(\Delta t)$ for the translational case. We define, in analogy to MSD, a *rotational* mean square displacement (RMSD) [84, 123, 125]

$$\langle \varphi^2(\Delta t)\rangle \equiv \frac{1}{N}\sum_{i=0}^{N} |\vec{\varphi}_i(t+\Delta t) - \vec{\varphi}_i(t)|^2. \qquad (3.21)$$

Using this form, we define D_r as given by Eq. (3.7), analogous to the definition of D_t. We have verified that there is no qualitative difference, in the results of the present work, when the polarization vector is replaced by the other two principal directions of the water molecule.

3.11.2 Correlation functions for dynamical heterogeneities

We introduce a MSD, $\langle r^2(\Delta t)\rangle$, for the fastest and slowest subsets of molecules by limiting the sum in the Eq. (3.6) to the molecules in the corresponding subset. The different MSDs at $T = 210$ K are shown in Fig. 3.8(a). We note that since the most and least mobile 7% of the molecules will generally vary as a function of time, the molecules used to calculate $\langle r^2(\Delta t)\rangle$ will change with time; in other words, when a molecule ceases being part of a DH, it is no longer considered in the computation of the MSD and the focus is shifted to the new subset of molecules belonging to the DH considered. Analyzing the $\langle r^2(\Delta t)\rangle$ for the collection of subsets from most mobile to least mobile has the advantage that the mean of $\langle r^2(\Delta t)\rangle$ over the subsets converges to the MSD for the full system. In a similar fashion the RMSD, $\langle \varphi^2(\Delta t)\rangle$, is calculated also for the fastest and slowest rotationally mobile molecules [Fig. 3.8(b)].

To complement the single particle dynamics determined by $\langle r^2(\Delta t)\rangle$ and $\langle \varphi^2(\Delta t)\rangle$, we also evaluate the coherent intermediate scattering function

$$F(q,\Delta t) \equiv \frac{1}{N\,S(q)}\sum_{j=1}^{N} e^{-iqr_j(t+\Delta t)}\sum_{k=1}^{N} e^{iqr_k(t)}, \qquad (3.22)$$

where $S(q)$ is the structure factor. $F(q,\Delta t)$ reflects two-particle temporal correlations instead of single-particle correlations (as in the case of the MSD). The normalization factors ensure that $F(q,0) = 1$. In analogy to our analysis of $\langle r^2(\Delta t)\rangle$, we would like to evaluate the contribution to $F(q,\Delta t)$ made by subsets of molecules. Naively, one might think this

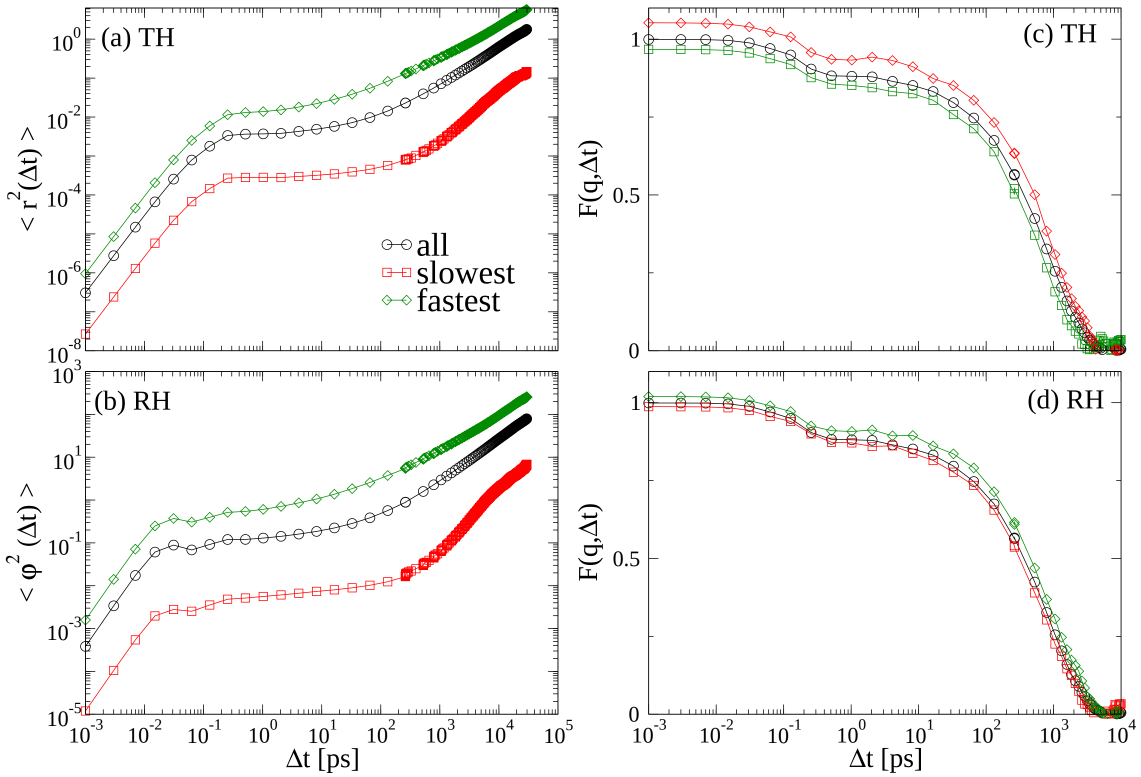

Figure 3.8: Example of time correlation functions limited to subsets of DH. (a) Mean square displacement (MSD) and (b) rotational mean square displacement (RMSD) at $T = 210$ K for the fastest and slowest translational heterogeneities (TH) and rotational heterogeneities (RH) respectively, as well as for the entire system. Intermediate scattering function, $F(q, \Delta t)$, at $T = 210$ K for (c) the fastest and slowest TH, and entire system and (d) the fastest and slowest RH and the entire system.

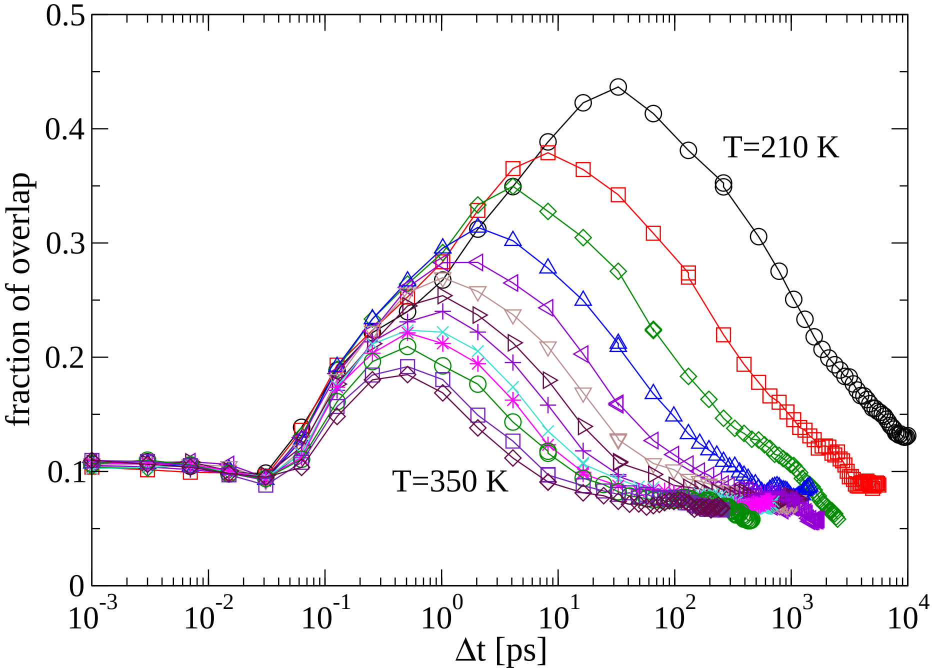

Figure 3.9: Fraction of molecules belonging simultaneously to *both* fastest translational heterogeneities (TH) and fastest rotational heterogeneities (RH) versus observation time Δt, at different temperatures. This overlap of fastest TH and fastest RH is maximum at the end of the cage regime and increases upon cooling. It is almost 45% at the lowest T.

can be simply done by limiting the sums in Eq. (3.22) to solely those molecules within the subset. However, taking the mean over the subsets of such a quantity will not recover the complete $F(q,\Delta t)$, since there will be no information on the cross-correlations between the subsets. In order to include these correlations and define a function that, when averaged over subsets, will return $F(q,\Delta t)$ (as is the case for MSD and RMSD), we simply limit one of the two sums to the subset, while the other sum still extends over all molecules. Mathematically, we define

$$F_{\rm subset}(q,\Delta t) \equiv \frac{1}{N_{\rm subset}\, S(q)} \sum_{j=1}^{N} e^{-iqr_j(t+\Delta t)} \sum_{k \in subset} e^{iqr_k(t)}. \tag{3.23}$$

Note that one must make the choice whether to limit the sum to the subset at time t or $t+\Delta t$; we have found that in practice there is little, if any, qualitative difference in this choice. Thus we measure the correlations between the subset of molecules at time t with all molecules at time $t+\Delta t$. Additionally, $F_{\rm subset}(q,0)$ is not necessarily 1; forcing this normalization would not satisfy the desired condition that the mean over subsets returns the average over all molecules. In all cases, we evaluate $F_{\rm subset}(q,\Delta t)$ at $q = 18$ nm^{-1}, the value of the transferred momentum at the first maximum of the structure factor where the relaxation is slowest (except for the $q \to 0$ limit). Figure 3.8(c) and 3.8(d) show $F(q,\Delta t)$ for all molecules, and for the fastest and the slowest TH and RH.

At this point, it is important to compare the behavior of $\langle r^2(\Delta t)\rangle$ and $\langle \varphi^2(\Delta t)\rangle$ with that of $F(q,\Delta t)$ for the TH and RH subsets. Since we define mobility on the basis of displacement, the behavior of $\langle r^2(\Delta t)\rangle$ and $\langle \varphi^2(\Delta t)\rangle$ for the subsets are much more strongly affected than $F_{\rm subset}(q,\Delta t)$ for the subsets. Additionally, $F_{\rm subset}(q,\Delta t)$ includes cross-correlations both within and between subsets that a single particle definition of mobility does not include. More specifically, the results in Fig. 3.8 at $T = 210$ K show that there is roughly two orders of magnitude difference between $\langle r^2(\Delta t)\rangle$ for the most and least mobile molecules (and similar difference for $\langle \varphi^2(\Delta t)\rangle$). We also find that there is roughly also two orders of magnitude difference between the most and least mobile molecules for D_t and D_r. For higher T, the difference is less pronounced. When we examine the relaxation of $F(q,\Delta t)$

for the most and least mobile subsets, we find only a difference of a factor of ≈ 2 between the time scales for relaxation. Therefore — not surprisingly — selecting mobility based on single particle displacement results in a much stronger effect on diffusion than it does for collective relaxation phenomena. This fact is important for the comparison between this work and a previous work [87].

3.11.3 Characteristic time of dynamical heterogeneities

Since we analyze the DH both in the context of translational and rotational motions, it is natural to ask at what time scale the TH and RH are more pronounced and to what degree the TH and RH subsets overlap each other. References [58] and [125] show that the fastest subsets of TH and RH form clusters, and that these clusters are larger at approximately the time t^* corresponding to the onset of the diffusive regime, as indicated by $\langle r^2(\Delta t)\rangle$ and $\langle \varphi^2(\Delta t)\rangle$ respectively. Normally t^* for the translational case is defined as the maximum in the non-Gaussian parameter [65]

$$\alpha_2(\Delta t) \equiv \frac{3 < r^4(\Delta t) >}{5 < r^2(\Delta t) >} - 1\,, \tag{3.24}$$

where $\langle r^4(\Delta t)\rangle$ and $\langle r^2(\Delta t)\rangle$ are the fourth and second moment of the displacement distribution, respectively (the last is also the MSD). $\alpha_2(\Delta t)$ is known to be identically zero for a Gaussian distribution, and thus it signals when the dynamics does not generate such a Gaussian distribution of displacements. In the present study, we use either translational, $\vec{r}_i(\Delta t)$, or rotational, $\vec{\varphi}_i(\Delta t)$, displacement for TH and RH, respectively, when computing $\alpha_2(\Delta t)$. Figure 3.6(b) shows t^* as a function of T defined for the fastest and slowest subsets of both the TH and RH. We also include the corresponding values of t^* for the entire system. Figure 3.6(b) shows that there is no qualitative difference in shape of the curve of $t^*(T)$ for the different subsets considered and the entire system.

Since the values of t^* for TH and RH are similar, we expect that there is some coupling between TH and RH. Previously, Chen *et al.* [138] found that at large momentum transfer q, there is coupling between translational and rotational motion. The maximum correlation occurs at the cage relaxation time, t^*, for large values of q. Ref. [125] found a spatial correlation between RH and TH. Along similar lines, we examine the overlap between these subsets. Figure 3.9 shows the overlap between the fastest subset of molecules belonging to TH and RH, as a function of Δt and T. Specifically, we count the number of fastest molecules belonging simultaneously to TH and RH as a function of observation time Δt. Similar to Fig. 9 in Ref. [138], the strength of this coupling reaches its maximum at the cage relaxation times, but these times are consistently shorter than those reported in [138]; this is likely to be due to the fact that we consider fastest TH and fastest RH in this calculation, while Ref. [138] considers all the molecules of the system. Figure 3.9 indicates that, at the lowest temperature simulated, about 45% of the molecules comprising the fastest subset of TH coincide with the ones in the fastest subset of RH.

Chapter 4

Water and the glass transition of biomolecules

Both experiments and computer simulation studies have shown that hydrated proteins undergo a "glass–like" transition near 200 K [139–143], above which proteins exhibit diffusive motion, and below which the proteins are trapped in harmonic modes. An important issue is to determine the effects of hydration water on this dynamical transition [144–148]. Experiments and computer simulations suggested that when a protein is solvated, the protein glass transition is strongly coupled to the solvent, leading to the question of whether the protein glass transition is directly related to a dynamic transition in the surrounding solvent [149].

Here we explore the hypothesis that the observed glass transition in biomolecules is related to the liquid-liquid phase transition [14, 150] and test this hypothesis by computer simulations. Specifically, using molecular dynamics (MD) simulations, we study the dynamic and thermodynamic behavior of lysozyme and DNA in hydration TIP5P [151–153] water, by means of the software package GROMACS [154] for (i) an orthorhombic form of hen egg-white lysozyme [155] and (ii) a Dickerson dodecamer DNA [156] at constant pressure $P = 1$ atm, several constant temperatures T, and constant number of water molecules N (NPT ensemble) in a simulation box with periodic boundary conditions. We first allow the system to equilibrate at constant temperature and pressure using the Berendsen method. This initial equilibration is followed by a long production run during which we calculate the dynamic and static properties. Equilibration times vary for different temperatures from a few ns for high temperatures to as much as 40 ns for low temperatures. The MD for DNA was performed using the Amber force field [157]. For lysozyme simulations, the system consists of a single protein in the native conformation solvated in $N = 1242$ TIP5P water molecules [151–153]. These simulation conditions correspond to a ratio of water mass to protein mass of 1.56). The DNA system consists of a single DNA helix with 24 nucleotides solvated in $N = 1488$ TIP5P water molecules, which corresponds to an experimental hydration level of 3.68.

The simulation results for protein and protein hydration water are shown in Fig. 4.1(a). We calculate the root mean square (RMS) fluctuations $\left\langle x^2 \right\rangle^{1/2}$ of protein from the equilibrated configurations, first for each atom over 1 ns, and then averaged over the total number of atoms in the protein. We find that the protein fluctuations [Fig. 4.1(a)] change functional form below $T_{\rm p} \approx 254 \pm 5$ K. At low temperatures the residues perform harmonic vibrational motion near the local potential energy minima thus one expects that tha evarage square fluctuations grow lineary with temperature. Moreover, upon cooling, the diffusivity of hydration water exhibits a dynamic crossover from non–Arrhenius[1] to Arrhenius behavior at the same crossover temperature $T_\times \approx 254 \pm 5$ K [Fig. 4.2(a)]. The actual dynamic transition temperature across the Widom line (254 K) is higher than $T_{MCT} \approx 230$ K. A similar temperature dependence of diffusivity of bulk TIP5P water was observed [159]. The coincidence of $T_\times$ with $T_{\rm p}$ indicates that the protein is strongly coupled with the surrounding solvent, in agreement with recent experiments [160]. Note that $T_\times$ is much higher than the glass transition temperature estimated for TIP5P as $T_g = 215$K [153]. Thus this crossover is not likely to be related to the glass transition in water. Here we will explore the possibility that instead it is related to a change in the properties of protein hydration water.

Experimental studies of supercritical water [161] indeed show that various response

---

[1] As a comparison, we used a prediction of the "mode coupling theory" (MCT) [158] to fit the data with parameters $T_{MCT} \approx 227$ and $\gamma \approx 2.72$.

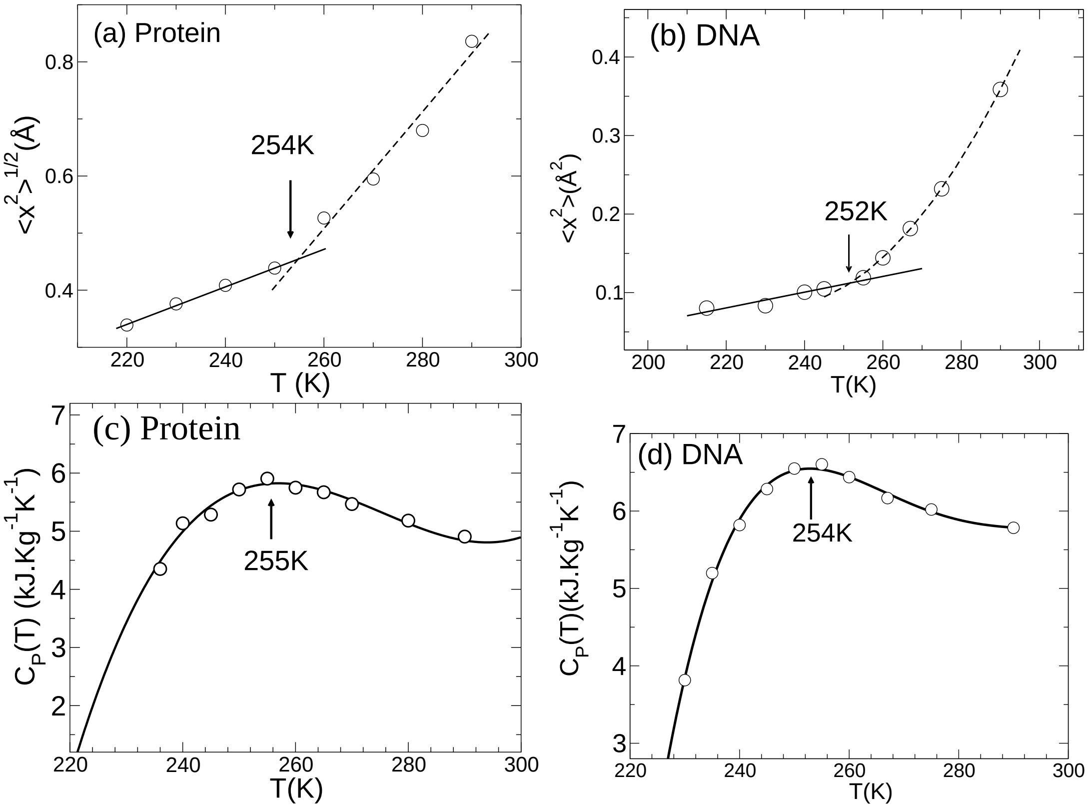

Figure 4.1: RMS fluctuation of (a) lysozyme, and (b) DNA showing that there is a transition around $T_\mathrm{p} \approx 254 \pm 5$ K. The simulations for DNA for $T < 220$ K are not equilibrated, but we did not observe any significant change in the RMS fluctuations within the equilibration time. (c) The specific heat of the combined system, lysozyme and water, and (d) DNA display maxima at $T_\mathrm{W} \approx 255$ K.

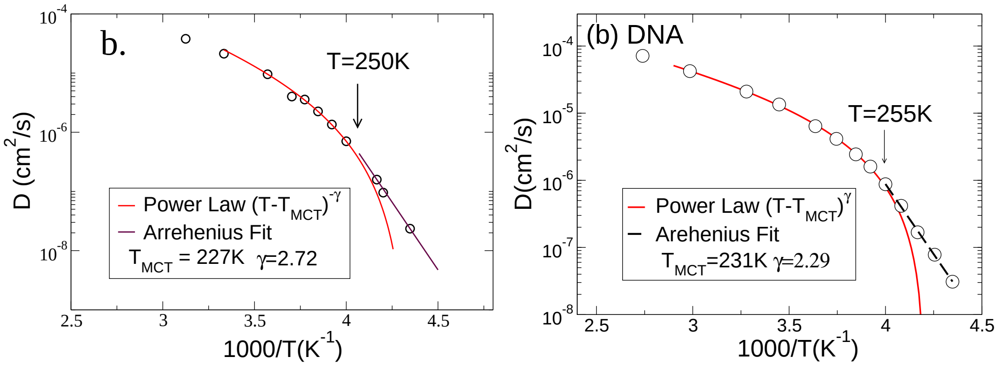

Figure 4.2: Diffusion constant of hydration water surrounding (a) lysozyme, and (b) DNA shows a dynamic transition from a power law behavior to an Arrhenius behavior at $T_\times \approx 250 \pm 5$ K.

functions have sharp maxima in the analogous region of the phase diagram above the liquid-vapor critical point C_1, but no direct experimental indication of a liquid-liquid critical point C_2 had been available due to unavoidable crystallization of bulk water[2]. Previously it was found that water remains unfrozen in hydrophilic nanopores for $T > 200$ K [163, 164]. Moreover when cooled at constant pressure for $P < P_{C2}$ the dynamics changes from non–Arrhenius to Arrhenius at $T = T_\times(P)$. The line $T_\times(P)$ is located in the range of temperatures between $200 - 230$ K and has a negative slope in the P-T phase diagram.

Upon crossing the first order phase transition line above the critical pressure, the thermodynamic state functions change discontinuously. Below the critical pressure they rapidly but continuously change upon cooling, see path α in Fig.1(c) of [159]. Indeed computer simulations of TIP5P[151, 153] and ST2 [150, 159, 162] water models show that many response functions such as isobaric specific heat and isothermal compressibility have sharp maxima as functions of temperature if the system is cooled isobarically at $P < P_{C2}$. The loci of these maxima asymptotically approach one another as the critical point is approached, because all of them become expressible in terms of the correlation length which is diverging at the critical point. This asymptotic line is called the Widom line. Computer simulations

---

[2] The situation is rather complex. Many different scenarios have been proposed in the literature, including a scenario with multiple liquid-liquid critical points [153, 162].

suggest that this line may be associated with $T_W(P)$, the Widom line, near which the local dynamic characteristics must rapidly change from those resembling the properties of HDL at high temperature to those of LDL at low temperature [159].

We also study the static properties — thermodynamics and structural properties. We first calculate the constant pressure specific heat C_P by numerical differentiation of the total enthalpy of the system (protein and water) as a function of temperature. This is done by fitting the enthalpy data by a fourth order polynomial and then by taking the derivative with respect to temperature. Figure 4.1(c) displays a maximum of $C_P(T)$ at $T_{\mathrm{W}} \approx 255 \pm 5$ K. The fact that $T_{\mathrm{p}} \approx T_{\times} \approx T_{\mathrm{W}}$ is evidence of the strong correlation of the changes in protein fluctuations [Fig. 4.1 (a)] with the hydration water thermodynamics [Fig. 4.1 (c)]. Thus our results are consistent with the possibility that the protein glass transition is related to the Widom line (and hence to the hypothesized liquid-liquid critical point). Crossing the Widom line corresponds to a continuous but rapid transition of the structural and thermodynamical properties of water from those resembling the properties of a local HDL structure for $T > T_{\mathrm{W}}(P)$ to those resembling the properties of a local LDL structure for $T < T_{\mathrm{W}}(P)$ [159, 164]. A consequence is the expectation that the fluctuations of the protein residues in low density water (more ordered and more rigid) just below the Widom line should be smaller than the fluctuations in high density water (less ordered and less rigid) just above the Widom line.

To test this interpretation, we analyze the structure of hydration water on the two sides of the Widom line. Fig. 4.3(a) shows the oxygen-oxygen radial distribution function $g(r)$ on two sides of the Widom line for lysozyme hydration water. The first peak of $g(r)$ on the low temperature (T=230 K) side is sharper and the first minimum is shallower compared to the $g(r)$ on the high temperature (T=270 K, 300 K) side of the Widom line, suggesting that water is more structured on the low temperature side. Further, we calculate the structure factor $S(q)$ of lysozyme hydration water [Fig. 4.3(c)]. The first peak of the structure factor associated with the hydrogen bond is very sharp and pronounced, for $T < T_{\mathrm{W}}(P)$, it is diminished and moves to larger wave vectors for $T > T_{\mathrm{W}}(P)$, consistent with a LDL-like

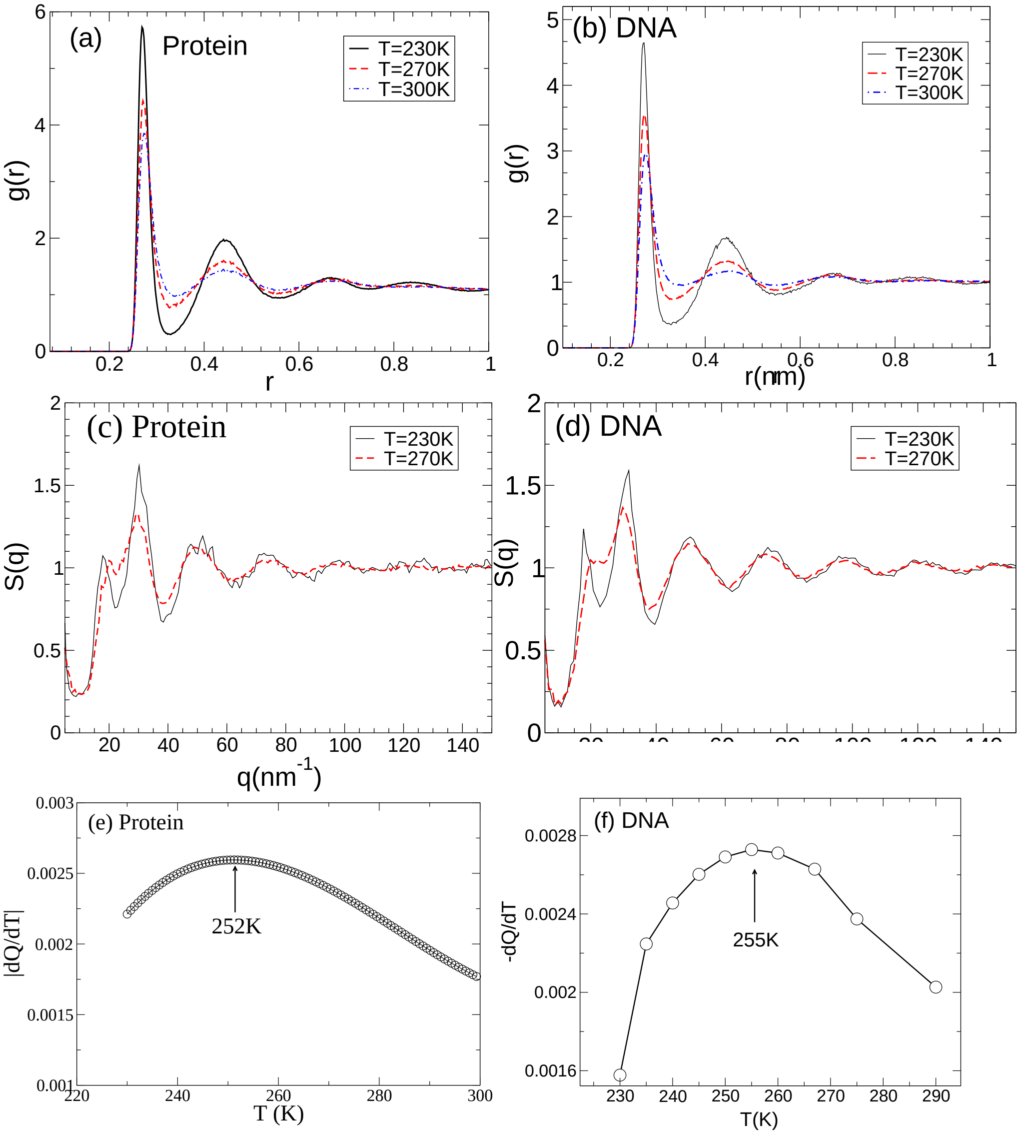

Figure 4.3: Oxygen–Oxygen pair correlation function $g(r)$ for (a) lysozyme hydration water, and (b) DNA hydration water, on crossing the Widom line from the HDL side ($T = 270$ K, 300 K) to the LDL side ($T = 230$ K). Structure factor of hydration water surrounding (c) lysozyme, and (d) DNA on two sides of the the Widom line. Upon crossing the Widom line, the local structure of water changes from more HDL-like to more LDL-like, reflected in the sharper and more prominent first peak. The first peak associated with the hydrogen bond distance also moves to small wave vectors, suggesting a change from the HDL to the LDL-like local structure of water at low temperatures. Derivative with respect to temperature of the orientational order parameter Q for (e) lysozyme and (f) DNA.

local structure for $T < T_{\mathrm{W}}(P)$ and a HDL-like local structure for $T > T_{\mathrm{W}}(P)$. Indeed we see the orientational order parameter, defined in [165], of water molecules increase upon cooling and the rate of increase is maximum at the Widom line temperature [Fig 4.3(e)-(f) shows the rate of change of Q with temperature].

Previous simulations [148] and experiments [147] suggest a "glass–like" transition of DNA around temperature 230 K. Hence to test if the dynamic crossover depends on the solute, we performed a parallel study of the DNA Dickerson dodecamer [156]. We find that fluctuations[3] of the DNA molecule [Fig. 4.1(b)] change their behavior approximately at the same temperature as lysozyme, with $T \approx 254 \pm 5$ K. The dynamic crossover in the hydration water upon cooling from non–Arrhenius to Arrhenius behavior takes place at $T_{\times} \approx 255 \pm 5$ K [Fig. 4.2(b)]. The specific heat maximum is located at $T_W \approx 255 \pm 5$ K [Fig. 4.1(d)]. For DNA hydration water C_P has a maximum at $T \approx 254$ K, similarly to the protein case of Fig. 4.1(c)[4]. Fig. 4.3(b) and Fig. 4.3(d) show $g(r)$ and $S(q)$ for the DNA hydration water[5]. The quantitative agreement of these results with the corresponding results for lysozyme suggests that it is indeed the changes in the properties of hydration water that are responsible for the changes in dynamics of the protein and DNA biomolecules. Our results are in qualitative agreement with recent experiments on hydrated protein and DNA [166] which found the crossover in side-chain fluctuations at $T_{\mathrm{p}} \approx 225$ K .

---

[3] The RMS fluctuation for DNA was calculated in the same fashion as for lysozyme.

[4] The values of C_P are different in each case with $C_P^{\mathrm{bulk}}(T_W) > C_P^{\mathrm{DNA}}(T_W) > C_P^{\mathrm{protein}}(T_W)$, probably because DNA hydration level (368%) is larger than lysozyme hydration level (156%) and the fact that the specific heat of water is larger than protein and DNA.

[5] The difference in the height of the first peak of $g(r)$ for lysozyme and DNA hydration water is due to the different hydration levels of the two systems.

Chapter 5

Cell model for water

Water is possibly the most important liquid for life [167] and, at the same time, is a very peculiar liquid [3]. In the stable liquid regime its thermodynamic response functions behave qualitatively differently than a typical liquid. The isothermal compressibility K_T, for example, has a minimum as a function of temperature at $T = 46$ °C, while for a typical liquid K_T monotonically decreases upon cooling. Water's anomalies become even more pronounced as the system is cooled below the melting point and enters the metastable supercooled regime [168].

Different hypothesis have been proposed to rationalize the anomalies of water [169]. All these interpretations, but one, predict the existence of a liquid–liquid phase transition in the supercooled state, consistent with the experiments to date [169] and supported by different models [3].

To discriminate among the different interpretations, many experiments have been performed [99]. However, the freezing in the temperature-range of interest can be avoided only for water in confined geometries or on the surface of macromolecules [169, 170]. Since experiments in the supercooled region are difficult to perform, numerical simulations have played an important role in recent years to help interpret the data. However, also the simulations at very low temperature T are hampered by the glassy dynamics of the empirical models of water [171, 172]. For these reasons is important to implement more efficient numerical simulations for simple models, able to capture the fundamental physics of water but also less computationally expensive. Here we introduce the implementation of a Wolff cluster algorithm [173] for the Monte Carlo (MC) simulations of a cell model for water [174, 175]. The model is able to reproduce all the different scenarios proposed to interpret the behavior of water [176] and has been analyzed (i) with mean field (MF) [174, 175, 177, 178], (ii) with Metropolis MC simulations [172, 179] and (iii) with Wang-Landau MC density of state algorithm [180]. Recent Metropolis MC simulations [172] have shown that very large times are needed to equilibrate the system as $T \to 0$, as a consequence of the onset of the glassy dynamics. The implementation of Wolff clusters MC dynamics, presented here, allows us to (i) drastically reduce the equilibration times of the model at very low T and (ii) give a geometrical characterization of the regions of correlated water molecules (clusters) at low T and show that the liquid–liquid phase transition can be interpreted as a percolation transition of the tetrahedrally ordered clusters.

5.1 The model

The system consists of N particles distributed within a volume V in d dimensions. The volume is divided into N cells of volume v_i with $i \in [1, N]$. For sake of simplicity, these cells are chosen of the same size, $v_i = V/N$, but the generalization to the case in which the volume can change without changes in the topology of the nearest–neighbor (n.n.) is straightforward. By definition, $v_i \geq v_0$, where v_0 is the molecule hard-core volume. Each cell has a variable $n_i = 0$ for a gas-like or $n_i = 1$ for a liquid-like cell. We partition the total volume in a way such that each cell has at least four n.n. cells, e.g. as in a cubic lattice in $3d$ or a square lattice in $2d$. Periodic boundary conditions are used to limit finite–size effects.

The system is described by the Hamiltonian [174, 175]

$$\mathscr{H} = -\epsilon \sum_{\langle i,j \rangle} n_i n_j - J \sum_{\langle i,j \rangle} n_i n_j \delta_{\sigma_{ij},\sigma_{ji}} - J_\sigma \sum_i n_i \sum_{(k,l)_i} \delta_{\sigma_{ik},\sigma_{il}}, \tag{5.1}$$

where $\epsilon > 0$ is the strength of the van der Waals attraction, $J > 0$ accounts for the hydrogen bond energy, with four (Potts) variables $\sigma_{ij} = 1, \ldots, q$ representing bond indices of molecule

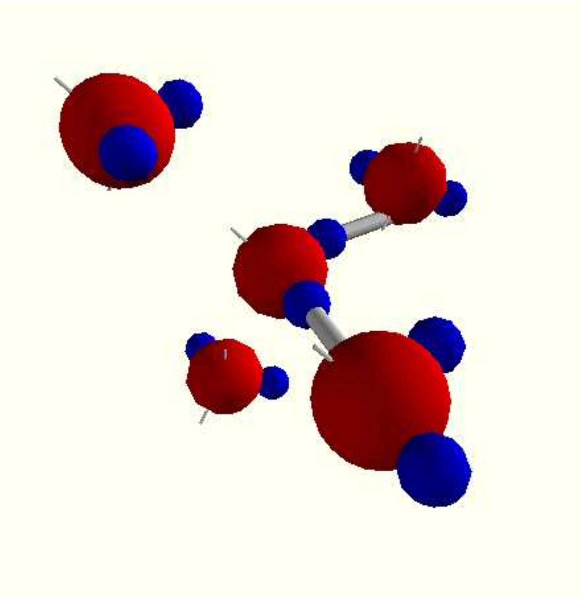

Figure 5.1: A pictorial representation of five water molecules in $3d$. Two hydrogen bonds (grey links) connect the hydrogens (in blue) of the central molecule with the lone electrons (small gray lines) of two nearest neighbor (n.n.) molecules. A bond index (arm) with $q = 6$ possible values is associated to each hydrogen and lone electron, giving rise to q^4 possible orientational states for each molecule. A hydrogen bond can be formed only if the two facing arms of the n.n. molecules are in the same state. Arms on the same molecule interact among themselves to mimic the O-O-O interaction that drives the molecules toward a tetrahedral local structure.

i with respect to the four n.n. molecules j, $\delta_{a,b} = 1$ if $a = b$ and $\delta_{a,b} = 0$ otherwise, and $\langle i, j \rangle$ denotes that i and j are n.n. The model does not assume a privileged state for bond formation. Any time two facing bond indices (arms) are in the same (Potts) state, a bond is formed. The third term represents an intramolecular (IM) interaction accounting for the O–O–O correlation [181], locally driving the molecules toward a tetrahedral configuration. When the bond indices of a molecule are in the same state, the energy is decreased by an amount $J_\sigma \geqslant 0$ and we associate this local ordered configuration to a local tetrahedral arrangement. The notation $(k, l)_i$ indicates one of the six different pairs of the four bond indices of molecule i (Fig.5.1). The model does not differentiate "donor" molecule and "acceptor" molecule in the hydrogen bond definition. This simplification increases the number of possible bonded configurations, hence increases the entropy associated to the local tetrahedral configurations. A simple modification of the model could explicitly take into account this feature, however the comparison of the results from the present version of the model with experiments and simulations from more detailed models shows good qualitative agreement.

Experiments show that the formation of a hydrogen bond leads to a local volume expansion [3]. Thus in our system the total volume is

$$V = Nv_0 + N_{HB} v_{HB}, \tag{5.2}$$

where

$$N_{HB} \equiv \sum_{<i,j>} n_i n_j \delta_{\sigma_{ij},\sigma_{ji}} \tag{5.3}$$

is the total number of hydrogen bonds, and v_{HB} is the constant specific volume increase due to the hydrogen bond formation.

5.2 Mean–field analysis

In the mean–field (MF) analysis the macrostate of the system in equilibrium at constant pressure P and temperature T (NPT ensemble) may be determined by a minimization of the Gibbs free energy per molecule, $g \equiv (\langle \mathscr{H} \rangle + PV - TS)/N_w$, where

$$N_w = \sum_i n_i \tag{5.4}$$

is the total number of liquid-like cells, and $S = S_n + S_\sigma$ is the sum of the entropy S_n over the variables n_i and the entropy S_σ over the variables σ_{ij}.

A MF approach consists of writing g explicitly using the approximations

$$\sum_{<i,j>} n_i n_j \longrightarrow 2Nn^2 \tag{5.5}$$

$$\sum_{<i,j>} n_i n_j \delta_{\sigma_{ij},\sigma_{ji}} \longrightarrow 2Nn^2 p_\sigma \tag{5.6}$$

$$\sum_i n_i \sum_{(k,l)_i} \delta_{\sigma_{ik},\sigma_{il}} \longrightarrow 6Nnp_\sigma \tag{5.7}$$

where $n = N_w/N$ is the average of n_i, and p_σ is the probability that two adjacent bond indices σ_{ij} are in the appropriate state to form a hydrogen bond.

Therefore, in this approximation we can write

$$V = Nv_0 + 2Nn^2 p_\sigma v_{HB}, \tag{5.8}$$

$$\langle \mathscr{H} \rangle = -2\left[\epsilon n + (Jn + 3J_\sigma) p_\sigma\right] nN. \tag{5.9}$$

The probability p_σ, properly defined as the thermodynamic average over the whole system, is approximated as the average over two neighboring molecules, under the effect of the mean-field h of the surrounding molecules

$$p_\sigma = \left\langle \delta_{\sigma_{ij},\sigma_{ji}} \right\rangle_h . \tag{5.10}$$

The ground state of the system consists of all N variables $n_i = 1$, and all σ_{ij} in the same state. At low temperatures, the symmetry will remain broken, with the majority of the σ_{ij} in the preferred state. We associate this preferred state to the tetrahedral order of the molecules and define m_σ as the density of the bond indices in the tetrahedral state, with $0 \leq m_\sigma \leq 1$. Therefore, the number density n_σ of bond indices σ_{ij} is in the tetrahedral state is

$$n_\sigma = \frac{1 + (q-1)m_\sigma}{q}. \tag{5.11}$$

Since an appropriate form for h is [174, 175]

$$h = 3J_\sigma n_\sigma, \tag{5.12}$$

we obtain that $\frac{3J_\sigma}{q} \leq h \leq 3J_\sigma$.

The MF expressions for the entropies S_n of the N variables n_i, and S_σ of the $4Nn$ variables σ_{ij}, are then [177]

$$S_n = -k_B N(n \log(n) + (1-n)\log(1-n)) \tag{5.13}$$

$$S_\sigma = -k_B 4Nn[n_\sigma \log(n_\sigma) + \\ (1-n_\sigma)\log(1-n_\sigma) + \log(q-1)], \tag{5.14}$$

where k_B is the Boltzmann constant.

Equating

$$p_\sigma \equiv n_\sigma^2 + \frac{(1-n_\sigma)^2}{q-1}, \tag{5.15}$$

with the approximate expression in Eq. (5.10), allows for solution of n_σ, and hence g, in terms of the order parameter m_σ and n.

By minimizing numerically the MF expression of g with respect to n and m_σ, we find the equilibrium values $n^{(eq)}$ and $m_\sigma^{(eq)}$ and, with Eqs. (5.4) and (5.2), we calculate the density ρ at any (T, P) and the full equation of state. An example of minimization of g is presented in Fig. 5.2 where, for the model's parameters $J/\epsilon = 0.5$, $J_\sigma/\epsilon = 0.05$, $v_{HB}/v_0 = 0.5$, $q = 6$, a discontinuity in $m_\sigma^{(eq)}$ is observed for $Pv_0/\epsilon > 0.8$. As discussed in Ref.s [174, 175, 179] this discontinuity corresponds to a first order phase transition between two liquid phases with different degree of tetrahedral order and, as a consequence, different density. The higher P at which the change in $m_\sigma^{(eq)}$ is continuous, corresponds to the pressure of a liquid–liquid critical point (LLCP). The occurrence of the LLCP is consistent with one of the possible interpretations of the anomalies of water, as discussed in Ref. [177]. However, for different choices of parameters, the model reproduces also the other proposed scenarios [176].

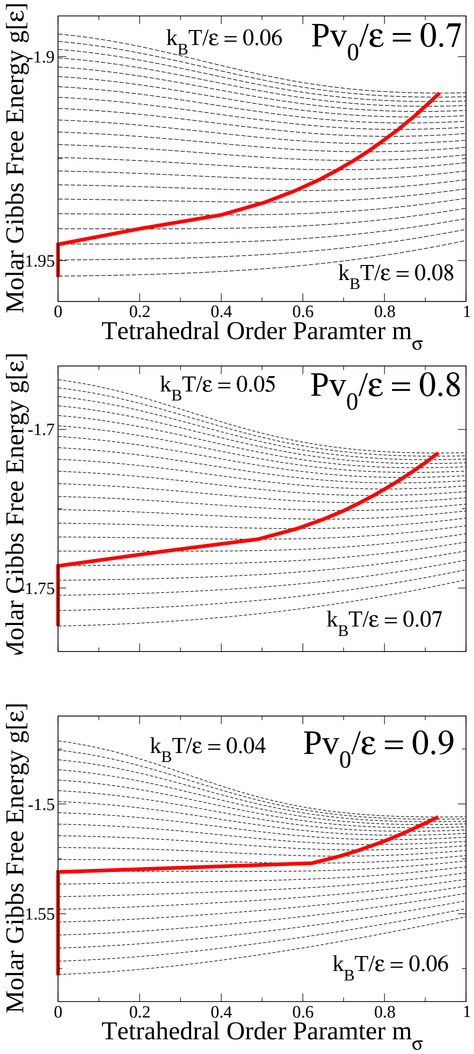

Figure 5.2: Numerical minimization of the molar Gibbs free energy g in the MF approach. The model's parameters are $J/\epsilon = 0.5$, $J_\sigma/\epsilon = 0.05$, $v_{HB}/v_0 = 0.5$ and $q = 6$. In each panel we present g (dashed lines) calculated at constant P and different values of T. The thick line crossing the dashed lines connects the minima $m_\sigma^{(eq)}$ of g at different T. Upper panel: $Pv_0/\epsilon = 0.7$, for T going from $k_BT/\epsilon = 0.06$ (top) to 0.08 (bottom). Middle panel: $Pv_0/\epsilon = 0.8$, for T going from $k_BT/\epsilon = 0.05$ (top) to 0.07 (bottom). Lower panel: $Pv_0/\epsilon = 0.9$, for T going from $k_BT/\epsilon = 0.04$ (top) to 0.06 (bottom). In each panel dashed lines are separated by $k_B\delta T/\epsilon = 0.001$. In all the panels $m_\sigma^{(eq)}$ increases when T decreases, being 0 (marking the absence of tetrahedral order) at the higher temperatures and $\simeq 0.9$ (high tetrahedral order) at the lowest temperature. By changing T, $m_\sigma^{(eq)}$ changes in a continuous way for $Pv_0/\epsilon = 0.7$ and 0.8, but discontinuous for $Pv_0/\epsilon = 0.9$ and higher P.

5.3 The simulation with the Wolff clusters Monte Carlo algorithm

To perform MC simulations in the NPT ensemble, we consider a modified version of the model in which we allow for continuous volume fluctuations. To this goal, (i) we assume that the system is homogeneous with all the variables n_i set to 1 and all the cells with volume $v = V/N$; (ii) we consider that $V \equiv V_{MC} + N_{HB}v_{HB}$, where $V_{MC} \geqslant Nv_0$ is a dynamical variable allowed to fluctuate in the simulations; (iii) we replace the first (van der Waals) term of the Hamiltonian in Eq. (5.1) with a Lennard-Jones potential with attractive energy $\epsilon > J$ and truncated at the hard-core distance

$$U_W(r) \equiv \begin{cases} \infty & \text{if } r \leqslant r_0, \\ \epsilon\left[\left(\frac{r_0}{r}\right)^{12} - \left(\frac{r_0}{r}\right)^{6}\right] & \text{if } r > r_0. \end{cases} \tag{5.16}$$

where $r_0 \equiv (v_0)^{1/d}$; the distance between two n.n. molecules is $(V/N)^{1/d}$, and the distance r between two generic molecules is the Cartesian distance between the center of the cells in which they are included.

The simplification (i) could be removed, by allowing the cells to assume different volumes v_i and keeping fixed the number of possible n.n. cells. However, the results of the model under the simplification (i) compares well with experiments [177]. Furthermore, the simplification (i) allows to drastically reduce the computational cost of the evaluation of the $U_W(r)$ term from $N(N-1)$ to $N-1$ operations. The changes (i)–(iii) modify the model used for the mean field analysis and allow off-lattice MC simulations for a cell model in which the topology of the molecules (i.e. the number of n.n.) is preserved. The comparison of the mean field results with the MC simulations show that these changes do not modify the physics of the system.

We perform MC simulations with $N = 2500$ and $N = 10000$ molecules, each with four n.n. molecules, at constant P and T, in 2d, and with the same parameters used for the mean field analysis. To each molecules we associate a cell on a square lattice. The Wolff algorithm is based on the definition of a cluster of variables chosen in such a way to be thermodynamically correlated [182, 183]. To define the Wolff cluster, a bond index (arm) of a molecule is randomly selected; this is the initial element of a stack. The cluster is grown by first checking the remaining arms of the same initial molecule: if they are in the same Potts state, then they are added to the stack with probability $p_{\text{same}} \equiv 1 - \exp(-\beta J_\sigma)$ [173], where $\beta \equiv (k_B T)^{-1}$. This choice for the probability p_{same} depends on the interaction J_σ between two arms on the same molecule and guarantees that the connected arms are thermodynamically correlated [183]. Next, the arm of a new molecule, facing the initially chosen arm, is considered. To guarantee that connected facing arms correspond to thermodynamically correlated variables, is necessary [182] to link them with the probability $p_{\text{facing}} \equiv 1 - \exp(-\beta J')$ where $J' \equiv J - Pv_{HB}$ is the P–dependent effective coupling between two facing arms as results from the enthalpy $\mathscr{H} + PV$ of the system. It is important to note that J' can be positive or negative depending on P. If $J' > 0$ and the two facing arms are in the same state, then the new arm is added to the stack with probability p_{facing}; if $J' < 0$ and the two facing arms are in different states, then the new arm is added with probability p_{facing} [1]. Only after every possible direction of growth for the cluster has been considered the values of the arms are changed in a stochastic way; again we need to consider two cases: (i) if $J' > 0$, all arms are set to the same new value

$$\sigma^{\text{new}} = \left(\sigma^{\text{old}} + \phi\right) \mod q \tag{5.17}$$

where ϕ is a random integer between 1 and q; (ii) if $J' < 0$, the state of every single arm is changed (rotated) by the same random constant $\phi \in [1, \dots q]$

$$\sigma_i^{\text{new}} = \left(\sigma_i^{\text{old}} + \phi\right) \mod q. \tag{5.18}$$

In order to implement a constant P ensemble we let the volume fluctuate. A small increment $\Delta r / r_0 = 0.01$ is chosen with uniform random probability and added to the current radius of a cell. The change in volume $\Delta V \equiv V^{\text{new}} - V^{\text{old}}$ and van der Waals energy

---

[1] The results of [182, 183] guarantee that the cluster algorithm described here satisfies the detailed balance and is ergodic. Therefore, it is a valid Monte Carlo dynamics.

ΔE_W is computed and the move is accepted with probability

$$p_{vol} = \min\left(1, \exp\left[-\beta\left(\Delta E_W + P\Delta V - T\Delta S\right)\right]\right), \tag{5.19}$$

where $\Delta S \equiv -Nk_B \ln(V^{new}/V^{old})$ is the entropic contribution.

5.4 Monte Carlo correlation times

The cluster MC algorithm described in the previous section turns out to be very efficient at low T, allowing to study the thermodynamics of deeply supercooled water with quite intriguing results [184]. To estimate the efficiency of the cluster MC dynamics with respect to the standard Metropolis MC dynamics, we evaluate in both dynamics, and compare, the autocorrelation function of the average magnetization per site $M_i \equiv \frac{1}{4}\sum_j \sigma_{ij}$, where the sum is over the four bonding arms of molecule i.

$$C_M(t) \equiv \frac{1}{N}\sum_i \frac{\langle M_i(t_0+t)M_i(t_0)\rangle - \langle M_i\rangle^2}{\langle M_i^2\rangle - \langle M_i\rangle^2}. \tag{5.20}$$

For sake of simplicity, we define the MC dynamics autocorrelation time τ as the time, measured in MC steps, when $C_M(\tau) = 1/e$. Here we define a MC step as $4N$ updates of the bond indices followed by a volume update, i.e. as $4N+1$ steps of the algorithm.

In Fig. 5.3 we show a comparison of $C_M(t)$ for the Metropolis and Wolff algorithm implementations of this model for a system with $N = 50 \times 50$, at three temperatures along an isobar below the LLCP, and approaching the line of the maximum, but finite, correlation length, also known as Widom line $T_W(P)$ [177]. In the top panel, at $T \gg T_W(P)$ ($k_BT/\epsilon = 0.11$, $Pv_0/\epsilon = 0.6$), we find a correlation time for the Wolff cluster MC dynamics $\tau_{\mathrm{W}} \approx 3\times 10^3$, and for the Metropolis dynamics $\tau_{\mathrm{M}} \approx 10^6$. In the middle panel, at $T > T_W(P)$ ($k_BT/\epsilon = 0.09$, $Pv_0/\epsilon = 0.6$) the difference between the two correlation times is larger: $\tau_{\mathrm{W}} \approx 2.5 \times 10^3$, $\tau_{\mathrm{M}} \approx 3 \times 10^6$. The bottom panel, at $T \simeq T_W(P)$ ($k_BT/\epsilon = 0.06$, $Pv_0/\epsilon = 0.6$) shows $\tau_{\mathrm{W}} \approx 3.7 \times 10^2$, while τ_{M} is beyond the accessible time window ($\tau_{\mathrm{M}} > 10^7$).

Since as $T \to 0$ the system enters a glassy state [172], the efficiency $\tau_{\mathrm{M}}/\tau_{\mathrm{W}}$ grows at lower T allowing the evaluation of thermodynamics averages even at $T \ll T_C$ [184]. In particular,

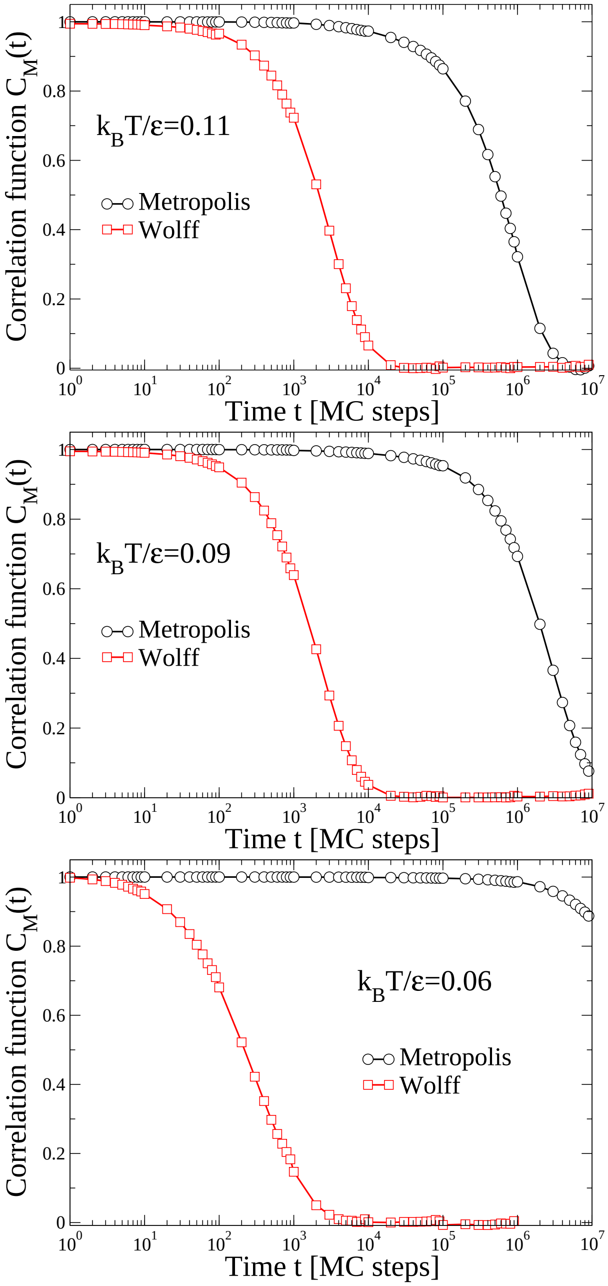

Figure 5.3: Comparison of the autocorrelation function $C_M(t)$ for the Metropolis (circles) and Wolff (squares) implementation of the present model. We show the temperatures $k_BT/\epsilon = 0.11$ (top panel), $k_BT/\epsilon = 0.09$ (middle panel), $k_BT/\epsilon = 0.06$ (bottom panel), along the isobar $Pv_0/\epsilon = 0.6$ close to the LLCP for $N = 50 \times 50$.

the cluster MC algorithm turns out to be very efficient when approaching the Widom line in the vicinity of the LLCP, with an efficiency of the order of 10^4. We plan to analyze in a systematic way how the efficiency $\tau_{\mathrm{M}}/\tau_{\mathrm{W}}$ grows on approaching the LLCP. This result is well known for the standard liquid-gas critical point [173] and, on the basis of our results, could be extended also to the LLCP. However, this analysis is very expensive in terms of CPU time and goes beyond the goal of the present work. Nevertheless, the percolation analysis, presented in the next section, helps in understanding the physical reason for this large efficiency.

The efficiency is a consequence of the fact that the average size of Wolff clusters changes with T and P in the same way as the average size of the regions of correlated molecules [183], i.e. a Wolff cluster statistically represents a region of correlated molecules. Moreover, the mean cluster size diverges at the critical point with the same exponent of the Potts magnetic susceptibility [183], and the clusters percolate at the critical point, as we will discuss in the next section.

5.5 Percolating clusters of correlated molecules

The efficiency of Wolff cluster algorithm is a consequence of the exact relation between the average size of the finite clusters and the average size of the regions of thermodynamically correlated molecules. The proof of this relation at any T derives straightforward from the proof for the case of Potts variables [183]. This relation allows to identify the clusters built during the MC dynamics with the correlated regions and emphasizes (i) the appearance of heterogeneities in the structural correlations [125, 185, 186], and (ii) the onset of percolation of the clusters of tetrahedrally ordered molecules at the LLCP [187], as shown in Fig. 5.4.

A systematic percolation analysis [182] is beyond the goal of this report, however configurations such as those in Fig. 5.4 allow the following qualitative considerations. At $T > T_C$ the average cluster size is much smaller than the system size. Hence, the structural correlations among the molecules extends only to short distances. This suggests that the correlation time of a local dynamics, such as Metropolis MC or molecular dynamics, would

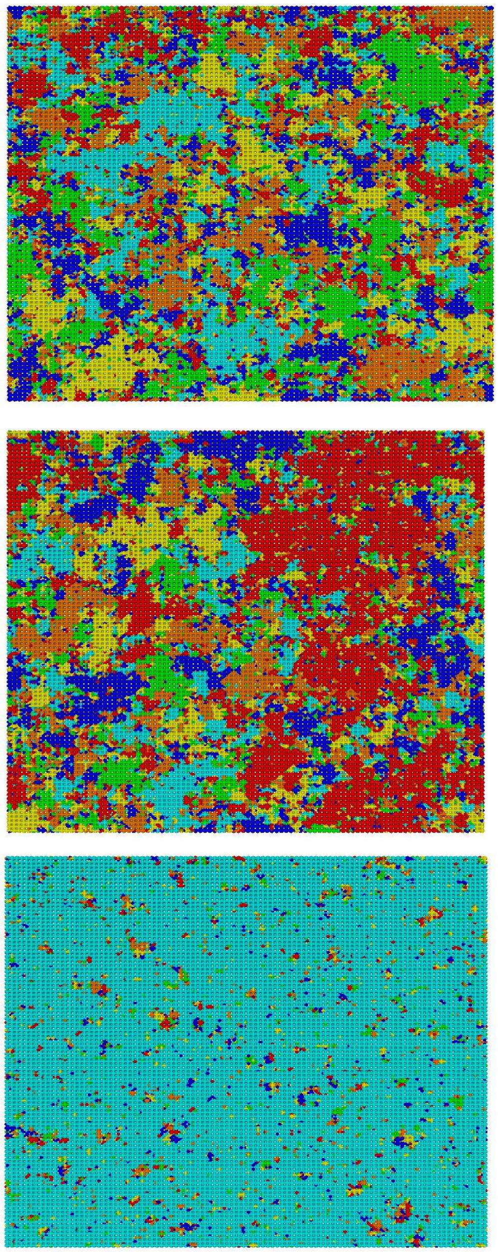

Figure 5.4: Three snapshots of the system with $N = 100 \times 100$, showing Wolff clusters of correlated water molecules. For each molecule we show the states of the four arms and associate different colors to different arm's states. The state points are at pressure close to the critical value P_C ($Pv_0/\epsilon = 0.72 \simeq P_C v_0/\epsilon$) and $T > T_C$ (top panel, $k_B T/\epsilon = 0.0530$), $T \simeq T_C$ (middle panel, $k_B T/\epsilon = 0.0528$), $T < T_C$ (bottom panel, $k_B T/\epsilon = 0.0520$), showing the onset of the percolation at $T \simeq T_C$.

be short on average at this temperature and pressure. Nevertheless, the system appears strongly heterogeneous with the coexistence of large and small clusters, suggesting that the distribution of correlation times evaluated among molecules at a given distance could be strongly heterogeneous. The clusters appear mostly compact but with a fractal surface, suggesting that borders between clusters can rapidly change.

At $T \simeq T_C$ there is one large cluster, in red on the right of the middle panel of Fig. 5.4, with a linear size comparable to the system linear extension and spanning in the vertical direction. The appearance of spanning clusters shows the onset of the percolation geometrical transition. At this state point the correlation time of local, such as Metropolis MC dynamics or molecular dynamics would be very slow as a consequence of the large extension of the structurally correlated region. On the other hand, the correlation time of the Wolff cluster dynamics is short because it changes in one single MC step the state of all the molecules in clusters, some of them with very large size. Once the spanning cluster is formed, it breaks the symmetry of the system and a strong effective field acts on the molecules near its border to induce their reorientation toward a tetrahedral configuration with respect the molecules in the spanning cluster.

As shown in Fig.3, the spanning cluster appears as a fractal object, with holes of any size. The same large distribution of sizes characterizes also the finite clusters in the system. The absence of a characteristic size for the clusters (or the holes of the spanning cluster) is the consequence of the fluctuations at any length-scale, typical of a critical point.

At $T < T_C$ the majority of the molecules belongs to a single percolating cluster that represents the network of tetrahedrally ordered molecules. All the other clusters are small, with a finite size that corresponds to the regions of correlated molecules. The presence of many small clusters gives a qualitative idea of the heterogeneity of the dynamics at these temperatures.

5.6 Summary and conclusions

We describe the numerical solution of mean field equations and the implementation of Wolff cluster MC algorithm for a cell model for liquid water. The mean field approach allows us to estimate in an approximate way the phase diagram of the model at any state point predicting intriguing new results at very low T [184].

To explore the state points of interest for these predictions the use of standard simulations, such as molecular dynamics or Metropolis MC, is not effective due to the onset of the glassy dynamics [172]. To overcome this problem and access the deeply supercooled region of liquid water, we adopt the Wolff cluster MC algorithm. This method, indeed, allows to greatly accelerate the autocorrelation time of the system. Direct comparison of Wolff dynamics with Metropolis dynamics in the vicinity of the liquid-liquid critical point shows a reduction of the autocorrelation time of a factor at least 10^4.

Furthermore, the analysis of the clusters generated during the Wolff MC dynamics allows to emphasize how the regions of tetrahedrally ordered molecules build up on approaching the liquid–liquid critical point, giving rise to the backbone of the tetrahedral hydrogen bond network at the phase transition [187]. The coexistence of clusters of correlated molecules with sizes that change with the state point gives a rationale for the heterogeneous dynamics observed in supercooled water [125, 185, 186].

Chapter 6

Cooperativity of hydrogen bonds and scenarios for water

Water's phase diagram is rich and complex: more than sixteen crystalline phases [2] , and two or more glasses [3]. The liquid state also displays interesting behavior, such as the well known density maximum for 1 atm at 4°C. Thermodynamic response functions, such as the isothermal compressibility K_T and the isobaric specific heat C_P, show anomalous increases upon decreasing temperature T [188]. This behavior is called anomalous because K_T and C_P are proportional to volume fluctuations $\left\langle(\delta V)^2\right\rangle$ and entropy fluctuations $\left\langle(\delta S)^2\right\rangle$, respectively, which are expected to decrease with temperature T [5] for a simple fluid. Further, these quantities display an apparent divergence for 1 atm at -45°C [188], hinting at interesting phase behavior.

A precise understanding of the physico–chemical properties of liquid water is important to provide accurate predictions of the behavior of biological molecules [189], such as the folding-unfolding transitions seen in proteins [190], and the dynamical behavior of DNA [166]. A full understanding of the hydrophobic effect, important in both biology and chemistry, also hinges on a more precise description of liquid water's behavior (add reference). Further lines of research in which water plays an important role include the study of atmospheric processes and the formation of geophysical structures, among others [161].

Microscopically, water's anomalous liquid behavior is understood as resulting from the tendency of neighboring molecules to form hydrogen (H) bonds upon cooling, with a decrease of local potential energy, decrease of local entropy, and increase of local volume. However, the low–temperature phase behavior resulting from these microscopic interactions remains unknown because below the homogenous nucleation temperature T_H (−38°C at 1 atm) crystallization of bulk water is unavoidable, hence the relevant region of the liquid state cannot be probed experimentally.

However, since confinement suppresses crystallization, there has been a series of recent experiments on nanoconfined water exploiting this feature [191–194] that revived the debate on the nature of the phase diagram of water.

In the void of definitive experimental evidence, theoretical and numerical analyses have thrived. Four separate scenarios for the pressure–temperature ($P - T$) phase diagram have been debated:

(i) The *stability limit* (SL) scenario [13, 195] hypothesizes that the superheated liquid-gas spinodal at negative pressure re-enters the positive P region below $T_H(P)$ leading to a divergence of the response functions. It has been noted that thermodynamic consistency requires that any retracing spinodal in the case of water cannot be a liquid-gas spinodal [3].

(ii) The *singularity–free* (SF) scenario [16] hypothesizes that the low-T anticorrelation between volume and entropy, specifically, through the presence of a temperature of maximum density (TMD) locus with a negative slope in the ($P - T$) plane, is sufficient to cause the response functions to increase upon cooling and display maxima at non–zero T, but with no singular behavior.

(iii) The *liquid–liquid critical point* (LLCP) scenario [14, 159] hypothesizes a first–order phase transition line with negative slope in the $P - T$ plane — separating a low density liquid (LDL) from a high density liquid (HDL) — which terminates at a critical point C'. Below the critical pressure $P_{C'}$, therefore in the one–phase region, the response functions increase on approaching the Widom line, defined as the locus of correlation length maxima emanating from C' into the one–phase region, and for $P > P_{C'}$ by approaching the spinodal line. been proposed. Evidence suggests [14, 179, 196] that $P_{C'} > 0$, but the possibility

$P_{C'} < 0$ has been proposed [197].

(iv) The *critical–point free* (CPF) scenario [99] hypothesizes a first–order phase transition line separating two liquid phases and extending to $P < 0$ down to the (superheated) limit of stability of liquid water. No critical point is present.

These four scenarios predict fundamentally different behavior, though they have their bases in the same microscopic interaction: the H bond interaction. A question that naturally arises is whether the macroscopic thermodynamic descriptions are in fact connected in some way. Here we offer a relation linking these four scenarios showing that (i) all can be included in one general scheme and (ii) the balance between the energies of two components of the H bond interaction determines which scenario is valid.

We analyze a microscopic model [174] of water in which the fluid is divided into N cells which communicate through nearest neighbor (n.n.) interactions. The division is such that each cell is in contact with four n.n., mimicking the first shell of liquid water.

The goal of the model is to accurately represent, microscopically, the essential features of the interaction among water molecules, while being able to quantitatively understand the importance of each of these features. To this aim the interaction among cells is separated into four distinct components.

The first component of the interaction is due to the short–range repulsion of the electron clouds. This is incorporated into the model through a maximum density per cell, hence each cell is assigned a volume v_0, and contains a maximum of one molecule.

The second component is due to the long–range attraction of the electron clouds [198], referred to as the van der Waals interaction. In the MF treatment, this leads to an energetic preference for occupied n.n. cells, realized by the Hamiltonian

$$\mathscr{H}_{\mathrm{vdW}} = -\epsilon \sum_{\langle i,j \rangle} n_i n_j, \tag{6.1}$$

where ϵ is the characteristic energy of the attraction, $n_i = 0$ for an unoccupied cell and $n_i = 1$ for an occupied cell, and the sum is over all n.n. pairs $\langle i, j \rangle$.

Water is distinguished from other molecular liquids by its ability to form highly directional H bonds between neighboring molecules. Accordingly, the third component incorporated here is this orientationally–dependent interaction, associated with the covalent nature of the bond [199]. To account for the orientational degrees of freedom of each water molecule, each cell i is assigned a bond variable $\sigma_{ij} = 1, ..., q$ for each n.n. cell j, representing the orientation of cell i with respect to cell j. We choose $q = 6$, giving rise to $6^4 = 1296$ possible orientational states per cell. We say that a bond is formed between cells i and j if $\sigma_{ij} = \sigma_{ji}$.

Experiments show that formation of a H bond leads to a local volume expansion [3], so the total volume is given as

$$V = Nv_0 + N_{HB}v_{HB}, \tag{6.2}$$

where

$$N_{HB} \equiv \sum_{\langle i,j \rangle} n_i n_j \delta_{\sigma_{ij},\sigma_{ji}} \tag{6.3}$$

is the total number of H bonds, and v_{HB} is the specific volume increase due to H bond formation [16]. Bond formation also leads to a decrease in the local potential energy, hence the Hamiltonian in 6.1 is emended by the term

$$\mathscr{H}_{HB} = -JN_{HB}, \tag{6.4}$$

where J is the characteristic energy of the H bond. Because condensation is a result of van der Waals attraction, $J < \epsilon$.

A very desirable feature of a model for a liquid is transferability. The parameters and effective interactions of a model are optimized to precisely reproduce static and dynamic properties of the liquid at one particular thermodynamic state point. The quality of the model is measured by the range of validity of its predictions in other state points. Unfortunately, there is no water model that is truly transferable, nor can reproduce all the properties of water [200]. Many routes have been explored to solve this issue. Molecular polarizability [201, 202] is one way to introduce effects not considered by standard pairwise additive potentials. However, polarizable models are computationally very expensive and provide only a partial solution [203]. An alternative way is to include many–body effects into the potential. For water, four–body and higher order interactions seem to be negligible with respect to the three–body term [204, 205].

A key experimental fact is that at low T the O–O–O angle distribution in water becomes sharper around the tetrahedral value [181], suggesting an interaction that induces a cooperative behavior among bonds. Hence, the fourth component to the interaction potential is the many–body effect due to H bonds [206–208], which minimizes the energy when the H bonds of nearby molecules assume a tetrahedral orientation. This is accomplished by further emending the Hamiltonian in 6.1 and 6.4 with the term

$$\mathscr{H}_{coop} = -J_\sigma \sum_i n_i \sum_{(k,\ell)_i} \delta_{\sigma_{ik},\sigma_{i\ell}}, \tag{6.5}$$

where $(k,\ell)_i$ indicates one of the six different pairs of the four bond variables of molecule i. This interaction introduces a cooperative behavior among bonds, which may be fine tuned by changing J_σ. Choosing $J_\sigma = 0$ leads to H bonds which form independent of neighboring bonds, while $J_\sigma \to \infty$ leads to fully dependent bonds.

The total Hamiltonian is then given by

$$\mathscr{H} = \mathscr{H}_{\text{vdW}} + \mathscr{H}_{HB} + \mathscr{H}_{coop}. \tag{6.6}$$

The model is studied using both mean–field (MF) analysis and Monte Carlo (MC) simulations [172, 177, 179]. Details of the MF and MC techniques are available elsewhere [209].

6.1 Mean-field results

Three qualitatively different phase diagrams are found, depending on the strengths of the H bond energy parameters, J and J_σ. i) *Singularity-free* scenario for $J_\sigma = 0$ (Fig. 6.1a). At high T, liquid (L) and gas (G) phases are separated by a first order transition line (thick line) ending at a critical point C, from which a L–G Widom line emanates. In the liquid phase, the α_P maxima and the K_T maxima increase along lines that converge to a locus (dot–dashed line). The locus of the maxima is related to the L-L Widom line for $T_{C'} \to 0$. ii) *Liquid–liquid critical point* with a positive critical pressure scenario, for $J_\sigma/\epsilon = 0.05$

(Fig. 6.1b). At low T and high P, a high density liquid (HDL) and a low density liquid (LDL) are separated by a first order transition line (thick line) ending in a critical point C', from which the L-L Widom line emanates. We also find a LLCP with a negative critical pressure, for $J_\sigma/\epsilon = 0.3$ (Fig. 6.1c). iii) *Critical–point free* scenario for $J_\sigma/\epsilon = 0.5$ (Fig. 6.1d). The HDL–LDL coexistence line extends to the superheated liquid region at $P < 0$, merging with the liquid spinodal (dotted line) that bends toward negative P. The stability limit (SL) of water at ambient conditions (HDL) is delimited by the superheated liquid–to–gas spinodal and the supercooled HDL–to–LDL spinodal (long–dashed thick line), giving a re-entrant behavior as hypothesized in the SL scenario.

When $J_\sigma = 0$ the model coincides with that proposed in [16], which gives rise to the SF scenario (Fig. 6.1a). For $0 < J_\sigma < a + bJ$, where a and b are fitting parameters [1], the model displays a liquid–liquid transition ending in a LLCP (Fig. 6.1b) [179], which may be tuned such that $P_{C'} > 0$ or $P_{C'} < 0$. For $J_\sigma > a + bJ$, a liquid-liquid transition with no critical point is found, consistent with the CPF scenario (Fig. 6.1c). In Fig. 6.3 we summarize these results in the J/ϵ vs. J_σ/ϵ parameter space.

It is illuminating to look at the limiting behavior between each of the three cases. For $J_\sigma \to 0$, keeping J and other parameters constant, we find that $T_{C'} \to 0$, and the power–law behavior of K_T and the isobaric thermal expansion coefficient α_P is preserved. Further, we find for the entropy S that, for any value of J_σ, $(\partial S/\partial T)_P \propto |T - T_{C'}|^{-1}$. This critical behavior of the derivative of S implies that $C_P \equiv T(\partial S/\partial T)_P$ diverges when $T_{C'}$ is non–zero ($J_\sigma > 0$), but C_P is constant for the case $T_{C'} = 0$ ($J_\sigma = 0$), as found in the SF scenario [16]. Therefore, the SF scenario coincides with the LLCP scenario in the limiting case of $T_{C'} \to 0$ for $J_\sigma \to 0$.

For increasing J_σ, again keeping J constant, we observe that C' moves to larger T and lower P, with $P_{C'} < 0$ for $J_\sigma \gtrsim J/2$. For further increase of J_σ, we observe C' approaching, and eventually intersecting, the liquid–gas spinodal. For larger values of J_σ only the liquid–

---

[1] We fit the boundary of the CPF scenario with the functional form $J_\sigma = a + bJ$, with $a = 0.30 \pm 001$ and $b = 0.36 \pm 0.01$.

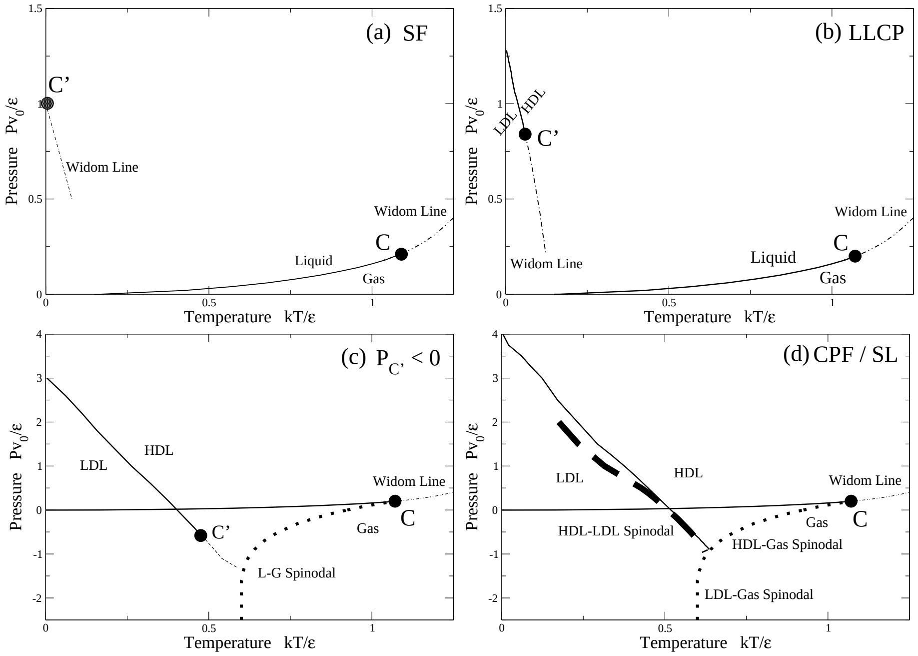

Figure 6.1: Phase diagram predicted from our calculations for the cell model with fixed H bond strength ($J/\epsilon = 0.5$), fixed H bond volume increase ($v_{HB}/v_0 = 0.5$), and different values of the H bond cooperativity strength J_σ. (a) *Singularity-free* scenario ($J_\sigma = 0$) from MF calculations. (b) *Liquid–liquid critical point* with a positive critical pressure scenario (for $J_\sigma/\epsilon = 0.05$) from MF calculations. At low T and high P, a high density liquid (HDL) and a low density liquid (LDL) are separated by a first order transition line (thick line) ending in a critical point C', from which the L-L Widom line emanates. (c) Same as in (b) but with a negative critical pressure (for $J_\sigma/\epsilon = 0.3$). (d) *Critical–point free* scenario ($J_\sigma/\epsilon = 0.5$) from MF calculations. The HDL–LDL coexistence line extends to the superheated liquid region at $P < 0$, merging with the liquid spinodal (dotted line) that bends toward negative P. Other symbols are as in the previous panels. Errors are of the order of the symbol sizes. Lines are guides for the eyes.

liquid transition remains, which is precisely the CPF scenario [99]. Hence the CPF scenario differs from the LLCP scenario only in that C' is now inaccessible, lying beyond the region of liquid states.

In the case of the CPF scenario, we find that the superheated liquid-gas spinodal merges with the supercooled liquid-liquid spinodal, as in Ref. [196]. This gives rise to a liquid spinodal which retraces in the P–T plane, as in the SL scenario. Hence, the CPF scenario and the SL scenario (i) coincide and (ii) correspond to the case in which the cooperative behavior is very strong.

The overall picture that emerges is one in which the amount of cooperativity among H bonds, relative to the H bond strength, governs the location of a liquid-liquid critical point, and hence which scenario is realized. For zero cooperativity, $T_{C'}$ is at zero temperature, and no liquid-liquid transition exists in the positive-T phase space. For moderate cooperativity, a line of liquid-liquid transitions is present, the length of which is proportional to the strength of the cooperativity. For very large cooperativity, C' lies outside the region of stable liquid states, and only the liquid-liquid transition is realized.

6.2 Monte Carlo results

To test our MF calculations, we perform MC simulations in the NPT ensemble, considering a modified version of the model in which we allow for continuous volume fluctuations [179]. To this goal,

(i) we consider that the total volume is $V \equiv V_{MC} + N_{HB} v_{HB}$, where $V_{MC} \geqslant N v_0$ is a dynamical variable allowed to fluctuate in the simulations;

(ii) we assume that the system is homogeneous with all the variables n_i set to 1;

(iii) we replace the first (van der Waals) term of the Hamiltonian in Eq. (6.6) with a Lennard–Jones potential with attractive energy $\epsilon > 0$ and truncated at a hard–core distance

$$U_W(r) \equiv \begin{cases} \infty & \text{if } r \leqslant r_0, \\ \epsilon \left[\left(\frac{r_0}{r}\right)^{12} - \left(\frac{r_0}{r}\right)^{6} \right] & \text{if } r > r_0 \end{cases} \tag{6.7}$$

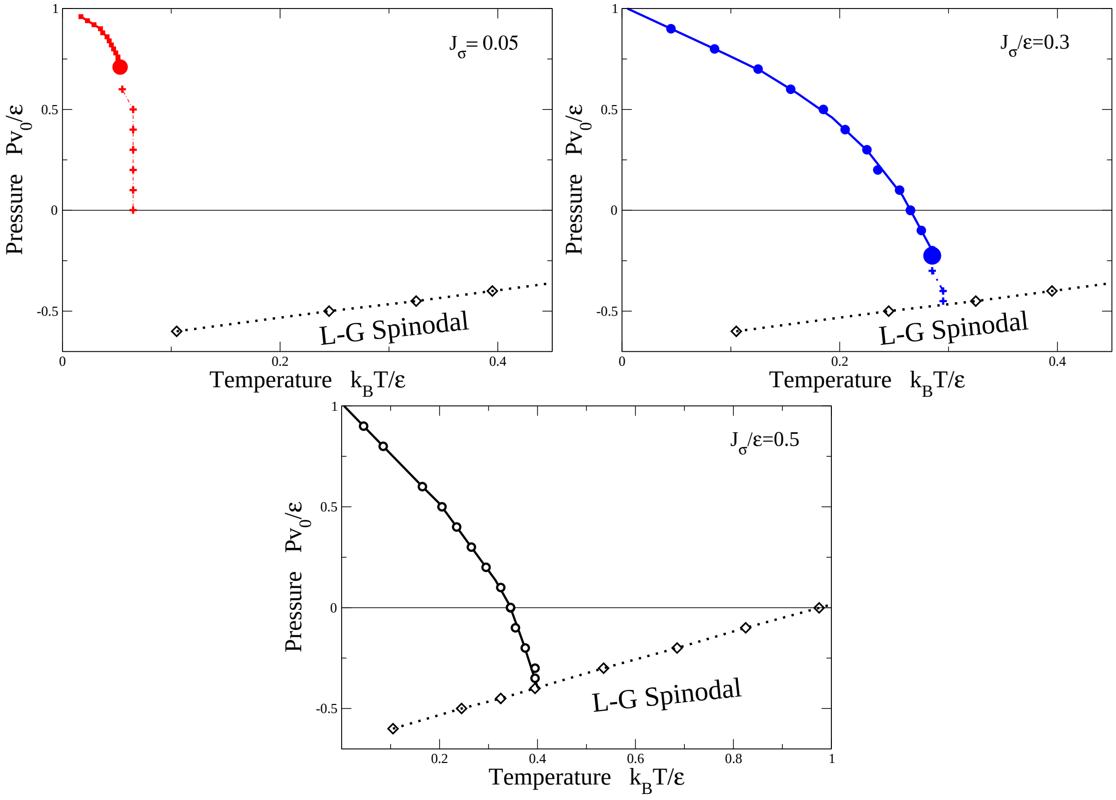

Figure 6.2: Phase diagrams from MC simulations. (a) We find for$J_\sigma/\epsilon = 0.05$, a liquid–liquid phase transition (thick line with symbols) ending in the LLCP at positive pressure. The Widom line (crosses) emanates from the LLCP. (b) We find for$J_\sigma/\epsilon = 0.3$, a liquid–liquid phase transition (thick line with symbols) ending in the LLCP at negative pressure [197]. The Widom line (crosses) emanates from the LLCP. (c) We find for $J_\sigma/\epsilon = 0.5$, the CPF scenario. Other model parameters are as for MF calculations (see text).

where $r_0 \equiv (v_0)^{1/2}$ [2]; the distance between two n.n. molecules is $(V/N)^{1/d}$, and the distance r between two generic molecules is the Cartesian distance between the center of the cells in which they are included. We simulate this system for $N = 10^4$ molecules arranged on a square lattice, adopting Wolff's algorithm to equilibrate at low T [209], for different values of J_σ, keeping J, ϵ and v_{HB}/v_0 constant (Fig. 6.1d).

For large values of J_σ ($J_\sigma = J = 0.5\epsilon$), we find a HDL–LDL first–order phase transition that merges with the superheated liquid spinodal as in the CPF scenario. At lower J_σ ($J_\sigma = 0.6J = 0.3\epsilon$), a HDL–LDL critical point appears at $P < 0$, from which emanates the liquid–liquid Widom line, approximated here as the locus of C_P maxima, which intersects the superheated liquid spinodal. By further decreasing J_σ ($J_\sigma = J/10 = \epsilon/20$), the HDL–LDL critical point occurs at $P > 0$, with the liquid–liquid Widom line intersecting the $P = 0$ axis. By approaching $J_\sigma = 0$ ($J_\sigma = J/25 = \epsilon/50$), we find that the temperature of the HDL–LDL critical point approaches zero and the critical pressure increases toward the value $P = \epsilon/v_0$ independent of J_σ. The liquid–liquid Widom line approaches the $T = 0$ axis for $J_\sigma \to 0$. These results confirm those found with the MF calculations.

We compare our results with those from a thermodynamic model, introduced by Poole et al. [196], in which a van der Waals free energy is augmented to include the effect of H bond formation. There, the H bond interaction is characterized by two free parameters: the strength of the H bond, and a geometrical constraint on H bond formation. The fraction of molecules which form H bonds with decreased energy and entropy is determined by a distribution over molar volumes, the width of which is σ_{Poole}. They show that, by keeping σ_{Poole} fixed, their model displays a SL scenario for weak H bond energy, and a LLCP at positive pressure for strong H bond energy.

We first verify that specific choices of J and J_σ in our cell model produce phase diagrams corresponding to those found by Poole et al. for either weak or strong H bond energy. We find it is by increasing the H bond coupling J in the cell model, while keeping J_σ fixed,

---

[2] To reduce the computational cost, we add a hard–core repulsion at r_0. The presence of this hard–core repulsion does not change the phase diagram of the system.

that switches from the phase diagram corresponding to Poole's SL scenario to the phase diagram corresponding to Poole's LLCP scenario. Hence the measure of H bond strength in the cell model directly compares to the measure of H bond strength in the Poole model.

Next we study the effect of varying the other H bond parameter in Poole's model, the width $\sigma_{\rm Poole}$. Keeping the H bond energy fixed, we are able to produce the LLCP phase behavior at large $\sigma_{\rm Poole}$ and the SL phase behavior at small $\sigma_{\rm Poole}$. Hence a decrease of $\sigma_{\rm Poole}$ has the same effect on the phase diagram as an increase in the H bond cooperativity in our model. This makes sense physically, as a more all-or-nothing distribution of H bonds implies a more cooperative process of formation. It also implies that the Poole model gives rise to the SF scenario only in the limiting case of infinite $\sigma_{\rm Poole}$.

We conclude that both models give a consistent physical picture. This observation is an important step towards showing that our result, summarized in Fig. 6.3, is model–independent.

We argue that each of the four scenarios proposed for the phase diagram of liquid water may be viewed as a special case of a more general scheme. We propose that a possible way to understand which case best describes water is to probe the energy of the covalent part of the H bond interaction [199] and the energy of the cooperative component of the H bond interaction [206–208], the two physical parameters which give rise to this scheme.

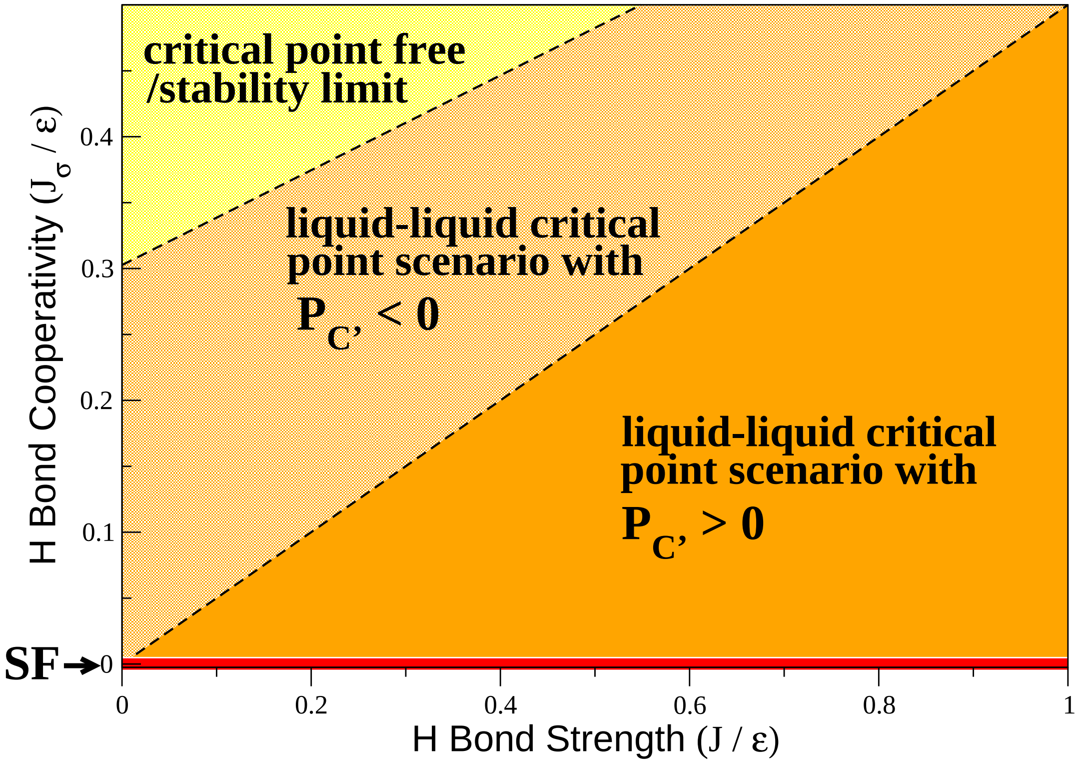

Figure 6.3: Possible scenarios for water for different values of J, the H bond strength, and J_σ, the strength of the cooperative interaction, both in units of the van der Waals energy ϵ. The ratio v_{HB}/v_0 is kept constant. (i) If $J_\sigma = 0$ (red line), water would display the singularity free (SF) scenario, independent of J. (ii) For large enough J_σ, water would possess a first–order liquid–liquid phase transition line terminating at the liquid–gas spinodal—the critical point free (CPF) scenario; the liquid spinodal would retrace at negative pressure, as in the stability limit (SL) scenario (yellow region). (iii) For other combinations of J and J_σ, water would be described by the liquid–liquid critical point (LLCP) scenario. For large J_σ, the LLCP is at negative pressure (ochre region). For small J_σ, the LLCP is at positive pressure (orange region). Dashed lines separating the three different regions correspond to mean field results of the microscopic cell model. The $P - T$ phase diagram evolves continuously as J and J_σ change.

Appendices

Appendix A

Molecular dynamics simulations

The liquid state of matter lies between two other states, the solid and gaseous phase, for which we have simple and powerful models, the harmonic crystal and the ideal gas, respectively. These two models exploit the presence of perfect order or complete absence of it. Since a liquid is an intermediate state of matter, a simple general model is lacking. For these reasons, the study of the liquid state has posed many experimental and theoretical challenges.

A new route of exploration was opened with the invention of computers. in the middle of the XX century, which allowed to perform "numerical experiments" In a computer experiment very complex and more realistic models can be tested to be compared with real experiments. Also, conceptual experiments can be performed with the aim to give insight into natural phenomena.

The first computer simulation of a liquid was performed at the Los Alamos National Laboratories (USA) in 1953 [210]. This seminal work established the method of modern Monte Carlo (MC) simulations, which, though, can provide information only on thermodynamic quantities.

To access information on the dynamics of a many–body system we need a different technique: molecular dynamics (MD). The temporal evolution of a system of interacting atoms is determined, in MD, by solving the equations of motion. We will consider only systems obeying classical mechanics, thus we will need to solve Newton equations

$$\mathbf{F}_i = m_i \mathbf{a}_i \tag{A.1}$$

for every atom i of the system, where m_i is the mass, $\mathbf{a}_i \equiv d^2\mathbf{r}_i/dt^2$ the acceleration, and $\mathbf{F}_i$ the force on atom i. The MD is a deterministic method: given the initial set of positions and velocities of the atoms, the subsequent evolution, the *trajectory*, is, in principle, completely determined[1].

Given a system of N particles, the computer calculates a trajectory in a phase space with $6N$ dimensions, $3N$ for the positions and $3N$ for the momenta. MD is an analysis method of statistical mechanics, that provides a set of configurations distributed according to statistical distribution function, or statistical ensemble, such as the *microcanonical* or *canonical* ensemble. In a simulation, the calculation of a given physical observable is simply done as an arithmetic average of the instantaneous values of that observable during the simulation. In the limit of very long simulations times, the simulated system will explore all the phase space available. In practice, computer simulations are always of finite length and special precautions must be taken.

A.1 Equations of motion

In this section we will describe the techniques used to solve the classical equation of motionfor a system of N particles interacting through a potential $\mathscr{V}$. The most fundamental equations of motion probably are the Euler–Lagrange equations

$$\frac{d}{dt}\left(\frac{\partial \mathscr{L}}{\partial \dot{q}_k}\right) - \left(\frac{\partial \mathscr{L}}{\partial q_k}\right) = 0 \tag{A.2}$$

where the Lagrangian $\mathscr{L}(\mathbf{q}, \dot{\mathbf{q}})$ is defined, for the class of systems under consideration here, as a sum of kinetic and potential energy

$$\mathscr{L} = \mathscr{K} - \mathscr{V} \quad . \tag{A.3}$$

---

[1] In practice, because of the finite integration step and the inevitable approximations employed, the calculated trajectory will deviate from the real one.

If we consider a system of atoms with Cartesian coordinates $\mathbf{r}_i$, then Eq. A.2 becomes

$$m_i \ddot{\mathbf{r}}_i = \mathbf{F}_i \tag{A.4}$$

which are Newton equations for the system under consideration, where m_i is tha mas of atom i and

$$\mathbf{F}_i = -\nabla_{\mathbf{r}_i} \mathscr{V} \tag{A.5}$$

is the force exterted on atom i.

A standard method of solving ordinary differential equations as Eq. A.4 is the finite difference method. The general idea is the following: given the positions, velocities and other dynamic variables at time t for the atoms, the same quantities are calculated at time $t + \delta t$ with sufficient accuracy. The equation of motion are solved, *integrated*, step by step in the discretized temporal variable t; the choice of the time step δt depends on the specific method of integration adopted, but δt must be larger than the time employed by a molecule to travel a molecular diameter.

Now, we will describe a very common integration scheme, the *leap–frog algorithm.* For small time intervals we can cansider a Taylor expansion of the atomic coordinates

$$\mathbf{r}(t + \delta t) = \mathbf{r}(t) + \mathbf{v}(t)\delta t + \frac{1}{2}\mathbf{a}(t)\delta t^2 + \frac{1}{6}\frac{d^3\mathbf{r}(t)}{dt^3}\delta t^3 + \ldots \tag{A.6}$$

and similarly for the velocities. Now, we consider the two following Taylor expansions for the velocities

$$\mathbf{v}(t + \frac{1}{2}\delta t) = \mathbf{v}(t) + \mathbf{a}(t)\frac{1}{2}\delta t + O(\delta t^2) \tag{A.7}$$

$$\mathbf{v}(t - \frac{1}{2}\delta t) = \mathbf{v}(t) - \mathbf{a}(t)\frac{1}{2}\delta t + O(\delta t^2) \tag{A.8}$$

by subtracting the second from the the first we obtain

$$\mathbf{v}(t + \frac{1}{2}\delta t) = \mathbf{v}(t - \frac{1}{2}\delta t) + \mathbf{a}(t)\delta t + O(\delta t^3). \tag{A.9}$$

Next, we expand in Taylor series the coordinates about $t + \frac{1}{2}\delta t$ with increment $\pm\frac{1}{2}\delta t$

$$\mathbf{r}(t + \frac{1}{2}\delta t + \frac{1}{2}\delta t) = \mathbf{r}(t + \delta t) = \mathbf{r}(t + \frac{1}{2}\delta t) + \mathbf{v}(t + \frac{1}{2}\delta t)\frac{1}{2}\delta t + O(\delta t^2) \tag{A.10}$$

$$\mathbf{r}(t + \frac{1}{2}\delta t - \frac{1}{2}\delta t) = \mathbf{r}(t) = \mathbf{r}(t + \frac{1}{2}\delta t) - \mathbf{v}(t + \frac{1}{2}\delta t)\frac{1}{2}\delta t + O(\delta t^2), \tag{A.11}$$

again, by subtracting the second from the the first, we finally find

$$\mathbf{r}(t+\delta t) = \mathbf{r}(t) + \mathbf{v}(t+\frac{1}{2}\delta t)\delta t. \tag{A.12}$$

We collect here the final results

$$\mathbf{r}(t+\delta t) = \mathbf{r}(t) + \mathbf{v}(t+\frac{1}{2}\delta t)\delta t \tag{A.13}$$

$$\mathbf{v}(t+\frac{1}{2}\delta t) = \mathbf{v}(t-\frac{1}{2}\delta t) + \mathbf{a}(t)\delta t. \tag{A.14}$$

The leap–frog algorithm consists of Eq. A.13 and A.14. The velocity equation is implemented first, because of which the velocites leap over the coordinates (from this feature the algorithm derives its name); then the coordinate equation is implemented. The velocities at time t, useful, e.g., to calculate the instantaneous value of the energy, are obtained from

$$\mathbf{v}(t) = \frac{1}{2}\left(\mathbf{v}(t+\frac{1}{2}\delta t) + \mathbf{v}(t-\frac{1}{2}\delta t)\right). \tag{A.15}$$

Finally, we note that the error intrinsic in the leap–frog algorithm is of order δt^3 in the individual time step. However, this error accumulates over the total length of the simulation t_{tot}; the total error is of order δt^3 times the number of intervals $t_{tot}/\delta t$, hence, the total error is of order δt^2.

A.2 The SPC/E model of water

We describe here a molecular model of water, widely used in MD simulations. The SPC/E [48] model describes water as a planar molecules with three point–like interaction sites corresponding to the centers of the hydrogen (H) and oxygen (O) atoms. The SPC/E model assumes a rigid geometry, which means that the OH distance is held fixed at 1.0 Å and the HOH angle has also a fixed value of $\theta = 109.47°$, corresponding to the tetrahedral angle.

Every water molecule interacts with the others through a Lennard–Jones potential

$$V_{LJ}(r) \equiv 4\epsilon\left[\left(\frac{\sigma}{r}\right)^{12} - \left(\frac{\sigma}{r}\right)^{6}\right] \tag{A.16}$$

where r is the distance between the oxygens of two molecules, and the Lennard–Jones parameters for the SPC/E model are $\sigma = 3.166$ Å and $\epsilon = 0.6502$ kJ mol^{-1}. The length σ

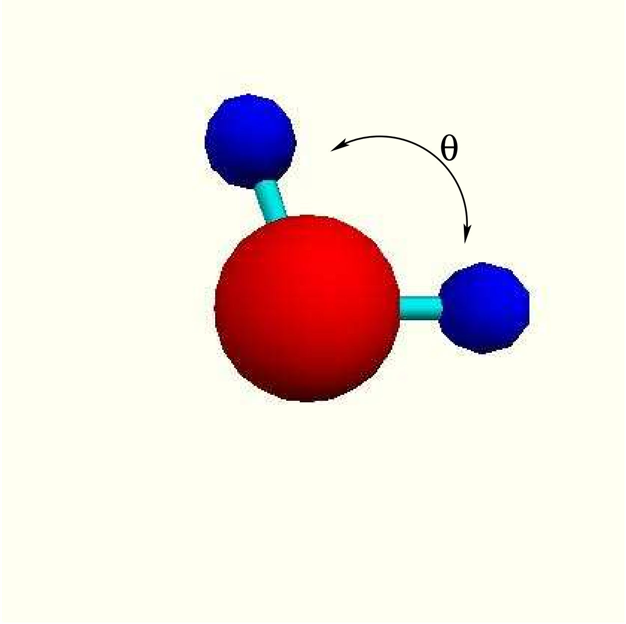

Figure A.1: Schematic of the SPC/E water molecule showing the oxygen and hydrogen atoms; marked on the figure is the HOH angle $\theta = 109.47°$.

corresponds to an effective molecular radius. The electrostatic interaction is also explicitly considered. Each hydrogen has a charge $q_H = 0.4238\,e$, and the oxygen charge is $q_O = -2.0\,q_H$, where e is the magnitude of the electron charge.

Finally, we note that the SPC/E model does not take into account electric polarizability or the flexibility of the molecular geometry. For a review of different classes of models see Ref. [211].

Appendix B

Monte Carlo simulations

The Monte Carlo (MC) technique plays a fundamental role in the numerical resolution of problems in statistical physics, condensed matter physics, and lattice gauge theories [212, 213]. It was developed at the Los Alamos National Laboratory, and the expression "Monte Carlo" appeared for the first time in a paper in 1949 by Metropolis and Ulam [214]. The Metropolis method — the most widespread MC method — was explained for the first time by Metropolis, Rosenbluth, Rosenbluth, Teller and Teller in 1953 [210]. Since then, myriad of different techniques and algorithms have been developed to tackle problems by randomly sampling the available phase space.

The fundamental idea of MC algorithms is to simulate random thermal fluctuations in the system, by moving through a set of states that are generated according to the appropriate probability distribution function, typically the Boltzmann distribution. This scheme is useful to compute quantities such as

$$\langle A \rangle = \frac{\int \mathrm{d}\mathbf{r}^N A(\mathbf{r}^N) \exp[-\beta U(\mathbf{r}^N)]}{\int \mathrm{d}\mathbf{r}^N \exp[-\beta U(\mathbf{r}^N)]}, \tag{B.1}$$

which is a ratio of two integrals. It is important to note that, in general, in computer simulations or experiments, we can not calculate or measure directly quantities such as the Helmoltz free energy,

$$F = -k_B T \ln Q(N, V, T) \equiv -k_B T \ln \left(\frac{\mathrm{d}\mathbf{p}^N \mathrm{d}\mathbf{r}^N \exp[-\beta \mathscr{H}(\mathbf{p}^N, \mathbf{r}^N)]}{\Lambda^{3N} N!} \right) \tag{B.2}$$

or entropy, because they are not averages of a function of positions and momenta, but rather they depend on the total volume in phase space available to the system [215].

Below, we will briefly describe two of the most commonly used algorithms to sample the phase space: the Metropolis algorithm and the Wolff algorithm.

B.1 Metropolis algorithm

In a MC simulation we want to create an algorithm that generates randomly a new state ν from an initial state μ. We indicate with $P(\mu \to \nu)$ the *transition probability* of changing microscopic state from μ to ν. $P(\mu \to \nu)$ should i) not depend on time, and ii) depend only on state μ and not on the previous history of the system[1].

As the system changes state according to the rule $P(\mu \to \nu)$, it should reach an equilibrium in which different states are sampled according to the Boltzmann distribution. The condition of detailed balance guarantees that the system will reach this desired equilibrium if the transition probabilities satisfy

$$\frac{P(\mu \to \nu)}{P(\nu \to \mu)} = e^{-\beta(E_\nu - E_\mu)} \tag{B.3}$$

where E_μ and E_ν are the energy of the system in state μ and ν respectively.

It turns out that it is useful to break the transition probability into two steps

$$P(\mu \to \nu) = s(\mu \to \nu)A(\mu \to \nu) \tag{B.4}$$

where $s(\mu \to \nu)$ is the *selection probability*, the probability for the algorithm to generate a candidate new state ν, and $A(\mu \to \nu)$ is the *acceptance ratio*, the numeber of times that the new ν state is accepted and the system moves to this new state. Now, there is a lot of freedom to choose $s(\mu \to \nu)$ and $A(\mu \to \nu)$, since Eq. B.3 fixes only the ratio

$$\frac{P(\mu \to \nu)}{P(\nu \to \mu)} = \frac{s(\mu \to \nu)A(\mu \to \nu)}{s(\nu \to \mu)A(\nu \to \mu)}. \tag{B.5}$$

To be more clear, we now consider a specific system to study using the Metropolis scheme. We consider the Ising model for a set of N spins, described by the following

---

[1] This is the definition of a Markov process.

Hamiltonian

$$\mathscr{H} = -J\sum_{\langle ij\rangle} s_i s_j - B\sum_i s_i \tag{B.6}$$

where $s_i = \pm 1$ is the value of spin i, $J > 0$ is the ferromagnetic coupling constant, B an external magnetic field, and $\langle ij\rangle$ denotes nearest–neighbors.

The Metropolis algorithm generates a single spin–flip dynamics, because a new state is selected by choosing only one spin to flip at a time. Thus, since there are N spin that can be randomly chosen, the selection probability is

$$s(\mu \to \nu) = \frac{1}{N} \tag{B.7}$$

which is constant, therefore, it drops out of Eq. B.3. It turns out that a very efficient choice for the acceptance ratio is

$$A(\mu \to \nu) = \begin{cases} e^{-\beta(E_\nu - E_\mu)} & \text{if } E_\nu - E_\mu > 0 \\ 1 & \text{otherwise.} \end{cases} \tag{B.8}$$

The Metropolis algorithm is completely determined by Eq. B.7 and Eq. B.8.

B.2 Wolff algorithm

The Metropolis algorithm is very efficient at relatively high temperatures. However, it becomes increasingly inefficient upon approacing the critical temperature T_c. The reason for this is the presence of large domains of spins all pointing in the same direction. Therefore, it is very hard to change the state of the system by flipping one spin per move. since its neighbors will be pointing in the original direction, the candidate move will be almost certainly rejected. The correlation length τ grows with the correlation length ξ as

$$\tau \sim \xi^z \tag{B.9}$$

where z is the *dynamic critical exponent.* This growth of the relaxation time near T_c is known as the critical slowing down. For finite systems, as any real simulation, of linear lenght L in d–dimensions, the computer time τ_{CPU} grows as

$$\tau_{CPU} \sim L^{d+z} \tag{B.10}$$

which makes simulations of larger systems near the critical point impracticable.

In 1989, Wolff [173] devised an algorithm to reduce drastically the critical slowing down. Building on the results by Swendsen and Wang [216], which in turn used the theory of Fortuin, Kasteleyn, Coniglio and Klein [217, 218], Wolff proposed to construct clusters of physically correlated spins, and then to flip them all at once. This idea exploits the fact that these clusters are the thermodynamically relevant objects in the dynamics near a critical point. These are the steps of the Wolff algorithm for an Ising system:

1. Select randomly a seed spin from which the cluster will grow.
2. Check the neighboring spins and, if they have the same value as the initial spin, add them to the cluster with probability $P_{add} \equiv 1 - e^{-2\beta J}$
3. For any newly added spin, check also its neighbors if they can be included into the cluster. The probability of adding them is the same P_{add}.
4. Once all the possibilities are exhausted, flip all the spins in the cluster.

This algorithm satisfies detailed balance and generates states distributed according to the Boltzmann distribution. The dynamic exponent for the Wolff algorithm is $z = 0.25 \pm 0.01$ [213], which is much lower than $z = 2.17$ for the Metropolis case.

Appendix C

Landau–Placzek ratio

The hydrodynamic regime of a fluid is described by the Navier–Stokes equation, which require the specification of three transport coefficient for the system: the thermal conductivity Λ, the shear viscosity η, and the bulk viscosity ζ. In this appendix we consider how scattering experiments can provide information on transport coefficients and the specific heat of the fluid.

We start by defining the building blocks that are necessary to define the time–dependent correlation function measured in an experiment. First, we consider the time–dependent number density

$$\rho(\mathbf{r},t)=\sum_{i=1}^{N}\delta\left[\mathbf{r}-\mathbf{r}_i(t)\right], \tag{C.1}$$

which is related to the time–dependent *van Hove correlation function*

$$G(\mathbf{r},t)\equiv\left\langle\frac{1}{N}\sum_{i=1}^{N}\sum_{j=1}^{N}\int\delta[\mathbf{r}-\mathbf{r}_j(t)+\mathbf{r}_i(0)]\mathrm{d}\mathbf{r}\right\rangle, \tag{C.2}$$

and this last one can be written as

$$\begin{aligned}G(\mathbf{r},t)&=\left\langle\frac{1}{N}\int\sum_{i=1}^{N}\sum_{j=1}^{N}\delta[\mathbf{r}'+\mathbf{r}-\mathbf{r}_j(t)]\,\delta[\mathbf{r}'-\mathbf{r}_i(0)]\mathrm{d}\mathbf{r}\,\mathrm{d}\mathbf{r}'\right\rangle\\&=\left\langle\frac{1}{N}\int\rho(\mathbf{r}'+\mathbf{r},t)\,\rho(\mathbf{r}',0)\mathrm{d}\mathbf{r}'\right\rangle=\frac{1}{\rho}\left\langle\rho(\mathbf{r},t)\,\rho(\mathbf{0},0)\right\rangle.\end{aligned} \tag{C.3}$$

Thus, the van Hove correlation function corresponds, physically, to the density–density time–correlation function. A correlation function can also be studied in momentum space.

The Fourier transform of the van Hove function

$$F(\mathbf{k},t) = \int G(\mathbf{r},t)\exp(-i\mathbf{k}\cdot r)\mathrm{d}\mathbf{r} \tag{C.4}$$

is called the *intermediate scattering function*, a very useful quantity to calculate in numerical simulations.

The temporal Fourier transform of $F(\mathbf{k},t)$

$$S(\mathbf{k},\omega) = \frac{1}{2\pi}\int_{-\infty}^{\infty} F(\mathbf{k},t)\exp(i\omega t)\mathrm{d}t \tag{C.5}$$

is known as the *dynamic structure factor*. $S(\mathbf{k},\omega)$ is physically relevant because it can be directly measured through, e.g., inelastic neutron scattering, in which case $\hbar\mathbf{k}$ and $\hbar\omega$ are respectively the momentum and energy transferred by the scattering neutron to the target.

It is possible to show [15, 49] that in the hydrodynamic regime, where the wavelength $\lambda = 2\pi/|\mathbf{k}|$ is considerably larger than the correlation length ξ, $S(\mathbf{k},\omega)$ can be written as

$$\begin{aligned}\frac{S(\mathbf{k},\omega)}{S(\mathbf{k})} = \left(1-\frac{C_V}{C_P}\right)\frac{2D_Tq^2}{\omega^2+(D_Tq^2)^2} + \frac{C_V}{C_P}\Bigg\{&\frac{1/2D_sq^2}{(w-c_sq)^2+(1/2D_sq^2)^2}\\ &+\frac{1/2D_sq^2}{(w+c_sq)^2+(1/2D_sq^2)^2}\Bigg\}\end{aligned} \tag{C.6}$$

where

$$D_T \equiv \frac{\Lambda}{\rho C_P} \tag{C.7}$$

is the thermal diffusivity, and

$$D_s \equiv D_T\left(\frac{C_P}{C_V}-1\right)+\frac{1}{\rho}\left(\frac{4}{3}\eta+\zeta\right) \tag{C.8}$$

is the sound attenuation coefficient. The power spectrum of the density fluctuations, $S(\mathbf{k},\omega)$, is composed of three Lorentzian lineshapes: i) the *Rayleigh line*, centered at $\omega = 0$ with half–width $\Gamma_R = D_Tq^2$, and ii) the *Brillouin doublet*, centered at $\omega = \pm c_sq$ with half–width $\Gamma_B = \frac{1}{2}D_sq^2$.

It is possible to show [219] that the Rayleigh line corresponds to non–propagating fluctuations in entropy at constant pressure, while the Brillouin doublet corresponds to propagating pressure fluctuations at constant entropy, i.e., sound waves. In Fig. C.1 we show

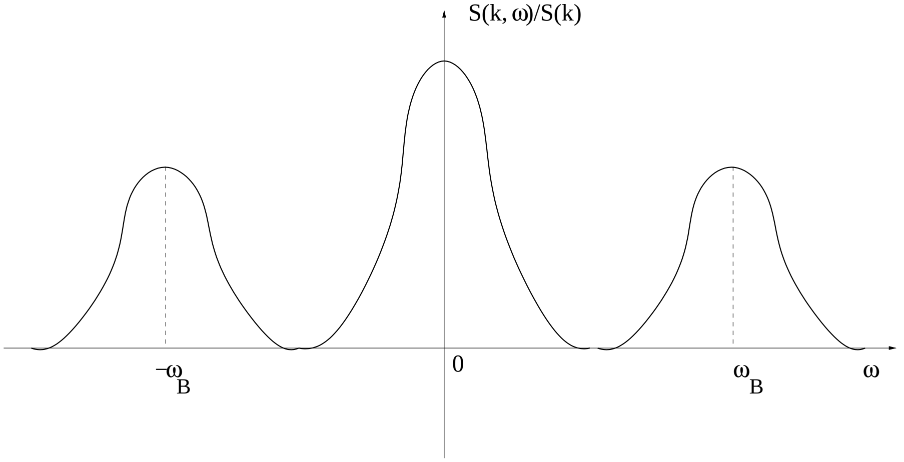

Figure C.1: Dynamic structure factor for a fluid in the hydrodynamic regime as a function of ω for a fixed value of T and wavevector $\mathbf{k}$.

a schematic plot of $S(\mathbf{k}, \omega)/S(\mathbf{k})$ for a fluid as a function of ω for a fixed value of T and wavevector $\mathbf{k}$.

From Eq. C.6 we see that he total integrated area of the Rayleigh linewidth is

$$I_{\mathrm{R}} \equiv 1 - \frac{C_V}{C_P} \tag{C.9}$$

and the integrated area of both Brillouin linewidths is

$$2I_{\mathrm{B}} \equiv \frac{C_V}{C_P}. \tag{C.10}$$

Equation C.9 and C.10 imply that

$$\frac{I_{\mathrm{R}}}{2I_{\mathrm{B}}} = \frac{C_P}{C_V} - 1 \tag{C.11}$$

which is known as the *Landau–Placzek ratio.* Incidentally, because of the normalization of Eq. C.6, the following identity is valid

$$I_{\mathrm{R}} + 2I_{\mathrm{B}} = 1. \tag{C.12}$$

The intensity of the scattered radiation is proportional to the mean–square fluctuations of the dielectric constant, $\left\langle(\Delta\epsilon)^2\right\rangle$ [219]. Futhermore, the fluctuation–dissipation theorem applied to the absorption coefficient $\alpha(\omega)$ gives [220]

$$\alpha(\omega) = \frac{2\pi\omega^2\beta}{3nc}\int_{-\infty}^{\infty} dt e^{-i\omega t}\left\langle \mathbf{M}(0)\mathbf{M}(t)\right\rangle \tag{C.13}$$

This last relation, along with a macroscopic theory of the dielectric properties of a fluid can provide a link to the Landau–Placzek ratio, and therefore to the ratio of isobaric and isochoric specific heats.

Bibliography

[1] R. Waller, *(trans.) Essays of Natural Experiments*, (original in Italian by the secretary of the Accademia del Cimento); facsimile of the 1684 English translation (Johnson Reprint, New York, 1964).

[2] E. A. Zheligovskaya and G. G. Malenkov, Russian Chemical Review **75**, 57 (2006).

[3] P. G. Debenedetti, Journal of Physics: Condensed Matter **15**, R1669 (2003).

[4] L. Pauling, *The Nature of the Chemical Bond*, Cornell University Press, Ithaca, (1960).

[5] L. D. Landau and E. M. Lifshitz, *Statistical Physics*, 2nd edn. Pergamon Press, Oxford, (1960).

[6] G. S. Kell, Journal of Chemical & Engineering Data **12**, 66 (1967).

[7] M. D. Ediger, C. A. Angell, and S. R. Nagel, Journal of Physical Chemistry **100**, 13200 (1996).

[8] V. Velikov, S. Borick, and C. A. Angell, Science **294**, 2335 (2001).

[9] M. Chaplin, http://www.lsbu.ac.uk/ .

[10] C. A. Angell, W. J. Sichina, and M. Oguni, Journal of Physical Chemistry **86**, 998 (1982).

[11] R. J. Speedy and C. A. Angell, Journal of Chemical Physics **65**, 851 (1976).

[12] H. E. Stanley, S. V. Buldyrev, M. Canpolat, O. Mishima, M. R. Sadr-Lahijany, A. Scala, and F. W. Starr, Physical Chemistry Chemical Physics **2**, 1551 (2000).

[13] R. J. Speedy, Journal of Physical Chemistry **86**, 982 (1982).

[14] P. H. Poole, F. Sciortino, U. Essmann, and H. E. Stanley, Nature (London) **360**, 324 (1992).

[15] H. E. Stanley, *Introduction to Phase Transitions and Critical Phenomena*, Oxford University Press, 1971.

[16] S. Sastry, P. G. Debenedetti, F. Sciortino, and H. E. Stanley, Physical Review E **53**, 6144 (1996).

[17] L. P. N. Rebelo, P. G. Debenedetti, and S. Sastry, Journal of Chemical Physics **109**, 626 (1998).

[18] Y. Xie, K. F. Ludwig, G. Morales, D. E. Hare, and C. M. Sorensen, Physical Review Letters **71**, 2050 (1993).

[19] G. Adam and J. H. Gibbs, Journal of Chemical Physics **43**, 139 (1965).

[20] F. Sciortino, P. Gallo, P. Tartaglia, and S.-H. Chen, Physical Review E **54**, 6331 (1996).

[21] F. Sciortino, L. Fabbian, S.-H. Chen, and P. Tartaglia, Physical Review E **56**, 5397 (1997).

[22] W. Kob and H. C. Anderson, Physical Review Letters **73**, 1376 (1994).

[23] F. W. Starr, F. Sciortino, and H. E. Stanley, Physical Review E **60**, 6757 (1999).

[24] S. Harrington, F. Sciortino, and H. E. Stanley, Physical Review Letters **82**, 3629 (1999).

[25] W. Götze, Journal of Physics: Condensed Matter **11**, A1 (1999).

[26] W. Götze, *Liquids, Freezing and Glass Transition,* edited by J. P. Hansen, D. Levesque, and J. Zinn-Justin (North-Holland, Amsterdam 1991), 1991.

[27] K. Schmidt-Rohr and H. W. Spiess, Physical Review Letters **66**, 3020 (1991).

[28] J. Liesen, K. Schmidt-Rohr, and H. W. Spiess, Journal of Non–Crystalline Solids **172-174**, 737 (1994).

[29] A. Heuer, M. Wilhelm, H. Zimmermann, and H. W. Spiess, Physical Review Letters **75**, 2851 (1995).

[30] M. T. Cicerone and M. D. Ediger, Journal of Chemical Physics **103**, 5684 (1995).

[31] F. Fujara, B. Geil, H. Sillescu, and G. Fleischer, Zeitschrift für Physik **88**, 195 (1992).

[32] M. T. Cicerone, F. R. Blackburn, and M. D. Ediger, Journal of Chemical Physics **102**, 471 (1995).

[33] M. Hurley and P. Harrowell, Physical Review E **52**, 1694 (1995).

[34] A. I. Mel'cuk, R. A. Ramos, H. Gould, W. Klein, and R. D. Mountain, Physical Review Letters **75**, 2522 (1995).

[35] T. Muranaka and Y. Hiwatari, Physical Review E **51**, R2735 (1995).

[36] W. Kob, C. Donati, S. J. Plimpton, P. H. Poole, and S. C. Glotzer, Physical Review Letters **79**, 2827 (1997).

[37] P. H. Poole, S. C. Glotzer, A. Coniglio, and N. Jan, Physical Review Letters **78**, 3394 (1997).

[38] C. Angell, K. Ngai, G. McKenna, P. McMillan, and S. Martin, Journal of Applied Physics **88**, 3113 (2000).

[39] C. Donati, J. F. Douglas, W. Kob, S. J. Plimpton, P. H. Poole, and S. C. Glotzer, Physical Review Letters **80**, 2338 (1998).

[40] C. Donati, S. C. Glotzer, P. H. Poole, W. Kob, and S. J. Plimpton, Physical Review E **60**, 3107 (1999).

[41] B. Doliwa and A. Heuer, Physical Review Letters **80**, 4915 (1998).

[42] R. Böhmer, G. Hinze, G. Diezemann, B. Geil, and H. Sillescuet, Europhysics Letters **36**, 55 (1996).

[43] B. Schiener, R. Böhmer, A. Loidl, and R. V. Chamberlin, Science **274**, 752 (1996).

[44] W. K. Kegel and A. van Blaaderen, Science **287**, 290 (2000).

[45] H. Sillescu, Journal of Non–Crystalline Solids **243**, 81 (1999).

[46] M. D. Ediger, Annual Review Physical Chemistry **51**, 99 (2000).

[47] E. R. Weeks, J. C. Crocker, A. C. Levitt, A. Schofield, and D. A. Weitz, Science **287**, 627 (2000).

[48] H. J. C. Berendsen, J. R. Grigera, and T. P. Straatsma, Journal of Physical Chemistry **91**, 6269 (1987).

[49] J. P. Hansen and I. R. McDonald, *Theory of Simple Liquids*, Academic Press, London, 1986.

[50] Y. Gebremichael, T. B. Schrøder, F. W. Starr, and S. C. Glotzer, Physical Review E **64**, 051503 (2001).

[51] C. Bennemann, C. Donati, J. Baschnagel, and S. C. Glotzer, Nature (London) **399**, 246 (1999).

[52] Y. Gebremichael, T. B. Schrøder, and S. C. Glotzer, Abstracts of the American Chemical Society **220**, 412 (2000).

[53] I. Ohmine and H. Tanaka, Chemical Reviews **93**, 2545 (1993).

[54] S. C. Glotzer, Journal of Non–Crystalline Solids **274**, 342 (2000).

[55] D. N. Perera and P. Harrowell, Journal of Non–Crystalline Solids **235**, 314 (1998).

[56] J. Garrahan and D. Chandler, Physical Review Letters **89**, 035704 (2002).

[57] A. Scala, Nature (London) **406**, 166 (2000).

[58] N. Giovambattista, S. V. Buldyrev, F. W. Starr, and H. E. Stanley, Physical Review Letters **90**, 085506 (2003).

[59] J. Kim and T. Keyes, Chemical Physics **121**, 4237 ((2004)).

[60] M. Ribeiro, Physical Chemistry Chemical Physics **6**, 771 (2004).

[61] G. Matsui and S. Kojima, Physics Letters A **293**, 156 (2002).

[62] I. M. Svishchev and P. G. Kusalik, **98**, 728 (1994).

[63] S. Kämmerer, W. Kob, and R. Schilling, Physical Review E **58**, 2141 (1998).

[64] L. Fabbian, F. Sciortino, and P. Tartaglia, Journal of Non–Crystalline Solids **235-237**, 325 (1998).

[65] A. Rahman, Physical Review **136**, A405 (1964).

[66] L. Fabbian, A. Latz, R. Schilling, F. Sciortino, P. Tartaglia, and C. Theis, Physical Review E **60**, 5768 (1999).

[67] L. Bosio, S. H. Chen, and J. Teixeira, Physical Review A **27**, 1468 (1983).

[68] A. Einstein, *Investigations on the Theory of the Brownian Motion*, Dover, New York, 1956.

[69] P. Debye, *Polar Molecules*, Dover, New York, 1929.

[70] R. A. L. Jones, *Soft Condensed Matter*, Oxford Univ. Press, Oxford, 2002.

[71] L. Andreozzi, M., M. Faetti, and M. Giordano, Journal of Non–Crystalline Solids **303**, 262 (2002).

[72] E. Rössler, Physical Review Letters **65**, 1595 (1990).

[73] S. F. Swallen, P. A., R. J. McMahon, and M. D. Ediger, Physical Review Letters **90**, 015901 (2003).

[74] S.-H. Chen, F. Mallamace, C.-Y. Mou, M. Broccio, C. Corsaro, A. Faraone, and L. Liu, Proceedings of the National Academy of Sciences of the United States of America **103**, 12974 (2006).

[75] B. Chen, E. E. Sigmund, and W. P. Halperin, Physical Review Letters **96**, 145502 (2006).

[76] F. H. Stillinger and J. A.Hodgdon, Physical Review E **50**, 2064 (1994).

[77] J. F. Douglas and D. Leporini, Journal of Non–Crystalline Solids **235-237**, 137 (1998).

[78] K. L. Ngai, Journal of Physical Chemistry B **103**, 10684 (1999).

[79] J. Kim and T. Keyes, Journal of Physical Chemistry B **109**, 21445 (2005).

[80] T. Franosch, M. Fuchs, W. Götze, M. R. Mayr, and A. P. Singh, Physical Review E **56**, 5659 (1997).

[81] G. Tarjus and D. Kivelson, Journal of Chemical Physics **103**, 3071 (1995)).

[82] M. Nicodemi and A. Coniglio, Physical Review E **57**, R39 (1998).

[83] K. S. Schweizer and E. J. Saltzman, Journal of Physical Chemistry B **108**, 19729 (2004).

[84] C. D. Michele and D. Leporini, Physical Review E **63**, 036702 (2001).

[85] P. A. Netz, F. W. Starr, H. E. Stanley, and M. C. Barbosa, Journal of Chemical Physics **115**, 344 (2001).

[86] J. Qian, R. Hentschke, and A. Heuer, Journal of Chemical Physics **110**, 4514 (1999).

[87] S. R. Becker, P. H. Poole, and F. W. Starr, Physical Review Letters **97**, 055901 (2006).

[88] D. C. L. Berthier and J. P. Garrahan, Europhysics Letters **69**, 320 (2005).

[89] S. K. Kumarand, G. Szamel, and J. F. Douglas, Journal of Chemical Physics **124**, 214501 (2006).

[90] M. Dzugutov, S. I. Simdyankin, and F. H. M. Zetterling, Physical Review Letters **89**, 195701 (2002).

[91] P. Bordat, F. Affouard, M. Descamps, and F. Müller-Plathe, Journal of Physics: Condensed Matter **15**, 5397 (2003).

[92] P. Kumar, Proceedings of the National Academy of Sciences of the United States of America **103**, 12955 (2006).

[93] P. Kumar, S. V. Buldyrev, S. R. Becker, F. W. Starr, P. H. Poole, and H. E. Stanley, Proceedings of the National Academy of Sciences of the United States of America **104**, 9575 (2007).

[94] Y.-J. Jung, J. Garrahan, and D. Chandler, Physical Review E **69**, 061205 (2004).

[95] I. Chang and H. Sillescu, Journal of Physical Chemistry B **101**, 8794 (1997).

[96] A. Döß, G. Hinze, B. Schiener, J. Hemberger, and R. Böhmer, Journal of Chemical Physics **107**, 1740 (1997).

[97] W. Steffen, A. Patkowski, G. Meier, and E. Fischer, Journal of Chemical Physics **96**, 4171 (1992).

[98] E. W. Fischer, E. Donth, and W. Steffen, Physical Review Letters **68**, 2344 (1992).

[99] C. A. Angell, Science **319**, 582 (2008).

[100] T. Loerting and N. Giovambattista, Journal of Physics: Condensed Matter **18**, R919 (2006).

[101] P. G. Debenedetti, *Metastable Liquids*, Princeton Univ. Press, Princeton, 1996.

[102] R. Böhmer, R. Chamberlin, G. Diezemann, B. Geil, A. Heuer, G. Hinze, S. Kuebler, R. Richert, B. Schiener, H. Sillescu, H. Spiess, U. Tracht, and M. Wilhelm, Journal of Non–Crystalline Solids **235-237**, 1 (1998).

[103] U. Tracht, M. Wilhelm, A. Heuer, H. Feng, K. Schmidt-Rohr, and H. Spiess, Physical Review Letters **81**, 2727 (1998).

[104] L. A. Deschenes and D. A. V. Bout, Science **292**, 255 (2001).

[105] L. A. Deschenes and D. A. V. Bout, Journal of Physical Chemistry B **106**, 11438 (2002).

[106] A. S. Keys, A. Abate, S. C. Glotzer, and D. J. Durian, Nature Physics **3**, 260 (2007).

[107] R. Richert, Journal of Physics: Condensed Matter **14**, R703 (2002).

[108] S. A. Kivelson, X.-C. Zeng, D. Kivelson, C. M. Knobler, and T. Fischer, Journal of Chemical Physics **101**, 2391 (1994).

[109] K. Y. Tsang and K. K. Ngai, Physical Review E **54**, R3067 (1996).

[110] C. Donati, S. Glotzer, and P. Poole, Physical Review Letters **82**, 5064 (1999).

[111] N. L. cević, F. W. Starr, T. B. S. der, V. N. Novikov, and S. Glotzer, Physical Review E **66**, 030101(R) (2002).

[112] Y. Gebremichael, M. Vogel, M. N. J. Bergroth, F. W. Starr, and S. Glotzer, Journal of Physical Chemistry B **109**, 15068 (2005).

[113] M. Vogel and S. Glotzer, Physical Review Letters **92**, 255901 (2004).

[114] Y. Gebremichael, M. Vogel, and S. Glotzer, Journal of Chemical Physics **120**, 4415 (2004).

[115] D. N. Perera and P. Harrowell, Journal of Chemical Physics **111**, 5441 (1999).

[116] A. Widmer-Cooper, P. Harrowell, and H. Fynewever, Physical Review Letters **93**, 135701 (2004).

[117] A. Pan, J. Garrahan, and D. Chandler, Physical Review E **72**, 041106 (2005).

[118] M. Shell, P. Debenedetti, and F. Stillinger, Journal of Physics: Condensed Matter **17**, S4035 (2005).

[119] G. S. Matharoo, M. S. G. Razul, and P. H. Poole, Physical Review E **74**, 050502(R) (2006).

[120] J. D. Stevenson, J. Schmalian, and P. G. Wolynes, Nature Physics **2**, 268 (2006).

[121] J. Errington, P. Debenedetti, and S. Torquato, Physical Review Letters **89**, 215503 (2002).

[122] A. Geiger and H. Stanley, Physical Review Letters **49**, 1749 (1982).

[123] W. K. S. Kammerer and R. Schilling, Physical Review E **56**, 5450 (1997).

[124] J. Kim, W.-X. Li, and T. Keyes, Physical Review E **67**, 021506 (2003).

[125] M. G. Mazza, N. Giovambattista, F. W. Starr, and H. E. Stanley, Physical Review Letters **96**, 057803 (2006).

[126] O. Steinhauser, Molecular Physics **45**, 335 (1982).

[127] H. J. C. Berendsen, J. P. M. Postma, W. F. van Gunsteren, A. DiNola, and J. R. Haak, Journal of Chemical Physics **81**, 3684 (1984).

[128] E. Lang, D. Girlich, H.-D. Lüdemann, L. Piculell, and D. Müller, Journal of Chemical Physics **93**, 4796 (1990).

[129] S. Glotzer, V. Novikov, and T. S. der, Journal of Chemical Physics **112**, 509 (2000).

[130] G. L. Pollack, Physical Review A **23**, 2660 (1981).

[131] M. Cicerone and M. Ediger, Journal of Chemical Physics **104**, 7210 (1996).

[132] L. Bocquet, J. P. Hensen, and J. Piasecki, Jouranl of Statistical Physics **76**, 527 (1994).

[133] A. Voronel, E. Veliyulin, V. Machavariani, A. Kisliuk, and D. Quitmann, Physical Review Letters **80**, 2630 (1998).

[134] L. Andreozzi, A. D. Schino, M. Giordano, and D. Leporini, epl **38**, 669 (1997).

[135] S. Hensel-Bielowka, T. Psurek, J. Ziolo, and M. Paluch, Physical Review E **63**, 062301 (2001).

[136] L. Berthier, Physical Review E **69**, 020201 (2004).

[137] T. Lombardo, P. Debenedetti, and F. Stillinger, Journal of Chemical Physics **125**, 174507 (2006).

[138] S.-H. Chen, P. Gallo, F. Sciortino, and P. Tartaglia, Physical Review E **56**, 4231 (1997).

[139] D. Ringe and G. A. Petsko, Biophysical Chemistry **105**, 667 (2003).

[140] H. Hartmann, F. Parak, W. Steigemann, G. A. Petsko, D. R. Ponzi, and H. Frauenfelder, Proceedings of the National Academy of Sciences of the United States of America **79**, 4967 (1982).

[141] A. L. Lee and A. J. Wand, Nature **411**, 501 (2001).

[142] B. F. Rasmussen, A. M. Stock, D. Ringe, and G. A. Petsko, Nature **357**, 423 (1992).

[143] W. Doster, S. Cusack, and W. Petry, Nature **337**, 754 (1989).

[144] D. Vitkup, D. Ringe, G. A. Petsko, and M. Karplus, Nature Structural Biology **7**, 34 (2000).

[145] M. Tarek and D. J. Tobias, Physical Review Letters **88**, 138101 (2002).

[146] J. M. Zanotti, M.-C. Bellissent-Funel, and J. Parrello, Biophysics Journal **76**, 2390 (1999).

[147] A. P. Sokolov, H. Grimm, and R. Kahn, Journal of Chemical Physics **110**, 7053 (1999).

[148] J. Norberg and L. Nilsson, Proceedings of the National Academy of Sciences of the United States of America **93**, 10173 (1996).

[149] A. L. Tournier, J. Xu, and J. C. Smith, Biophysics Journal **85**, 1871 (2003).

[150] P. H. Poole, I. Saika-Voivod, and F. Sciortino, Journal of Physics: Condensed Matter **17**, L431 (2005).

[151] M. W. Mahoney and W. L. Jorgensen, Journal of Chemical Physics **112**, 8910 (2000).

[152] M. Yamada, S. Mossa, H. E. Stanley, and F. Sciortino, Physical Review Letters **88**, 195701 (2002).

[153] I. Brovchenko, A. Geiger, and A. Oleinikova, Journal of Chemical Physics **123**, 044515 (2005).

[154] E. Lindahl, B. Hess, and D. van der Spoel, Journal Molecular Modeling **7**, 306 (2001).

[155] P. J. Artymiuk, C. C. F. Blake, D. W. Rice, and K. S. Wilson, Acta Crystallographica B **38**, 778 (1982).

[156] H. R. Drew, R. M. Wing, T. Takano, C. Broka, S. Tanaka, K. Itakura, and R. E. Dickerson, Proceedings of the National Academy of Sciences of the United States of America **78**, 2179 (1981).

[157] J. Wang, P. Cieplak, and P. A. Kollman, Journal of Computational Chemistry **21**, 1049 (2000).

[158] W. Götze, Journal of Physics: Condensed Matter **11**, A1 (1999).

[159] L. Xu, P. Kumar, S. V. Buldyrev, S.-H. Chen, P. H. Poole, F. Sciortino, and H. E. Stanley, Proceedings of the National Academy of Sciences of the United States of America **102**, 16558 (2005).

[160] S.-H. Chen, L. Liu, E. Fratini, P. Baglioni, A. Faraone, and E. Mamontov, Proceedings of the National Academy of Sciences of the United States of America **103**, 9012 (2006).

[161] M. A. Anisimov, J. V. Sengers, and J. M. H. L. Sengers, *Aqueous System at Elevated Temperatures and Pressures: Physical Chemistry in Water, Steam and Hydrothermal Solutions*, pages 29–71, Elsevier, Amsterdam, 2004.

[162] I. Brovchenko, A. Geiger, and A. Oleinikova, Journal of Chemical Physics **118**, 9473 (2003).

[163] K. Morishige and K. Kawano, Journal of Chemical Physics **110**, 4867 (1999).

[164] L. Liu, S.-H. Chen, A. Faraone, C.-W. Yen, and C.-Y. Mou, Physical Review Letters **95**, 117802 (2005).

[165] J. Errington and P. Debenedetti, Nature **409**, 318 (2001).

[166] S.-H. Chen, L. Liu, X. Chu, Y. Zhang, E. Fratini, P. Baglioni, A. Faraone, and E. Mamontov, Journal of Chemical Physics **125**, 171103 (2006).

[167] G. Franzese and M. Rubi, *Aspects of Physical Biology: Biological Water, Protein Solutions, Transport and Replication*, Springer, Berlin, 2008.

[168] P. G. Debenedetti and H. E. Stanley, Physics Today **56**, 40 (2003).

[169] G. Franzese, K. Stokely, X.-Q. Chu, P. .Kumar, M. G. Mazza, S.-H. Chen, and H. E. Stanley, Journal of Physics: Condensed Matter **20**, 494210 (2008).

[170] H. Stanley, P. Kumar, G. Franzese, L. Xu, Z. Yan, M. Mazza, S.-H. Chen, F. Mallamace, and S. V. Buldyrev, Liquid polyamorphism: Some unsolved puzzles of water in bulk, nanoconfined, and biological environments, in *AIP Conference Proceedings*, volume 982, page 251, M. Tokuyama and I. Oppenheim, and H. Nishiyama, eds. AIP Conference Proceedings, 2008.

[171] P. Kumar, G. Franzese, S. V. Buldyrev, and H. E. Stanley, Physical Review E **73**, 041505 (2006).

[172] P. Kumar, G. Franzese, and H. E. Stanley, Physical Review Letters **100**, 105701 (2008).

[173] U. Wolff, Physical Review Letters **62**, 361 (1989).

[174] G. Franzese and H. E. Stanley, Journal of Physics: Condensed Matter **14**, 2201 (2002).

[175] G. Franzese and H. E. Stanley, Physica A **314**, 508 (2002).

[176] K. Stokely, M. G. Mazza, H. E. Stanley, and G. Franzese, arXiv:0805.3468v1 (2008).

[177] G. Franzese and H. E. Stanley, Journal of Physics: Condensed Matter **19**, 205126 (2007).

[178] P. Kumar, G. Franzese, and H. E. Stanley, Journal of Physics: Condensed Matter **20**, 244114 (2008).

[179] G. Franzese, M. I. Marqués, and H. Eugene Stanley, Physical Review E **67**, 011103 (2003).

[180] M. I. Marqués, Physical Review E **76**, 021503 (2007).

[181] M. Ricci, F. Bruni, and A. Giuliani, Faraday Discussion **141**, 347 (2009).

[182] V. Cataudella, G. Franzese, M. Nicodemi, A. Scala, and A. Coniglio, Physical Review E **54**, 175 (1996).

[183] A. Coniglio and F. Peruggi, Journal of Physics A **15**, 1873 (1982).

[184] M. G. Mazza, K. Stokely, H. E. Stanley, and G. Franzese, arXiv:cond-mat/0807.4267 (2008).

[185] M. G. Mazza, N. Giovambattista, H. E. Stanley, and F. W. Starr, Physical Review E **76**, 031203 (2007).

[186] N. Giovambattista, M. G. Mazza, S. V. Buldyrev, F. W. Starr, and H. E. Stanley, The Journal of Physical Chemistry B **108**, 6655 (2004).

[187] A. Oleinikova and I. Brovchenko, Journal of Physics: Condensed Matter **18**, S2247 (2006).

[188] C. A. Angell, *Water: A Comprehensive Treatise*, vol. 7, eds. F. Franks, Plenum, New York, 1982.

[189] P. Ball, Chemical Reviews **108**, 74 (2008).

[190] Y. Levy and J. N. Onuchic, Annual Review of Biophysics and Biomolecular Structure **35**, 389 (2006).

[191] F. Mallamace, C. Corsaro, M. Broccio, C. Branca, N. Gonzlez-Segredo, J. Spooren, S.-H. Chen, and H. E. Stanley, Proceedings of the National Academy of Sciences **105**, 12725 (2008).

[192] D. Liu, Y. Zhang, C.-C. Chen, C.-Y. Mou, P. H. Poole, and S.-H. Chen, Proceedings of the National Academy of Sciences **104**, 9570 (2007).

[193] F. Mallamace, C. Branca, M. Broccio, C. Corsaro, C.-Y. Mou, and S.-H. Chen, Proceedings of the National Academy of Sciences **104**, 18387 (2007).

[194] F. Mallamace, M. Broccio, C. Corsaro, A. Faraone, D. Majolino, V. Venuti, L. Liu, C.-Y. Mou, and S.-H. Chen, Proceedings of the National Academy of Sciences **104**, 424 (2007).

[195] R. J. Speedy, Journal of Physical Chemistry **86**, 3002 (1982).

[196] P. H. Poole, F. Sciortino, T. Grande, H. E. Stanley, and C. A. Angell, Physical Review Letters **73**, 1632 (1994).

[197] H. Tanaka, Nature **380**, 328 (1996).

[198] A. M. Pendás, M. A. Blanco, and E. Francisco, Journal of Chemical Physics **125**, 184112 (2006).

[199] E. D. Isaacs, A. Shukla, P. M. Platzman, D. R. Hamann, B. Barbiellini, and C. A. Tulk, Journal of Physics and Chemistry of Solids **61**, 403 (2000).

[200] B. Guillot, Journal of Molecular Liquids **101**, 219 (2002).

[201] G. Lamoureux, J. Alexander D. MacKerell, and B. Roux, Journal of Chemical Physics **119**, 5185 (2003).

[202] P. K. Mankoo and T. Keyes, Journal of Chemical Physics **129**, 034504 (2008).

[203] J.-P. Piquemal, R. Chelli, P. Procacci, and N. Gresh, Journal of Physical Chemistry A **111**, 8170 (2007).

[204] J. M. Pedulla, F. Vila, and K. D. Jordan, Journal of Chemical Physics **105**, 11091 (1996).

[205] R. Kumar and J. L. Skinner, Journal of Physical Chemistry B **112**, 8311 (2008).

[206] K. Ohno, M. Okimura, N. Akai, and Y. Katsumoto, Physical Chemistry Chemical Physics **7**, 3005 (2005).

[207] J. D. Cruzan, L. B. Braly, K. Liu, M. G. Brown, J. G. Loeser, and R. J. Saykally, Science **271**, 59 (1996).

[208] D. A. Schmidt and K. Miki, The Journal of Physical Chemistry A **111**, 10119 (2007).

[209] M. G. Mazza, K. Stokely, E. G. Strekalova, H. E. Stanley, and G. Franzese, Computer Physics Communications **180**, 497 (2009).

[210] N. Metropolis, A. Rosenbluth, M. Rosenbluth, A. Teller, and E. Teller, Journal of Chemical Physics **21**, 1087 (1953).

[211] B. Guillot, Journal of Molecular Liquids **101**, 219 (2002).

[212] D. P. Landau and K. Binder, *A Guide to Monte Carlo Simulations in Statistical Physics*, Cambridge University Press, 2005.

[213] M. E. J. Newman and G. T. Barkema, *Monte Carlo Methods in Statistical Physics*, Oxford University Press, 1999.

[214] N. Metropolis and S. Ulam, Journal of the American Statistical Association **44**, 335 (1949).

[215] D. Frenkel and B. Smit, *Understanding Molecular Simulations*, Academic Press, 2002.

[216] R. H. Swendsen and J.-S. Wang, Physical Review Letters **58**, 86 (1987).

[217] C. M. Fortuin and P. W. Kasteleyn, Physica **57**, 536 (1972).

[218] A. Coniglio and W. Klein, Journal of Physics A **13**, 2775 (1980).

[219] H. Z. Cummins and R. W. Gammon, Journal of Chemical Physics **44**, 2785 (1966).

[220] R. Zwanzig, *Nonequilibrium Statistical Mechanics*, Oxford University Press, 2001.

CURRICULUM VITAE

Marco G. Mazza

Boston University, Physics Department
Center For Polymer Studies
590 Commonwealth Avenue
Boston, Massachusetts 02215 USA

Telephone: 617-353-3891
Facsimile: 617/353-3783
E-mail: marcokyb@bu.edu

EDUCATION

- 2009, Ph.D. Physics, Boston University, Boston, USA

  Advisor: H. Eugene Stanley

  Thesis: *Thermodynamics and dynamics of supercooled water*
- 2001, M.Sc. Physics, University of Catania, Catania, Italy

  Advisor: Paolo Castorina

  Thesis: *Proper time formulation of Wilson renormalization group*

EMPLOYMENT AND TEACHING EXPERIENCE

- 2008–present, Boston University, experience mentoring one junior graduate student
- 2005–present, Boston University, *Research Assistant*
- 2005, Boston University, *Teaching Assistant*
- 2001, 1-year research grant, University of Catania, Italy

AWARDS

- 2007, National Science Foundation grant to attend STATPHYS-23 in Genoa, Italy
- 2006, Best poster award at Gordon Research Conference on *Water and Aqueous Solutions* at Holderness School in Plymouth, NH, USA
- 2003, Foundation G. Grimaldi and Accademia Gioenia award, Modica, Italy.
- 2002, Bonino-Pulejo Scholarship for the study of the physics of complex systems, Messina, Italy.

COMPUTER SKILLS

- Operating Systems: Windows; Unix/Linux; Experience as chief system administrator of a computer cluster.
- Languages: Fortran, C, shell scripting, Python/VPython, LaTeX.

RESEARCH PAPERS

1. M. Mazza, D. Zappala', "Proper time regulator and Renormalization Group flow", Phys. Rev. D **64**, 105013 (2001).
2. P. Castorina, M. Mazza, D. Zappala', "Renormalization group analysis of the three-dimensional Gross-Neveu model at finite temperature and density", Phys. Lett. B **567**, 31-38 (2003).
3. N. Giovambattista, M. G. Mazza, S. V. Buldyrev, F. W. Starr, and H. E. Stanley, "Dynamic Heterogeneities in Supercooled Water", J. Phys. Chem. B **108**, 6655-6662 (2004).
4. M. G. Mazza, N. Giovambattista, F. W. Starr, and H. E. Stanley, "Relation between Rotational and Translational Dynamic Heterogeneities in Water", Phys. Rev. Lett. **96**, 057803 (2006).
5. P. Kumar, Z. Yan, L. Xu, M. G. Mazza, S. V. Buldyrev, S.-H. Chen. S. Sastry, and H. E. Stanley, "Glass Transition in Biomolecules and the Liquid-Liquid Critical Point of Water", Phys. Rev. Lett. **97**, 177802 (2006).
6. M. G. Mazza, N. Giovambattista, H. E. Stanley, and F. W. Starr, "Connection of translational and rotational dynamical heterogeneities with the breakdown of the Stokes-Einstein and Stokes-Einstein-Debye relations in water", Phys. Rev. E **76**, 031203 (2007) (selected by Virtual Journal of Biological Physics Research **14** (2007)).
7. K. Stokely, M. G. Mazza, H. E. Stanley, G. Franzese, "Effect of hydrogen bond cooperativity on the behavior of water", arXiv:0805.3468 (2008).
8. M. G. Mazza, K. Stokely, H. E. Stanley, G. Franzese, "Anomalous specific heat of supercooled water", arXiv:0807.4267 (2008).

CONFERENCE PROCEEDINGS

1. N. Giovambattista, M. G. Mazza, S. V. Buldyrev, F. W. Starr, and H. E. Stanley, " Heterogeneities in the Dynamics of Supercooled Water," in *Unifying Concepts in Granular Media and Glasses*, edited by A. Coniglio, A. Fierro, H. J. Herrmann, and M. Nicodemi (Elsevier, Amsterdam, 2004).

2. H. E. Stanley, P. Kumar, L. Xu, Z. Yan, M. G. Mazza, S. V. Buldyrev, and S.-H. Chen, "Relation between the Widom Line and the Dynamic Crossover in Bulk Water and in Protein Hydration Water" [Proc International Conf on Quasi-Elastic Neutron Scattering – QENS], MRS Conf Proc (2006).

3. H. E. Stanley, P. Kumar, L. Xu, Z. Yan, M. G. Mazza, S. V. Buldyrev, and S.-H. Chen, "Relation between the Widom Line and the Dynamic Crossover in Bulk Water and in Protein Hydration Water," in Proceedings of the Eighth International Conference on Quasi-Elastic Neutron Scattering, edited by P. E. Sokol, H. Kaiser, D. Baxter, R. Pynn, D. Bossev, and M. Leuschner (Materials Research Society, Warrendale PA, 2007).

4. H. E. Stanley, P. Kumar, L. Xu, Z. Yan, M. G. Mazza, S. V. Buldyrev, S.-H. Chen, and F. Mallamace, The Puzzling Unsolved Mysteries of Liquid Water: Some Recent Progress" [Proc. PASI, Mar del Plata], Physica A **386**, 729-743 (2007).

5. H. E. Stanley, P. Kumar, L. Xu, Z. Yan, M. G. Mazza, S. V. Buldyrev, S.-H. Chen, and F. Mallamace, "New Results on Water in Bulk, Nanoconfined, and Biological Environments," in Proceedings of CTNEXT07, Complexity, Metastability and Nonextensivity, Catania, Italy, 1-5 July 2007, edited by S. Abe, H. J. Herrmann, P. Quarati, A. Rapisarda, and C. Tsallis (American Institute of Physics, 2007).

6. M. G. Mazza, K. Stokely, E. G. Strekalova, H. E. Stanley, G. Franzese, "Cluster Monte Carlo and numerical mean field analysis for the water liquid–liquid phase transition", arXiv:0810.4688 (2008), Computer Physics Communications (in press).

7. H. E. Stanley, P. Kumar, G. Franzese, L. Xu, Z. Yan, M. G. Mazza, S. V. Buldyrev, S.-H. Chen, and F. Mallamace, “Liquid Polyamorphism: Possible Explanation of Water’s Anomalies” [Proc. *International Conf. on Transport, Localization, and Fluctuations in Complex Systems*], European Physical Journal: Special Topics **161**, 1–17 (2008).

8. H. E. Stanley, S. V. Buldyrev, S.-H. Chen, G. Franzese, S. Han, P. Kumar, F. Mallamace, M. G. Mazza, L. Xu, and Z. Yan, “Liquid Polyamorphism and the Anomalous Behavior of Water,” in *Advances in Solid State Physics, Volume 48* [Proc. 2008 Annual Meeting of DFG, Berlin], edited by R. Haug (Springer-Verlag, Berlin/Heidelberg, 2008).

9. G. Franzese, K. Stokely, X. Chu, P. Kumar, M. G Mazza, S.-H. Chen and H. E. Stanley, “Pressure effects in supercooled water: comparison between a 2D model of water and experiments for surface water on a protein”, J. Phys.: Condens. Matter **20**, 494210 (2008).

10. H. E. Stanley, P. Kumar, G. Franzese, L. Xu, Z. Yan, M. G. Mazza, S.-H. Chen, F. Mallamace, and S. V. Buldyrev, “Liquid Polyamorphism: Some Unsolved Puzzles of Water in Bulk, Nanoconfined, and Biological Environments,” in *Fifth International Workshop on Complex Systems, Sendai, Japan*, edited by M. Tokuyama, I. Oppenheim, and H. Nishiyama, AIP Conf. Proc. **982**, 251–271 (2008).